

สมบัติการรับรู้ความเครียดของฟิล์มบางแบเรียมไททาเนตและแบเรียมสตรอนเชียมไททาเนต
เตรียมโดยเทคนิคโซล-เจล

นายปวีศ พรหมเสนา

วิทยานิพนธ์นี้เป็นส่วนหนึ่งของการศึกษาตามหลักสูตรปริญญาวิทยาศาสตรมหาบัณฑิต

สาขาวิชาฟิสิกส์ ภาควิชาฟิสิกส์

คณะวิทยาศาสตร์ จุฬาลงกรณ์มหาวิทยาลัย

ปีการศึกษา 2553

ลิขสิทธิ์ของจุฬาลงกรณ์มหาวิทยาลัย



STRAIN SENSING PROPERTIES OF BARIUM TITANATE AND BARIUM
STRONTIUM TITANATE THIN FILMS PREPARED BY A SOL-GEL
TECHNIQUE

Mr. Pavarit Promsena

A Thesis Submitted in Partial Fulfillment of the Requirements
for the Degree of Master of Science Program in Physics

Department of Physics

Faculty of Science

Chulalongkorn University

Academic Year 2010

Copyright of Chulalongkorn University

Thesis Title STRAIN SENSING PROPERTIES OF BARIUM TITANATE AND BARIUM STRONTIUM TITANATE THIN FILMS PREPARED BY A SOL-GEL TECHNIQUE


By Mr. Pavarit Promsena

Field of Study Physics

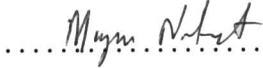
Thesis Advisor Assistant Professor Satreerat Hodak, Ph.D.


Thesis Co-Advisor Assistant Professor Jose Hodak, Ph.D.

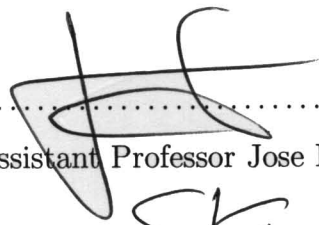
Accepted by the Faculty of Science, Chulalongkorn University in Partial Fulfillment of the Requirements for the Master's Degree



..... Dean of the Faculty of Science
(Professor Supot Hannongbua, Dr.rer.nat.)

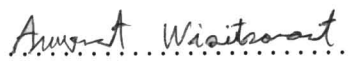
THESIS COMMITTEE


..... Chairman
(Associate Professor Mayuree Natenapit, Ph.D.)


..... Thesis Advisor
(Assistant Professor Satreerat Hodak, Ph.D.)


..... Thesis Co-Advisor
(Assistant Professor Jose Hodak, Ph.D.)



..... Examiner
(Assistant Professor Sakuntam Sanorpim, Ph.D.)


..... External Examiner
(Anurat Wisitsoraat, Ph.D.)

ปวริศ พรหมเสนา : สมบัติการรับรู้ความเครียดของฟิล์มบางแบเรียมและแบเรียมสตรอนเทียมไททานเตเตรียมโดยเทคนิคโซล-เจล. (STRAIN SENSING PROPERTIES OF BARIUM TITANATE AND BARIUM STRONTIUM TITANATE THIN FILMS PREPARED BY A SOL-GEL TECHNIQUE) อ.ที่ปรึกษาวิทยานิพนธ์หลัก : ผศ.ดร. สตรีรัตน์ ไชด์ค, อ.ที่ปรึกษาวิทยานิพนธ์ร่วม : ผศ.ดร. โสเช่ ไชด์ค, 103 หน้า.

เซนเซอร์และทรานสดิวส์เซอร์เป็นอุปกรณ์อิเล็กทรอนิกส์ที่ใช้กันอย่างแพร่หลายในทางอุตสาหกรรมและงานวิจัย ในงานวิจัยนี้ได้ทำการสร้างสเตรนเกจจากวัสดุไดอิเล็กทริกฟิล์มบางแบเรียมไททานเต ($BaTiO_3$) และแบเรียมสตรอนเทียมไททานเต ($BaSrTiO_3$) ที่ปลูกบนแผ่นรองรับที่เป็นแก้วโบโรซิลิเกตบางที่มีความยืดหยุ่นโดยเทคนิคโซล-เจลแบบหมุนและนำฟิล์มบางแบเรียมไททานเตไปสร้างเป็นสเตรนเกจ โดยเทคนิคการสร้างขั้วไฟฟ้าของแบบสปัดเตอร์ริงกระแสนตรง และตัดให้เป็นคานที่มีตัวเก็บประจุเรียงเป็นแถวตรง ซึ่งสเตรนเกจดังกล่าวจะถูกนำไปติดตั้งบนฐานติดตั้งที่มีวัสดุเพียโซอิเล็กทริกเป็นตัวให้แรงกับฟิล์ม เมื่อมีการให้แรงกับสเตรนเกจจะทำให้เกิดการเปลี่ยนแปลงของค่าประจุไฟฟ้า และสามารถตรวจวัดได้โดยวงจรออสซิลเลเตอร์ การโค้งงอของคานสามารถวัดได้โดยสังเกตุจากไมโครมิเตอร์แบบหน้าปัด เมื่อมีการให้แรงเราจะพบว่าฟิล์มมีการเปลี่ยนแปลงความเครียดไปพร้อมกับการเปลี่ยนแปลงของความถี่ของวงจรออสซิลเลเตอร์ นอกจากนี้ฟิล์มบางส่วนยังถูกนำไปสร้างเป็นตัวเก็บประจุเดี่ยวๆที่มีขนาด 3×5 มิลลิเมตร และค่าความจุไฟฟ้าสามารถเปลี่ยนแปลงได้โดยการเปลี่ยนแปลงปริมาณของสตรอนเทียมของ ($Ba_xSr_{1-x}TiO_3$) ค่าคงที่ไดอิเล็กตริกสามารถเปลี่ยนแปลงผกผันกับความถี่ที่เพิ่มขึ้นของสัญญาณไฟฟ้าที่ให้กับตัวเก็บประจุในช่วงความถี่ 100-1100 กิโลเฮิร์ต ค่าคงที่ไดอิเล็กตริกสูงสุดบนฟิล์มบางแบเรียมสตรอนเทียมไททานเต โดยค่าที่แปลงจากค่าความจุไฟฟ้าจะมีค่าสูงสุดเป็น 482 ที่ $x = 0.35$

ภาควิชาฟิสิกส์.....
สาขาวิชาฟิสิกส์.....
ปีการศึกษา2553.....

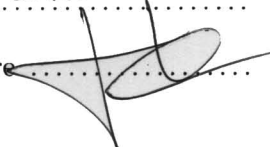
ลายมือชื่อนิติ.....*Pavarit Promsena*.....
ลายมือชื่อ อ.ที่ปรึกษาวิทยานิพนธ์หลัก.....*Satreeat Hoedak*.....
ลายมือชื่อ อ.ที่ปรึกษาวิทยานิพนธ์ร่วม.....

5072350923 : MAJOR PHYSICS

KEYWORDS : BaTiO₃/BaSrTiO₃/THIN FILM/SOL-GEL TECHNIQUE/CAPACITIVE STRAIN GAUAGE

PAVARIT PROMSENA : STRAIN SENSING PROPERTIES OF BARIUM TITANATE AND BARIUM STRONTIUM TITANATE THIN FILMS PREPARED BY A SOL-GEL TECHNIQUE. THESIS ADVISOR : SATREERAT HODAK, PH.D., THESIS CO-ADVISOR : ASST. PROF. JOSE HODAK, PH.D., 103 pp.

We have fabricated strain gauges from dielectric materials, barium titanate (BaTiO₃) and barium strontium titanate (BaSrTiO₃), depositing on flexible borosilicate glasses substrates using a sol-gel method. The coplanar capacitors were patterned on the surface of the films using a DC sputtering technique. The measurement of the strain on a cantilever spring made from capacitor arrays were obtained by monitoring the changing of capacitance of the dielectric films. A parallelogram clamp and a piezoelectric actuator were used for supporting the device under test as well as for the application of strain. The capacitive strain gauge was connected to the oscillator circuit via wire bonding. The changing of capacitance in capacitive strain gauge was done by applying the force with eleven values. The deflection of the beam cantilever was indicated by a dial micrometer. Also, the capacitors were diced individually to 3x5 mm and the capacitance measurements were taken as a function of Sr composition of Ba_xSr_{1-x}TiO₃ and frequency with an LCR meter. The dielectric constant decreased as a function of frequency in the range of 100-1100 kHz and the maximum dielectric constant of Ba_xSr_{1-x}TiO₃ films was found to be 482 at x = 0.35.

Department : Physics Student's Signature .. *Pavarit Promsena* ..
 Field of Study : Physics Advisor's Signature .. *Satreerat Hodak* ..
 Academic Year : 2010 Co-Advisor's Signature ..  ..

Acknowledgements

First of all, I would like to express my appreciation and acknowledgement to my thesis advisor and co-advisor, Assistant Professor Dr. Satreerat Hodak and Assistant Professor Dr. Jose Hodak, respectively for their teaching during the time of my master degree of Chulalongkorn university. I am also grateful to Associate Professor Dr. Mayuree Natenapit, Assistant Professor Dr. Sakuntam Sanorpim and Dr. Anurat Wisitsoraat for attending as a chairman and committee of my dissertation, respectively. All of whom have made useful comments and help in the improvement of this thesis.

I would like to thank Dr. Anurat wisitsoraat and Mr. Disayut Phokharatkul from National electronic and technology computer center(NECTEC) for making electrode patterns on the films. I would like to thank NECTEC to let me use some equipments needed to finish my thesis work. Also, I would like to thank all technicians, Mr. Manop Tirarattanasompat, Mrs. Sopit Poompuang, for the help in the X-ray and WDX experiments, respectively.

My sincere thank to Miss Thidarat Supasai, Miss Yumairoh Kasa, Miss Ornicha Kongwut and all to my friends and colleagues, for their fun helps, suggestion and a good relationship throughout my study.

I would like to thanks to Miss Chonticha Kongsiriwattanakul for her morale and always being near by my side all the time when I feel down.

Finally, a deep affectionate gratitude goes to my father, my mother, and my younger brother for their love, encouragement and supporting throughout my entire study.

Contents

	Page
Abstract (Thai)	iv
Acknowledgements	vi
Contents	vii
List of Tables	x
List of Figures	xi
 Chapter	
I INTRODUCTION	1
1.1 Motivation	1
1.2 Aims of thesis	3
1.3 Overview of thesis	3
II THEORETICAL BACKGROUND	5
2.1 Barium titanate (BaTiO_3) and Barium strontium titanate (BaSrTiO_3) properties	5
2.2 Sol gel method	7
2.3 Beam deflection theory	9
2.3.1 Definition of the simple stress and the simple strain	10
2.3.2 Hooke's law	14

Chapter	Page
2.3.3 The bending moment	15
2.3.4 The deflection of the cantilever	18
2.3.5 The stress of the cantilever	21
2.3.6 The strain of the cantilever	21
2.3.7 The simulation of beam deflection	22
2.4 Dielectric properties	27
2.4.1 Dielectric constant	27
2.4.2 Dielectric loss	28
2.4.3 Conversion from capacitance to dielectric constant	28
III CHARACTERIZATION TECHNIQUES	32
3.1 X-ray diffractometry	32
3.1.1 The X-ray source	32
3.1.2 Bragg's law	36
3.1.3 The X-ray diffractometer	38
3.2 Wavelength dispersive X-ray spectroscopy	39
IV EXPERIMENTAL METHODS	42
4.1 Film preparation on cleaned substrates	42
4.1.1 Preparation of barium titanate (BTO) precursor	42
4.1.2 Preparation of barium strontium titanate (BSTO) precursor	43
4.1.3 Film deposition	45
4.2 Device fabrication	48
4.3 Capacitance measurement	51

Chapter	Page
4.4 Resonant frequency of an oscillator circuit as a function of stress and strain	54
V RESULTS AND DISCUSSION	58
5.1 The effect of annealing temperature and annealing time on the crystal structure and the deformation of the borosilicate substrate . . .	58
5.2 The WDS result of barium strontium titanate	63
5.3 X-ray diffraction pattern	65
5.3.1 X-ray diffraction pattern of BaTiO ₃ , Ba _{0.35} Sr _{0.65} TiO ₃ and Ba _{0.8} Sr _{0.2} TiO ₃ thin films	65
5.4 Dielectric response of the film	67
5.4.1 Dielectric constant and dielectric loss versus frequency of BaTiO ₃ thin film	67
5.4.2 Dielectric constant and dielectric loss versus frequency of Ba _{0.8} Sr _{0.2} TiO ₃ thin film	67
5.4.3 Dielectric constant and dielectric loss versus frequency of Ba _{0.65} Sr _{0.35} TiO ₃ thin film	69
5.5 Stress and strain sensing of barium titanate thin film	72
5.5.1 Stress and strain sensing of the cantilever made of barium titanate thin film at x = 0.7 cm.	72
5.5.2 Stress and strain sensing sensing of the cantilever made of barium titanate thin film at x = 0.5 cm.	76
VI CONCLUSIONS	79
References	81

Chapter	Page
Appendices.....	85
Appendix A: Oscillator circuit theory.....	86
Appendix B: Simulation program.....	88
Appendix C: XRD database.....	90
Appendix D: Conference presentation.....	95
Appendix E: Publication.....	97
Appendix F: Research award.....	103
Vitae.....	104

List of Tables

Table	Page
2.1 The parameters for simulation program for the interdigitated capacitor at $x = 0.7$ cm	23
3.1 The characteristic wavelength generated by Mo [11]	36
3.2 The characteristic wavelength generated by Cu [11]	36
4.1 Type of BTO and BSTO thin films with different growth conditions	44
4.2 Type of BTO and BSTO thin films with different stoichiometry . .	44
5.1 WDX result of $\text{Ba}_{0.69}\text{Sr}_{0.31}\text{TiO}_3$ thin film	64
5.2 WDX result of $\text{Ba}_{0.8}\text{Sr}_{0.2}\text{TiO}_3$ thin film	64
5.3 WDX result of $\text{Ba}_{0.35}\text{Sr}_{0.65}\text{TiO}_3$ thin film	64

List of Figures

Figure	Page
2.1 Perovskite cubic structure of BTO or BSTO	6
2.2 Sol-gel process and the final morphology of product	8
2.3 (a) The relation between film thickness and spinning speed (b) The relation between film thickness and spinning time	9
2.4 Perpendicular force with cross section area	10
2.5 The changing length of the material	10
2.6 The stress and strain diagram of elastic material	11
2.7 The stress and strain diagram of fragile material	13
2.8 The bending cantilever	13
2.9 The small section of the cantilever	14
2.10 The force on the smallest cross sectional area of the cantilever . . .	17
2.11 The sketch of the cantilever from the experiment	18
2.12 The elastic curve	19
2.13 Cross section of the cantilever	19
2.14 The diagram of the cantilever consisting of an interdigitated capacitor	23
2.15 The simulation of beam deflection of the borosilicate cantilever . . .	25
2.16 The stress of the borosilicated cantilever from simulation	26
2.17 The strain of the borosilicated cantilever from simulation	26
2.18 Electric dipoles in electric field	27

Figure	Page
2.19 Interdigitated pattern for dielectric constant conversion	29
2.20 The image of a cross section of BaTiO ₃ thin film taken from FSEM	31
2.21 The image of a cross section of Ba _{0.35} Sr _{0.65} TiO ₃ thin film taken from FSEM	31
3.1 X-ray spectrum of molybdenum as a function of applied voltage . .	33
3.2 (a) The schematic of electronic transitions in an atom (b) Excitation and emission process indicated by arrows	35
3.3 Diffraction of X-ray by a crystal	37
3.4 The X-ray diffractometer	38
3.5 Schematic representation of a wavelength dispersive spectrometer and associated electronics	39
3.6 (a) Fully focusing wavelength-dispersive spectrometer (b) Move- ment of the focusing circle to change the diffraction angle of WDS .	41
4.1 The speed diagram of spin coating process	45
4.2 The temperature diagram of annealing process	46
4.3 The process of BTO and BSTO film preparation	47
4.4 (a) The home made DC sputtering machine	49
4.5 (a) Placing BTO or BSTO thin films on array of magnets (b) At- taching the interdigitated chrome mask with the magnet	49
4.6 (a) The dicing saw machine (b) Inside the dicing saw machine (c) The diamond saw	50
4.7 The wire bonding machine (Model 4522)	51

Figure	Page
4.8 (a) The pattern of interdigitated mask (b) Coplanar capacitor (c) Interdigitated mask (d) An array of interdigitated capacitor in cantilever form	52
4.9 The strain gauge	52
4.10 The LCR meter	53
4.11 The ring resonator box	53
4.12 Labview program Version 8.5	54
4.13 The strain gauge fixture	55
4.14 (a) The overall experimental setup (b) The fixture with piezo actuator and dial micrometer	57
5.1 The deformed borosilicate glass substrate with gold electrode patterned on the BSTO film (BSTO#5) with 7 layers annealed at at $650^{\circ}C$ of 1.5 hr for each layer	60
5.2 XRD patterns of BSTO#3 and BSTO#5 ($Ba_{0.35}Sr_{0.65}TiO_3$)	60
5.3 XRD pattern of BTO#1 (6 layers) thin film annealed for 1 hr for each layer	62
5.4 XRD pattern of BTO#1 (6 layers) thin film after increasing annealing time for 2 hr	62
5.5 XRD pattern of $BaTiO_3$, $Ba_{0.8}Sr_{0.2}TiO_3$ and $Ba_{0.35}Sr_{0.65}TiO_3$	66
5.6 (a) Capacitance of $BaTiO_3$ thin film (b) Dielectric constant of $BaTiO_3$ thin film (c) Dielectric loss of $BaTiO_3$ thin film	68

Figure	Page
5.7 (a) Capacitance of $\text{Ba}_{0.8}\text{Sr}_{0.2}\text{TiO}_3$ thin film (b) Dielectric constant of $\text{Ba}_{0.8}\text{Sr}_{0.2}\text{TiO}_3$ thin film (c) Dielectric loss of $\text{Ba}_{0.8}\text{Sr}_{0.2}\text{TiO}_3$ thin film	70
5.8 (a) Capacitance of $\text{Ba}_{0.35}\text{Sr}_{0.65}\text{TiO}_3$ thin film (b) Dielectric constant of $\text{Ba}_{0.35}\text{Sr}_{0.65}\text{TiO}_3$ thin film (c) Dielectric loss of $\text{Ba}_{0.35}\text{Sr}_{0.65}\text{TiO}_3$ thin film	71
5.9 Variation of the resonant frequency and the change in resonant frequency of the oscillator with applied deflection at the free end whereas the bottom axis shows the corresponding stress at the location of the capacitor (at $x = 0.7$ cm) and the top axis show the deflection at $x = 0.7$ cm	74
5.10 Variation of the resonant frequency and the change in resonant frequency of the oscillator with applied deflection at the free end whereas the bottom axis shows the corresponding stress at the location of the capacitor (at $x = 0.7$ cm) and the top axis show the deflection at the end point	74
5.11 Variation of the resonant frequency and the change in resonant frequency of the oscillator with applied deflection at the free end whereas the bottom axis shows the corresponding strain at the location of the capacitor (at $x = 0.7$ cm) and the top axis show the deflection at 0.7 cm	75

Figure	Page
5.12 Variation of the resonant frequency and the change in resonant frequency of the oscillator with applied deflection at the free end whereas the bottom axis shows the corresponding strain at the location of the capacitor (at $x = 0.7$ cm) and the top axis show the deflection at the end point	75
5.13 Variation of the resonant frequency and the change in resonant frequency of the oscillator with applied deflection at the free end whereas the bottom axis shows the corresponding stress at the location of the capacitor (at $x = 0.5$ cm) and the top axis show the deflection at $x = 0.5$ cm	77
5.14 Variation of the resonant frequency and the change in resonant frequency of the oscillator with applied deflection at the free end whereas the bottom axis shows the corresponding stress at the location of the capacitor (at $x = 0.5$ cm) and the top axis show the deflection at the end point	77
5.15 Variation of the resonant frequency and the change in resonant frequency of the oscillator with applied deflection at the free end whereas the bottom axis shows the corresponding strain at the location of the capacitor (at $x = 0.5$ cm) and the top axis show the deflection at 0.5 cm	78
5.16 Variation of the resonant frequency and the change in resonant frequency of the oscillator with applied deflection at the free end whereas the bottom axis shows the corresponding strain at the location of the capacitor (at $x = 0.5$ cm) and the top axis show the deflection at the end point	78
A.1 The schematic of oscillator circuit	87
A.2 Output signal from oscillator circuit	87

Figure	Page
B.1 Front panel of the simulation program by Mr. Pakorn Yimpa	89
F.1 Best poster presenter award from 6 th Mathematics and Physical Science Congress 2010 at University of Malaya Kualalumpur Malaysia	103

CHAPTER I

INTRODUCTION

1.1 Motivation

Sensors and transducers are popular electronic devices used in many industrial and research. It can convert between mechanical force and electrical signal. There are many types of these devices such as piezoresistivity, piezoelectricity, variable capacitance, optical and resonant techniques. Strain gauge is a mechanical sensor which consists of thin film and with metal electrodes for measuring a change in its electrical properties while applying the force. It is used to convert between applied strain and electrical signal. Piezoelectric materials can convert a voltage to a force because of non centro-symmetric property of these materials [11]. Piezoelectric sensor and actuator can produce an electric charge when subjected to an applied strain and deformed by applying an electric field [2]. Ferroelectric materials can perform piezoelectricity when the temperature is below Curie point depending on the type of material [3].

In the past, lead zirconate titanate ($\text{Pb}_x\text{Zr}_{1-x}\text{TiO}_3$: PZT) which is one type of piezoelectric material became popular for fabrication of sensors and actuators because of its high piezoelectric constant which is enabled to create a large charge while applying force on the material. It is used to fabricate device such as microcantilever which is used to measure force between atom due to high value of charge coefficient [4]. The charge coefficient is the ratio between applying force and generated charge from PZT device. PZT is d_{33} material due to the same direction of applying force and polarization in material. For ceramic form of PZT, d_{33}

is about 300-600 pC/N range [5]. However, PZT contains lead which is environmentally unfriendly. Recently, some researchers developed various types of strain gauge from different types of material such as indium sesquitelluride (In_2Te_3) [6], tantalum nitride (TaN) [7], titanium dioxide (TiO_2) [8] and amorphous carbon ($a-C$) [9]. Therefore, in this thesis I chose to synthesize non-lead based piezoelectric materials for the fabrication of a strain gauge. In this research, barium titanate (BaTiO_3 : BTO) and barium strontium titanate ($\text{Ba}_x\text{Sr}_{1-x}\text{TiO}_3$: BSTO) films which were non-lead materials are deposited on thin flexible transparent substrates such as borosilicate glass with about 0.16 millimeter thickness using a sol-gel spinning method. After that, our thin-films were characterized some properties such as crystal structure and stoichiometry using X-ray diffraction and wavelength dispersive X-ray spectrometer, respectively. There are many methods in fabrication of strain gauge such as sputtering technique, and thermal spray [10]. In our case, Au/Cr sputtering technique is used to fabricate the strain gauge. Because of our strain gauge is developed for measuring of micro level force, the beam deflection theory is used to study the stress and the strain at different locations on the cantilever at which the film is on the top of borosilicate glass substrate [12]. Normally, strain is sensed by resistive strain gauge receiving analog signal in this thesis, the fabricated strain gauge will act as capacitive sensor due to the benefit of high dielectric constant of BTO and BSTO. Capacitive measurements are based on frequency measurements which give less noise and extremely accurate. In applications of sensor and transducer, several properties of ferroelectric materials such as the dielectric constant, the piezoelectric constant, and the charge coefficient must be considered. Capacitive sensor is quite expensive so this thesis aims to combine the easy fabrication and the low cost in the construction of strain gauges. We desire to fabricate a strain sensor consisting of BTO or BSTO films at which the strain is sensed by measuring the variations in the film capacitance resonant using a capacitance-dependent oscillator and measuring the resonant frequency as the observable. The working principle is that the strain induced will vary the dielectric properties of the film and thus, change the capacitance. The strain gauge

could then be used to determine the resonant frequency of the oscillator and then use it as strain to frequency converter.

In the past, many researchers have studied mostly electrical properties of BTO and BSTO films in both individual coplanar capacitor form and parallel capacitor form [14, 19]. According to the literature review, the stress and strain sensing of the coplanar capacitor arranged in an array form on borosilicate glass was diced to a rectangular shape was never studied before.

1.2 Aims of thesis

1) To reproducibly prepare and characterize barium titanate and barium strontium titanate thin films.

2) To fabricate a strain gauge and measure the strain sensing of the prepared film.

1.3 Overview of thesis

This thesis organized as follows:

Chapter II: This chapter introduces the detail about sol gel method, beam deflection theory and dielectric properties of BTO and BSTO films.

Chapter III: This chapter describes the detail about the characterization techniques used in this thesis such as X-ray diffractometry and wavelength dispersive X-ray Spectroscopy (WDX).

Chapter IV: Describes about experiments carried out this thesis namely film preparation, strain gauge fabrication, measuring of capacitance of coplanar capacitors and measuring of strain sensing.

Chapter V: Contains the results and discussion Storing with X-Ray diffraction patterns, capacitance measurements BaTiO_3 and BaSrTiO_3 thin films, curves of stress versus frequency and strain versus frequency.

Chapter VI: This chapter contains the conclusions of this thesis concerning the synthesis of BaTiO_3 and BaSrTiO_3 thin film and the stress+strain applications.

CHAPTER II

THEORETICAL BACKGROUND

This chapter introduces the barium titanate and barium strontium titanate materials, and their dielectric properties, the sol-gel technique, beam deflection theory . We derive some equations in beam deflection theory such as the the deflection equation of beam cantilever, the equation of stress of beam cantilever and the equation of strain for the beam cantilever. We then apply the simulation of bending beam with the real experiments as presented in section 2.3.7. The dielectric constant, the dielectric loss and the conversion of capacitance to dielectric constant will be described in detail in section 2.4

2.1 Barium titanate (BaTiO_3) and Barium strontium titanate (BaSrTiO_3) properties

Barium titanate (BTO) and barium strontium titanate (BSTO) are high dielectric constant materials with perovskite structures as shown in Fig. 2.1. Both types of materials have valuable properties such as piezoelectricity, ferroelectricity, and high tunable dielectric properties. Piezoelectricity is the ability of some materials to generate an electric potential in response to an applied mechanical stress and it was discovered by Curie in 1880. BTO and BSTO are in the 21th type of crystal among the 32 types found in nature which have piezoelectricity [13]. This phenomena arises from the d_{33} non-centro symmetry of their structure, causing the polarization to occur in the same direction as the applied force [13]. Satreerat Hodak and Charles T.Rogers have found that STO thin films prepared

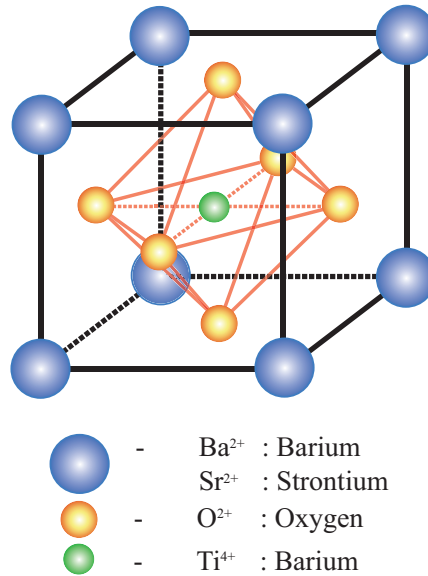


Figure 2.1: Perovskite cubic structure of BTO or BSTO

by pulse laser deposition showed a dielectric constant close to 300 at room temperature, which typically reaches a maximum between 1000 and 10,000 depending on the growth rate in the 30-100 K range and then decreases steadily [14]. These STO thin films showed a dielectric loss in the range of 10^{-2} - 10^{-3} [14]. At room temperature, STO thin films are paraelectric and do not show a phase transition to ferroelectric down to 4 K. Note that the transition temperature or Curie point is the temperature at which ferroelectric state changes to paraelectric state. On the other hand, the ferroelectricity occurs when the temperature is below Curie point. Run Xu et al. have found that the dielectric constant at room temperature of BTO thin films prepared by a sol-gel method reached 360-330 in the 0.1-1000 kHz frequency range. Experiments showed that an increase of the dielectric constant and its tunability at room temperature can be achieved through film growth of $\text{Ba}_x\text{Sr}_{1-x}\text{TiO}_3$ compound [15, 16] and [17] and by the use of $\text{SrTiO}_3/\text{BaTiO}_3$ multilayered thin films [18]. The optimum dielectric tunability occurs at a different temperature range (4-100 K for SrTiO_3 [19, 20] and 250-400 K for BaTiO_3 [21, 22]). BTO shows ferroelectricity at room temperature and paraelectricity at temperatures higher than 120°C [23]. By comparison, the Curie temperature of BTO and STO are 393 K [24] and 105 K [24], respectively which are considered

to be high and low transition temperatures respectively. BTO and STO is a forms solid solutions of Barium strontium titanate, Lahiry found that the Curie temperature of $\text{Ba}_x\text{Sr}_{1-x}\text{TiO}_3$ is between -180°C – -125°C whereas x is varied from 0.1-1.0 [23].

Ferroelectricity and paraelectricity in BSTO depend on the transition temperature which can be lowered by changing Ba/Sr content. The transition temperature of BSTO can be decreased by increasing amount of strontium [23, 25]. Mostly the transition temperature decreases nearly linearly with the Sr content. However, for the films the rate of variations of the transition temperature could slightly vary depending on the growth technique. For example, used rate of transition temperature change for BSTO thin films prepared by pulsed laser deposition was found to be $-4.59^\circ\text{C}/\text{mol}\%$ of Sr, while a sol-gel method yield a rate of $xx^\circ\text{C}/\text{mol}\%$ of Sr [25]. In section 5.4, I will show the results of dielectric constant of BTO, and $\text{Ba}_x\text{Sr}_{1-x}\text{TiO}_3$ thin films prepared by a sol-gel spin coating technique for value of $x = 0.35, 0.8, \text{ and } 0.69$.

2.2 Sol gel method

Sol-gel, is a well known wet chemical deposition method. It is one of the simplest techniques in preparation of thin films. A sol is a stable suspension of colloidal particles within a liquid. A gel is a porous 3-dimensionally interconnected solid network that expands throughout a liquid medium. If most of the liquid is removed, then brittle solid obtained is called a xerogel or an aerogel, depending on the drying method.

The preparation of homogeneous solution or precursor can be done in room temperature but every step should be done in a clean room to avoid any contaminations. From Fig. 2.2, the first step in sol-gel reaction is the formation of an inorganic polymer by hydrolysis and condensation reactions. The solution of precursor is hydrolyzed to a sol, a dispersion of colloidal particles in liquid. A gel

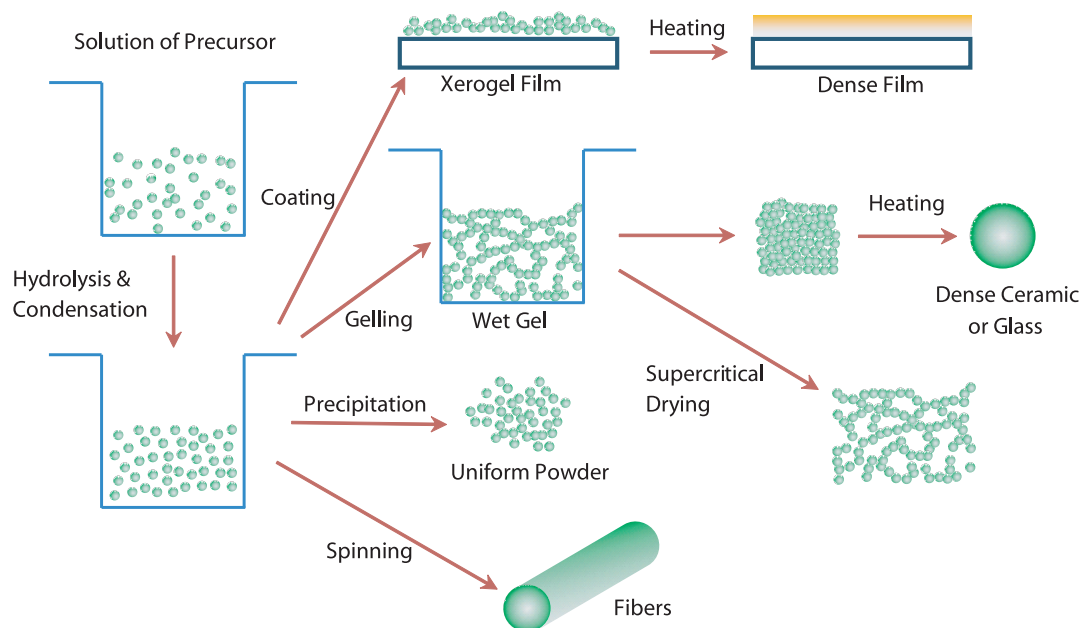


Figure 2.2: Sol-gel process and the final morphology of product

is an inorganic network enclosing a continuous liquid phase. These processes are called sol-gel transition. Aerogels are produced from upon removal of the liquid resulting in the pores of the solid. A xerogel occurs when the gel is dried under ambient conditions. Heat treatment is used to shape the material into any desired such as films, fiber, and monosized powders and subsequently to convert it into a ceramic material. The sol-gel method can be combined with dip coating, pyrolysis, spin coating, vacuum techniques etc. The spinning process is used here described by a speed diagram in Chapter 4. The spin coating machine can be used as a programmable device via LCD panel controller. The diagram of spinning program we used for the spin coating machine is shown in experimental detail part (See in Chapter 4). Spin coating technique uses the centrifuged force for spreading of the precursor cover the substrate. The thickness of the film depends on the speed and time for spinning. There are two ways of dropping precursor. The first way is to drop precursor while the substrate on the holder is spinning. This is used for high viscosity precursor solutions. The second way is to drop precursor on the substrate before it spins. This is used for low viscosity sols. Higher spinning speeds and low solution viscosity will result in thinner films especially when using

long time to spin. The comparison between two variables, spinning speed and spinning time, and film thickness is shown in Fig. 2.3

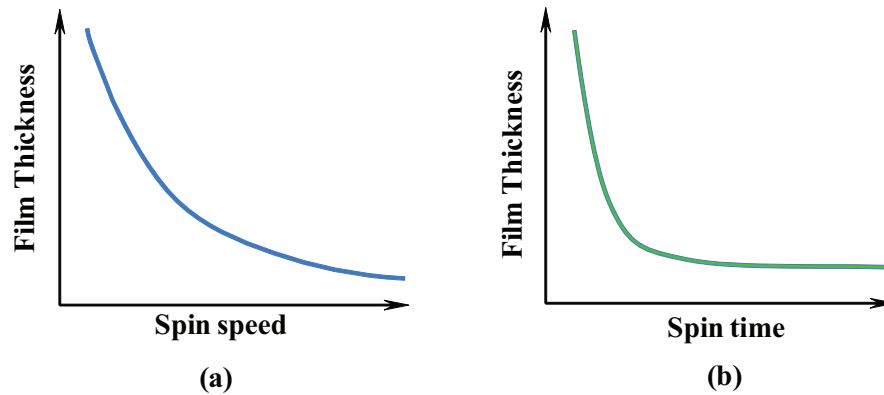


Figure 2.3: (a) The relation between film thickness and spinning speed (b) The relation between film thickness and spinning time

2.3 Beam deflection theory

Studying strain sensing property of thin film is done by determination of stress and strain in thin film at any position on the cantilever by observation of capacitance changes on thin film. In this thesis, we deposited barium titanate (BTO) and barium strontium titanate (BSTO) thin film on flexible borosilicate glass substrate to construct strain gauge. The strain gauges are fixed at one end on a fixture. A force is applied to the strain gauge by a piezoelectric actuator. The detail of strain sensing experiment will be explained in experimental section. Stress and strain at any position on the cantilever can be evaluated using beam deflection theory by knowing the value of the applied force at the free end of the cantilever. The applied force can not be measured directly but we can measure the bending range or deflection distance of the strain gauge instead. This section describes the basic mechanical properties of the material and some useful equations for this strain sensing experiment.

2.3.1 Definition of the simple stress and the simple strain

The stress (σ) of the material is defined as

$$\sigma = \frac{F}{A} \quad (2.1)$$

where F is the perpendicular force on cross sectional area (N), A is Cross section area (m^2)

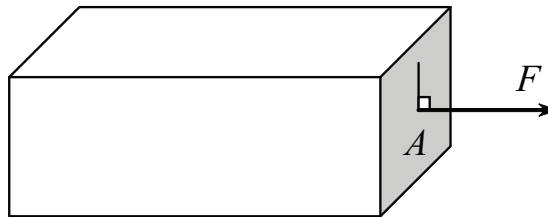


Figure 2.4: Perpendicular force with cross section area

The strain (ε) of the material is

$$\varepsilon = \frac{\Delta l}{l} \quad (2.2)$$

where Δl is the length by which the material has been extended, l the original length of the material before extending (m)

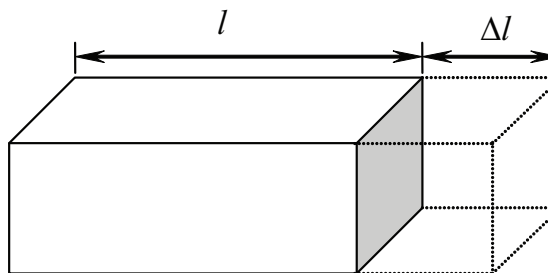


Figure 2.5: The changing length of the material

The Young's modulus (E) of the material is

$$E = \frac{\sigma}{\varepsilon} = \frac{\frac{F}{A}}{\frac{\Delta L}{L}} = \frac{F}{A} \cdot \frac{L}{\Delta L} \quad (2.3)$$

In order to find a relation between stress and strain of the cantilever we make the following assumptions;

1.The section of the cantilever under consideration is always a plane although the cantilever is bended.

2.The cantilever is made of a homogeneous material which follows Hooke's law. The extension (Δl) of the material is proportional to the applied force.

3.The modulus of elastic compression is equal to modulus of elastic for tension.

4.The cantilever must have smooth cross section area.

5.The plane of the force must consist of principal axis of cross section area of cantilever and perpendicular with longitudinal axis of cantilever.

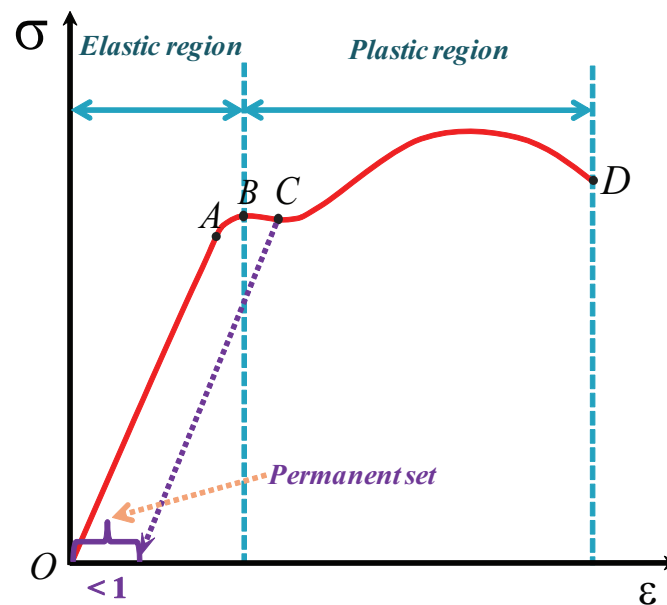


Figure 2.6: The stress and strain diagram of elastic material

We can determine the elastic properties of any material from stress strain diagram. Figure 2.6 shows a typical stress and strain diagram for an elastic material. Any point in the graph shows the state of the material at a certain force.

From O to A , the stress and strain are proportional, in this region it obeys Hooke's law. Point A is the proportional limit.

From A to B, the stress and strain are not proportional to each other. If stress is removed, the material still returns in to its original shape and length. Point B is the elastic limit or yield point.

From O to B, the material is classified as inelastic.

From B to C, if the material is stressed further, the strain increases rapidly, but when the stress is removed at some point beyond B (not over C) the material does not come back to its original shape of length then the material is said to have a permanent offset.

From B to D, the material is said to undergo plastic deformation "plastic region" If the stress is beyond point D, fracture takes place, at point D is called the fracture point.

The cantilever or beam in our experiment is made of BTO or BSTO films grown on borosilicate glass which is considered to be fragile material. Our experiment will take place in proportional region (force smaller than that for point A) on stress strain diagram in Fig. 2.6. The Young's modulus of borosilicate glass is 6.3×10^{10} Pascal, which mean it is a fragile material. The stress strain diagram for fragile material is shown in Fig. 2.7. The linear region of stress-strain graph is very short, and this material can be extended only 0.2 percent of its original length.

The shape of the bending deformation cantilever is shown in Fig. 2.8. For small bending of the cantilever, the neutral surface for neutral line goes through the center of gravity of the cross section. This is true for pure bending without stretching or compressing at the same time.

From Fig. 2.8, after the cantilever is bent, a small section of the cantilever with original length l extending to each side $\frac{\Delta l}{2}$ so the total changing is Δl . The radius of bending cantilever is ρ and the range from neutral axis to the upper edge of the cantilever is r . The small angle of bending section of cantilever is $d\theta$. The strain of the cantilever can be written as;

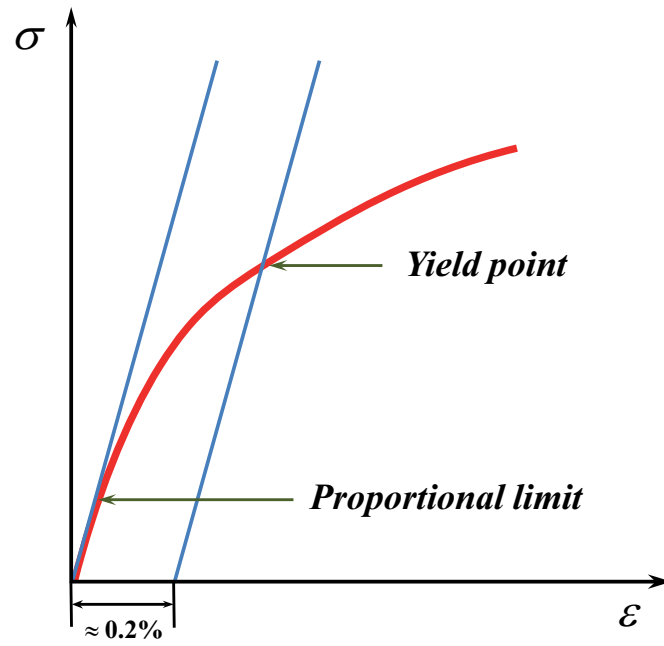


Figure 2.7: The stress and strain diagram of fragile material

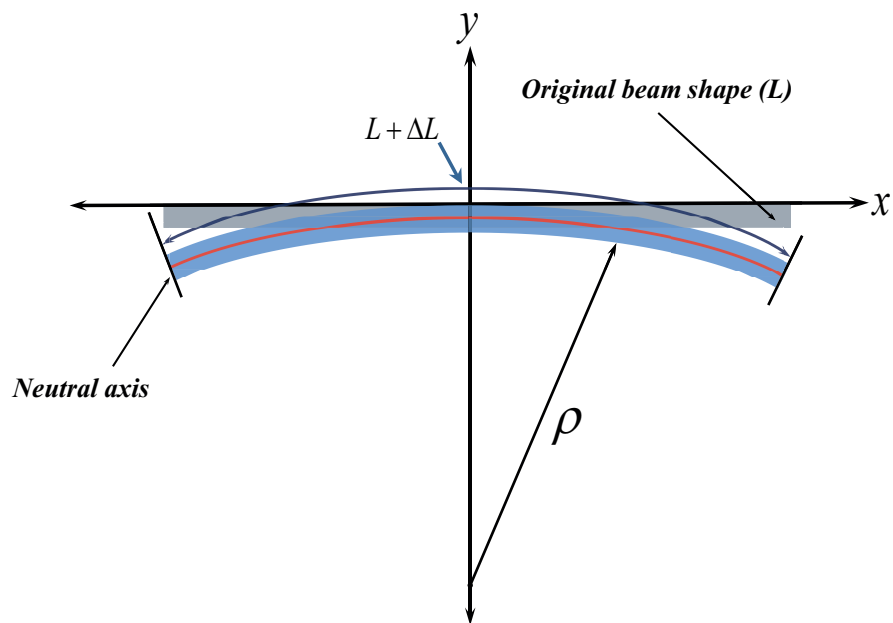


Figure 2.8: The bending cantilever

$$\varepsilon = \frac{\Delta l}{l} = \frac{2rd\theta}{2\rho d\theta} = \frac{r}{\rho} \quad (2.4)$$

where r is the length from neutral axis at the point of interest, and ρ is the radius

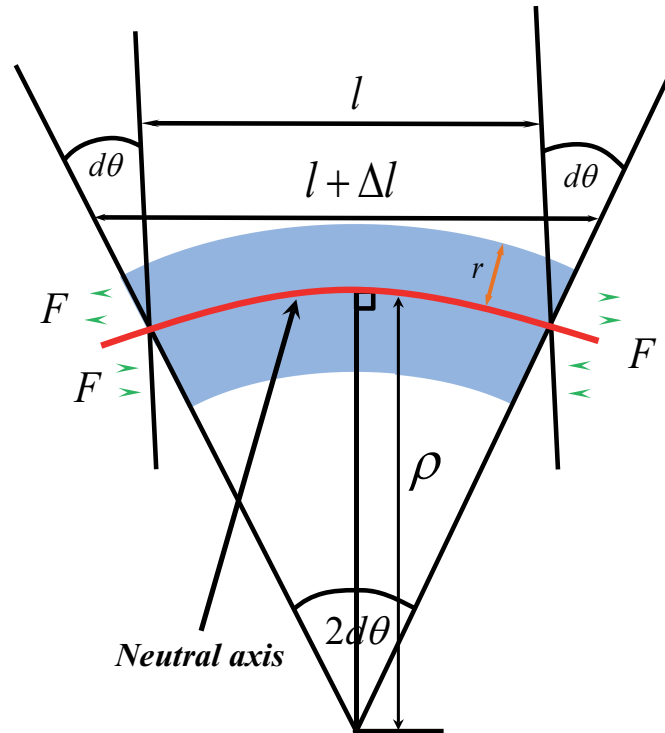


Figure 2.9: The small section of the cantilever

of bending part of the cantilever measured from the center point of circle to the neutral axis.

2.3.2 Hooke's law

Hooke's law is a linear relationship between the extension of material due to a force applied along its axis proportional to the stretching length which is given by

$$F \propto \Delta l \quad (2.5)$$

From Figure 2.9, the extensional part of the box depends on the perpendicular for but independent with the original length. This ratio can be define as

$$F \propto \frac{\Delta l}{l} \quad (2.6)$$

The perpendicular force must be proportional to the cross-sectional area A of the block in Fig. 2.4. We will write Hooke's law for rectangular block in the form (from equation 2.3).

$$F = EA \left(\frac{\Delta l}{l} \right) \quad (2.7)$$

From equation (2.1) and (2.2) and Hooke's law for a rectangular block (equation 2.7), the Hooke's law equation for the small section of the cantilever, we can calculate the relation between the radius bending of the cantilever (ρ) and the range from neutral axis to the point of interest (r);

$$\frac{1}{\rho} = \frac{\sigma}{Er} \quad (2.8)$$

2.3.3 The bending moment

In order to find the stress and strain of the cantilever, we have to know the bending moment of the cantilever by observing the pure bending of the material applied with our cantilever. From our work, we have a simple bending beam cantilever in Fig. 2.8. If we consider the small section of bent cantilever (Fig. 2.9) and the cross-section in Fig. 2.10, we can see that the material below the neutral axis or neutral surface has a compressional strain which is proportional to its distance from the neutral surface as shown below.

$$\frac{\Delta l}{l} = \frac{y}{\rho} \quad (2.9)$$

From the simple stress (equation (2.1)), the simple strain (equation (2.2)), the Young's modulus of the material (equation (2.3)) and equation (2.9), we find that y is proportional to the distance from the neutral surface (r)

$$\frac{\Delta F}{\Delta A} = E \frac{y}{\rho} \quad (2.10)$$

The small section of cantilever (Fig. 2.9) shows the forces acting in the material of the cantilever. The forces acting across cross section above and below neutral surface are in the opposite direction on x axis. These forces are cause the torque about the neutral line and we can calculate the bending moment from these. From Fig. 2.9, forces in x axis direction make the total bending moment around x axis and y axis disappear ($\sum M_x = 0, \sum M_y = 0$) because of bending of the cantilever in the z axis. The total bending moment of cantilever can be calculated by integrating the force ($dF_x = \sigma_x dA$).

$$M_z = \int_{\text{cross section}} y dF_x = \int_{\text{cross section}} y \sigma_x dA \quad (2.11)$$

where M_z is the bending moment around the z axis in x axis direction arising from the force F, σ_x is the stress in x axis direction, dA is the element of cross sectional area of cantilever.

From the third term of equation (2.11) and (2.8), replacing r with y , the blending moment is changed to

$$M_z = \frac{E}{\rho} \int y^2 dA \quad (2.12)$$

From equation (2.12) and Fig. 2.10, we can see that the integral $y^2 dA$ is the moment of inertia about x axis thorough the center of mass of the cantilever. This integral are changed in to I as shown below

$$I = \int_{\text{cross section}} y^2 dA \quad (2.13)$$

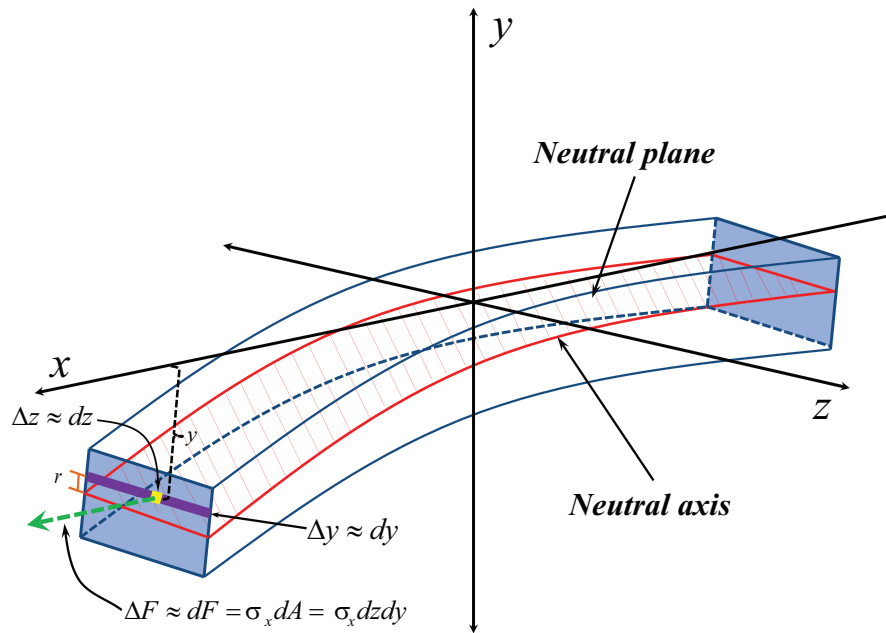


Figure 2.10: The force on the smallest cross sectional area of the cantilever

where I is the moment of inertia of the cross sectional area around the neutral axis or x axis, y = the range from horizontal (x axis).

From the diagram of borosilicate cantilever (Fig. 2.11), we will put the limit of integration in y axis and z axis so the moment of inertia of cross section is changed in to

$$I = \int_{-h}^0 \int_0^w h^2 dz dy = \frac{h^2 w}{12} \quad (2.14)$$

From equation(2.8) and (2.7) the relation between the curve of the cantilever and bending moment is changed to

$$\frac{1}{\rho} = \frac{M}{EI} \quad (2.15)$$

Equation (2.5),(2.10) and (2.11) are used to calculate the stress in the form moment of inertia, bending moment and the range from neutral axis.

$$\sigma = \frac{Mr}{I} \quad (2.16)$$

In my thesis, we will study the bent cantilever with a concentrate force P acting at position a from the clamping point, as sketched in Fig. 2.11.

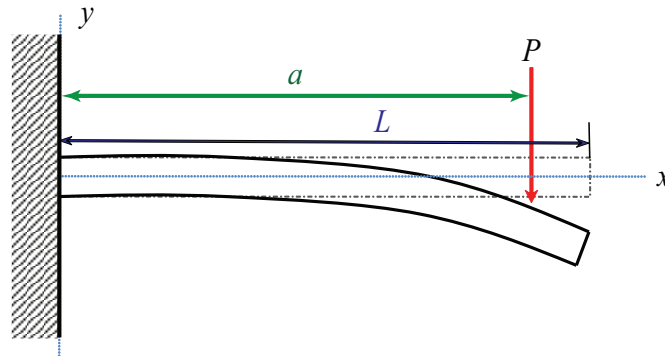


Figure 2.11: The sketch of the cantilever from the experiment

From Fig. 2.13, we see that the bending moment is a function of x because it is equal to the torque about the neutral axis of any cross section. we neglect the weight of the cantilever because the weight is very small and not in the same direction with force P . Then the bending moment at x is

$$M(x) = -P(a - x) \quad (2.17)$$

where $M(x)$ is the bending moment at x position, L is the original length of the cantilever from the clamping point, x is any position on the cantilever, a is the length between applying force point and clamping point.

2.3.4 The deflection of the cantilever

From Fig. 2.12, if θ is very small, $\tan \theta \approx \theta = \frac{dy}{dx}$

$$\frac{d\theta}{dx} = \frac{d^2y}{dx^2} \quad (2.18)$$

$$\frac{1}{\rho} = \frac{d\theta}{ds} \quad (2.19)$$

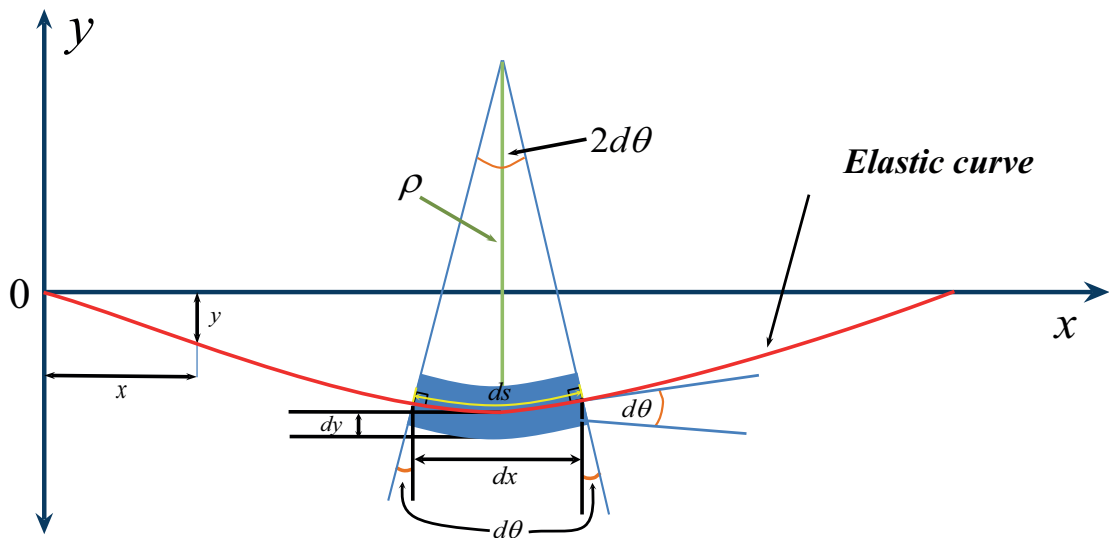


Figure 2.12: The elastic curve

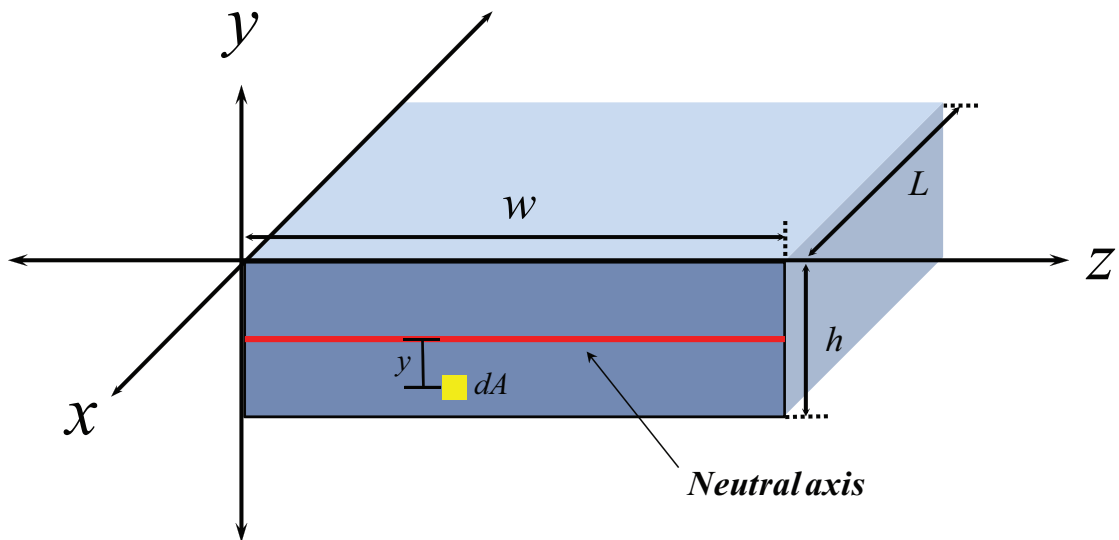


Figure 2.13: Cross section of the cantilever

$$ds \approx dx \quad (2.20)$$

$$\frac{1}{\rho} = \frac{d^2y}{dx^2} \quad (2.21)$$

From equation (2.9) and (2.19)

$$\frac{d^2y}{dx^2} = \frac{M}{EI} \quad (2.22)$$

The deflection equation of the cantilever can be rewritten by substituting equation (2.17) and (2.13) in equation (2.22) as shown below.

$$\frac{d^2y}{dx^2} = \frac{-P(a-x)}{E\frac{h^3w}{12}} \quad (2.23)$$

$$\int \frac{dy}{dx} = -\frac{12}{Eh^3w} \int P(a-x)dx \quad (2.24)$$

$$y = -\frac{6}{ELh^3w} \int \int P(a-x)dx dx \quad (2.25)$$

From Fig. 2.12, the curvature and deflection of the cantilever are equal to zero, the boundary conditions are

$$\left. \frac{dy}{dx} \right|_{x=0} = 0 \quad (2.26)$$

and

$$y(0) = 0 \quad (2.27)$$

where these conditions are applied to equation (2.24), the deflection of the cantilever is

$$y = -\frac{2Px^2}{Eh^3w}(ax-x) \quad (2.28)$$

The force from the cantilever is

$$P = -\frac{Eh^3wy}{2x^2(ax-x)} \quad (2.29)$$

where E is the Young's modulus of borosilicate glass, h is the thickness of the cantilever, w is the width of the cantilever, y is the deflection range of the cantilever.

2.3.5 The stress of the cantilever

To calculate the stress of the cantilever we substitute the force P (equation (2.29)) in to the bending moment (equation (2.17)), the bending moment becomes

$$M(z) = -\frac{Eh^3wy}{2x^2(ax-x)}(a-x) \quad (2.30)$$

We put this new form of bending moment in equation (2.16). Then the strain equation of the cantilever is

$$\sigma = \frac{12rP(a-x)}{h^3w} \quad (2.31)$$

where r is the constant range from neutral axis of cantilever.

2.3.6 The strain of the cantilever

We substitute the stress with equation (2.31) and substitute in to Young's modulus (equation 2.3).

$$\varepsilon = \frac{\sigma}{E} = \frac{r}{\rho} \quad (2.32)$$

Then, the strain of our cantilever is

$$\varepsilon = -\frac{6ry}{x^3(a-1)}(a-x) \quad (2.33)$$

2.3.7 The simulation of beam deflection

The simulation of the cantilever beam is done by using Microsoft excel 2007. This simulation was programmed by Mr. Pakorn Yimpa [26]. The beam deflection analysis can be done by plugging our experimental parameters of the actual strain gauge (see Fig. 4.8). The parameters used this program are shown in Fig. 2.14. The detail of each parameter in Fig. 2.14 is shown in Table 2.1. To use this simulation program, we use the some parameters from the table in to this program such as a, h, w, P, dx, I, E and b (See details in Appendix A). After putting all real parameters, then the program asks the user to increase position in x axis by dx and starts to plot 3 type automatically at the same time. This program simulates 4 equations and plots 3 types of graphs as follows.

1. For the deflection and the position graphs, equation (2.28) was used this graph.
2. For stress and position graph, equation (2.31) was used graph.
3. For strain and position graph, equation (2.33) was used graph.

We various forces which are inferred from the deflection distance indicated by the micrometer. We measured the deflection distance near the end of the cantilever. The point of the interest cantilever is fixed at a distance b from the clamping point. In the real experiment, we probed the capacitor located at this point.

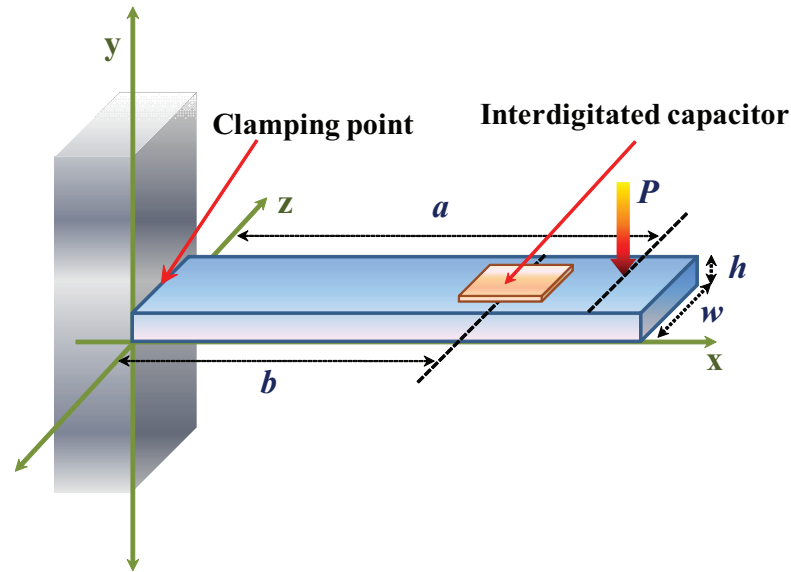


Figure 2.14: The diagram of the cantilever consisting of an interdigitated capacitor

Table 2.1: The parameters for simulation program for the interdigitated capacitor at $x = 0.7$ cm

Input parameter	Value	Unit
Range from clamping point to applying force position (a)	1	cm
Thickness of cantilever (h)	0.016	cm
Width of cantilever (w)	0.4	cm
Initial value of applying force (P)	0.00890	N
Step of increasing range on cantilever (dx)	0.05	cm
Moment of inertial cross section around neutral axis (I)	1.36533×10^{-15}	m^4
Young's modulus of borosilicate glass (E)	6.3×10^{15}	Pascal
The interesting interdigitated capacitor position (b or x)	0.5 or 0.7	cm

We used the equation of the beam deflection (Equation 2.28), stress and strain of the cantilever (Equation (2.31) and (2.33)) at any position on the cantilever by variation of x by dx . The simulation was done at 2 positions $x = 0.7$ cm and $x = 0.5$ cm. The simulated results of the beam deflection at $x = 0.7$ cm are shown in Fig. (2.15), (2.16), (2.17).

The deflection of beam cantilever is increased a function of force and the maximum deflection of the beam occurs at the end of cantilever as shown in Fig. 2.15. The maximum deflection of cantilever is 1.9×10^{-4} m. at the force of 0.0490 N.

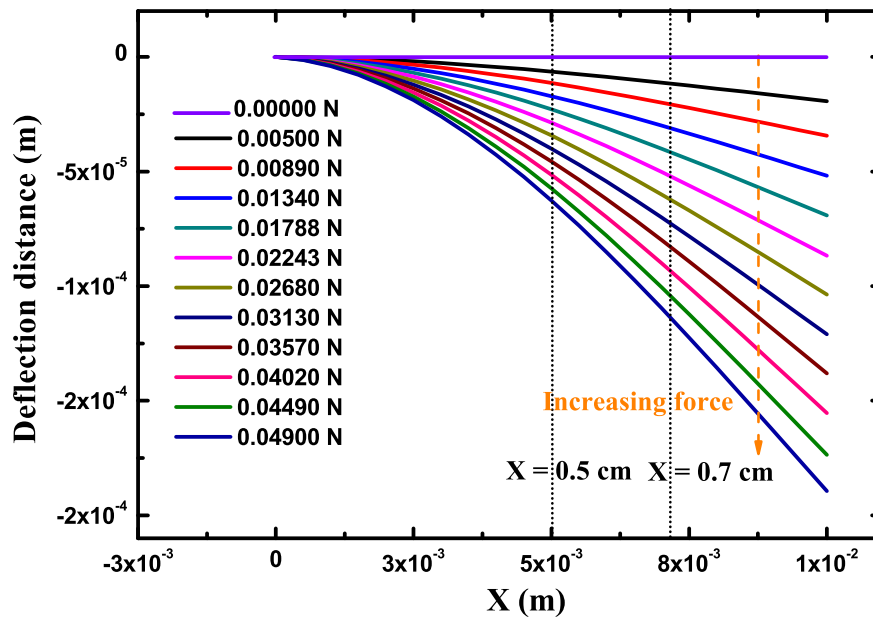


Figure 2.15: The simulation of beam deflection of the borosilicate cantilever

The stress of the beam cantilever increased with of the applied force and the maximum stress of the beam is performed at the clamping point of cantilever as shown in Fig. 2.16. The maximum stress of the cantilever is 2.88×10^7 Pascal at the force 0.0490 N.

The strain of the beam cantilever increased with the applied force and the maximum stress of the beam is performed at the clamping point of cantilever as shown in Fig. 2.17. The maximum stress of cantilever is 2.51×10^{-4} at the force 0.0490 N.

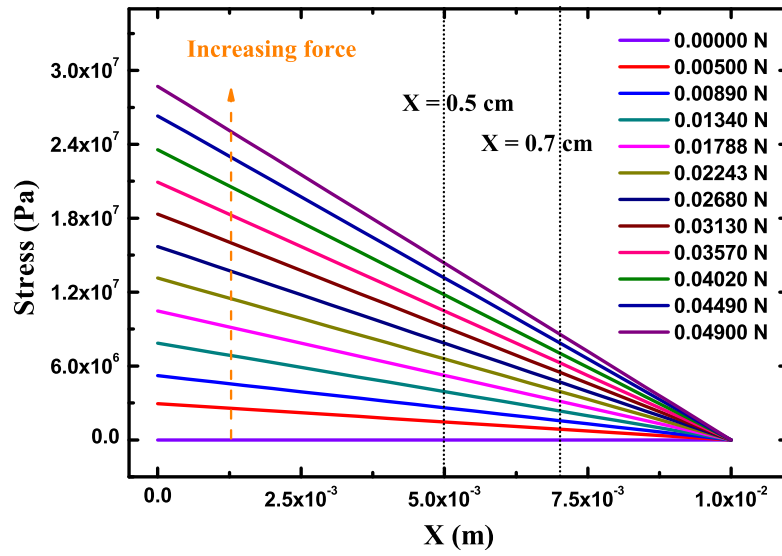


Figure 2.16: The stress of the borosilicated cantilever from simulation

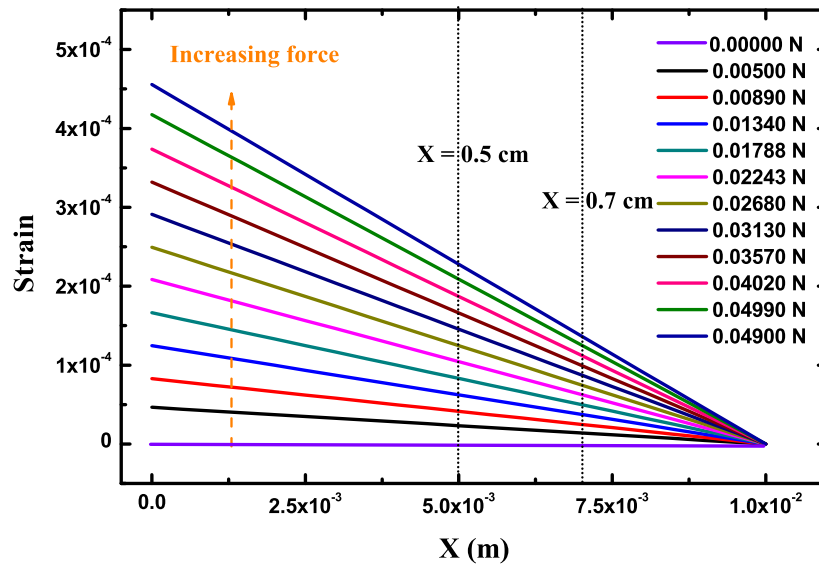


Figure 2.17: The strain of the borosilicated cantilever from simulation

2.4 Dielectric properties

2.4.1 Dielectric constant

Since in my thesis I deal with barium titanate and barium strontium titanate which are dielectric materials, I will introduce the polarization the dielectric constant and the dielectric loss in this section. A dielectric material is classified as an insulator which can be affected by an electric field (\vec{E}). In any insulator, the positive and negative charges are coupled together to become dipoles (See Fig. 2.18). After we apply an electric field to the dielectric material, an electric dipole moment is induced in the molecules of the material.

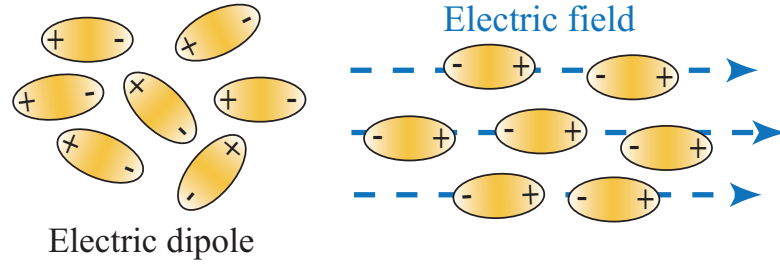


Figure 2.18: Electric dipoles in electric field

$$\vec{p} = \sum_i q_i \vec{r}_i \quad (2.34)$$

where q_i is the charge associated with the i th particle and \vec{r}_i is the displacement vector of the particle with respect to the origin. The number of the dipole moment per unit volume is called polarization (\vec{P}) which proportional to the field followed by

$$\vec{P} = \varepsilon_0 \chi_e \vec{E} \quad (2.35)$$

where χ_e is the electric susceptibility of the medium which depends on the microscopic structure of the any substance and ε_0 is permittivity of free space. The permittivity of the material (ε) is defined by

$$\varepsilon \equiv \varepsilon_0(1 + \chi_e) \quad (2.36)$$

where $\varepsilon_0 = 8.85 \times 10^{-12} \text{ C}^2/\text{N} \cdot \text{m}^2$. We rearrange equation (2.36) and define a new variable so

$$\varepsilon_r \equiv 1 + \chi_e = \frac{\varepsilon}{\varepsilon_0} \quad (2.37)$$

This new constant ε_r is called relative permittivity or dielectric constant of the material. Thus, we can conclude that dielectric material can be polarized. This magnitude of this is here identified by the dielectric constant which depends on the type of material.

2.4.2 Dielectric loss

The dielectric constant of the material can be defined in the term of complex dielectric constant (ε^*)

$$\varepsilon^* = \varepsilon' + i\varepsilon'' \quad (2.38)$$

where ε' is the real part of the dielectric constant of material, ε'' is the imaginary part which is considered to be the energy loss in dielectric material. This energy can be converted to heat energy. The loss factor or loss tangent is related to

$$\tan \delta = \frac{\varepsilon''}{\varepsilon'} \quad (2.39)$$

where δ equal to zero in ideal capacitor or no losses in its dielectric. Dielectric loss is one property we characterized for our BTO and BSTO coplanar capacitors (See section 4.2). The capacitance measurements and the dielectric response of films are described in section 4.3 and 5.4, respectively.

2.4.3 Conversion from capacitance to dielectric constant

In practice, we can not measure the dielectric constant directly but we obtained by conversion from the capacitance of the film measured with an LCR

meter. The detail of the capacitance measurements is shown in section 4.3. This conversion can be done by using this expression [27].

$$\varepsilon_f = \varepsilon_s + \frac{C - K(1 + \varepsilon_s)}{K \left(1 - e^{\left(\frac{-4.6h}{G+W}\right)}\right)} \quad (2.40)$$

where ε_f is the dielectric constant of the film, ε_s is the dielectric constant of borosilicate glass = 4.6 [28], K is a constant depending on the size of interdigitated finger in pF (See equation 2.42), L is the interdigitated finger length in unit m, h is the thickness of the film in micron, G and W are the size of gold finger (See Fig. 2.19), C is the measuring capacitance per unit finger length per length of electrode in pF, which is given by

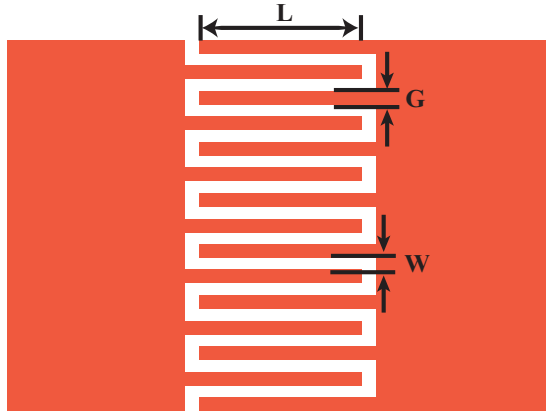


Figure 2.19: Interdigitated pattern for dielectric constant conversion

$$C = \frac{C_m}{LN} \quad (2.41)$$

where C_m is measured capacitance in unit pF from the experiment, L is the interdigitated finger length in unit m, N is the number of golden finger of the electrode, The constant K can be calculated by

$$K = 6.5\left(\frac{G}{G+W}\right)^2 + 1.8\left(\frac{G}{G+W}\right) + 2.37 \quad (2.42)$$

where Equations (2.40)-(2.42) were derived by Farnell et al. [29] using an analytical model for interdigital electrode configuration in Fig. 2.19. The value of G , W , L are obtained from the interdigitated pattern(See Fig. 4.8) The parameter $G = 100 \mu\text{m}$, $W = 100 \mu\text{m}$, then $K = 4.535 \text{ pF}$. The number of fingers (N) is 14, the interdigital finger length is $G = 1500 \mu\text{m}$. The thickness of the films (h) are obtained from field emission scanning electron microscopy (FSEM). The cross section of FSEM picture of barium titanate thin film (BTO#1) and barium strontium titanate thin film (BSTO#3) is shown in the Fig. 2.20 the thickness of this thin film is 712 nm. The film growth conditions including the film numbers can be seen in Table 4.1 and 4.2.

The cross section of barium strontium titanate thin films is taken from $\text{Ba}_{0.35}\text{Sr}_{0.65}\text{TiO}_3$ (See table 4.1 and 4.2 in subsection 4.1.2). The thickness of $\text{Ba}_{0.35}\text{Sr}_{0.65}\text{TiO}_3$ thin film is found to be 553 nm. From Fig. 2.20 and Fig. 2.21, BTO thin film is thicker than BSTO. The grain size of BTO film is smaller than $\text{Ba}_{0.35}\text{Sr}_{0.65}\text{TiO}_3$.

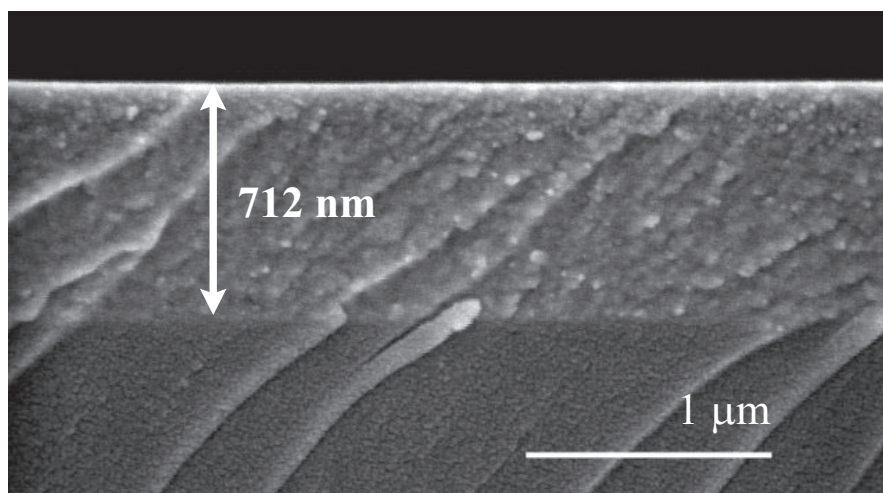


Figure 2.20: The image of a cross section of BaTiO₃ thin film taken from FSEM

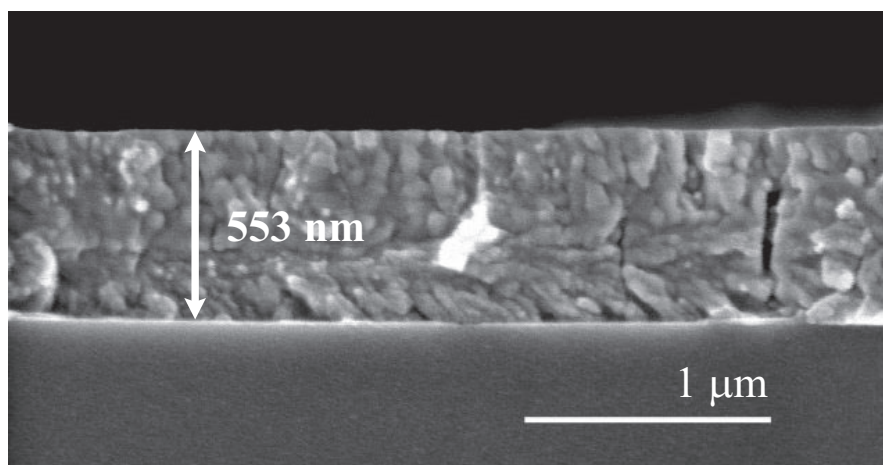


Figure 2.21: The image of a cross section of Ba_{0.35}Sr_{0.65}TiO₃ thin film taken from FSEM

CHAPTER III

CHARACTERIZATION TECHNIQUES

The main characterization techniques used in this thesis for examination of the properties of barium titanate and barium strontium titanate thin films are summarized in this chapter. The crystallinity and the crystal structure of the films are examined with X-ray diffractometer. The composition and stoichiometry of the films are examined by wavelength dispersive X-ray spectrometer.

3.1 X-ray diffractometry

3.1.1 The X-ray source

X-rays were first discovered by Wilhelm Conrad Röntgen (German Physicist) in 1895. He found that these rays were invisible, traveled in straight lines and affected photographic film as the visible light. Moreover, they were much more penetrating than the light and could pass through human body, wood, thick piece of material, and other opaque objects. In 1912, the phenomenon X-ray diffraction by crystals was discovered which is the new method for investigation the structure of matter. X-rays diffraction phenomena can directly reveal details of internal structure in material of the order 10^{-10} m in size.

X-rays are electromagnetic radiation of exactly the same nature as visible light but shorter wavelength. The unit of measurement in the X-ray region is the angstrom (Å). The wavelength of the X-ray region is in approximately 0.5-120 Å range. X-rays used in diffraction are in the range of 0.5-2.5 Å which is called

the short wavelength X-rays. Generally, there are 2 types of X-rays: continuous X-rays and characteristic X-rays.

The continuous X-rays are produced when electrons were decelerated quickly after obtaining enough kinetic energy and collide with others atoms. X-rays are produced in an X-ray tube with an electron source. The high voltage is used to accelerate electron to hit the anode with very high velocity and then X-rays both continuous X-rays and characteristic are emitted. The kinetic energy of electron (KE) is given by

$$KE = eV = \frac{1}{2}mv^2 \quad (3.1)$$

where m is the mass of the electron (9.1×10^{-31} kg) and v is the velocity of the electron. The X-rays coming from the target consist of different wavelength. The variation of intensity depends on the voltage across the tube. The relation between intensity and wavelength of X-ray is shown in Fig. 3.1.

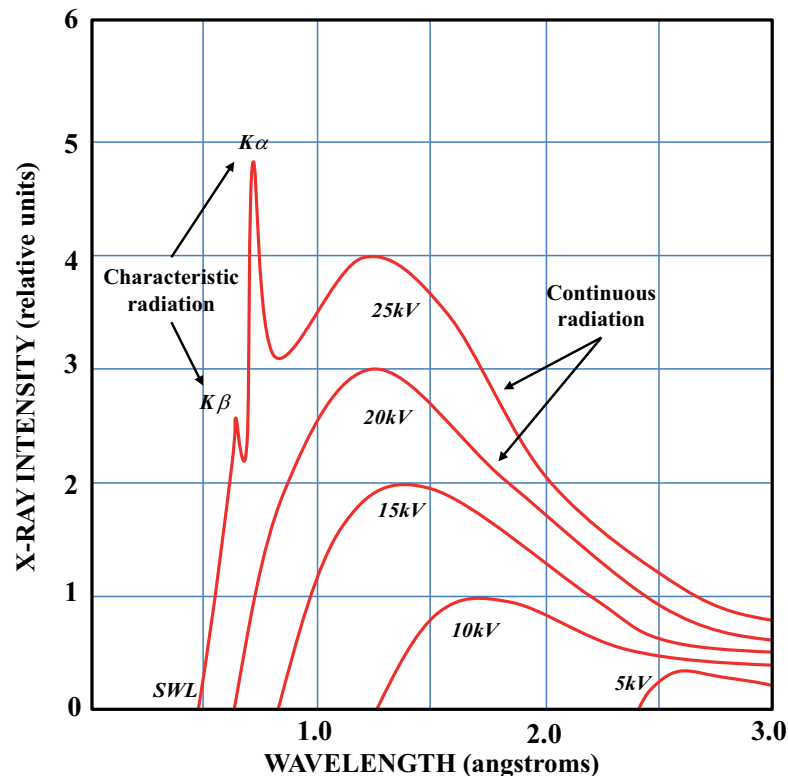


Figure 3.1: X-ray spectrum of molybdenum as a function of applied voltage

The zero intensity at the shortest wavelength is called short wave length limit (λ_{SWL}). Increasing the voltage makes the λ_{SWL} shorter. The continuous X-rays are represented by the broad curves at which sometimes they are called Bremsstrahlung. Some of electrons are suddenly stopped and release energy when electrons transfer all of electric potential energy into photon energy assuming no losing energy then the equation becomes

$$eV = h\nu_{\max} \quad (3.2)$$

$$eV = \frac{hc}{\lambda_{SWL}} \quad (3.3)$$

$$\lambda_{SWL} = \frac{hc}{eV} \quad (3.4)$$

where ν is the frequency of X-ray, e is the charge of an electron, V is the applied voltage, h is the planck constant and c is the light velocity (3×10^8 m/s). From Fig. 3.1, the total energy emitted per second proportional to the area under the curve, the atom number Z of target and the tube current i , so the total X-ray intensity is given by

$$I_{cont} = AiZV^m \quad (3.5)$$

where A is a proportional constant and m is a constant with a value of about 2. We can conclude from equation 3.5 that the intensity of the continuous X-ray spectrum depends on the type of material of target. We use characteristic X-ray in X-ray diffractometry technique. This type of X-ray occurs when the voltage on X-ray tube is raised over a normal critical value, the characteristic X-ray of the target appears as narrow peak of intensity (See Fig. 3.1) at which the wavelength depends on the type of target. This phenomena is called characteristic lines. Let's consider on the sketch of electronic transitions in an atom in Fig. 3.2.

The characteristic X-ray is occur when one of electron with enough kinetic energy hits the target and knock an electron out of inner-shell, then one of the outer electron fall in the inner-shell immediately and emit the energy in the form of a well definite X-ray wavelength. The transition of electrons from L-shell to K-shell produced K_α X-ray and from the M-shell to K-shell produces K_β X-ray.

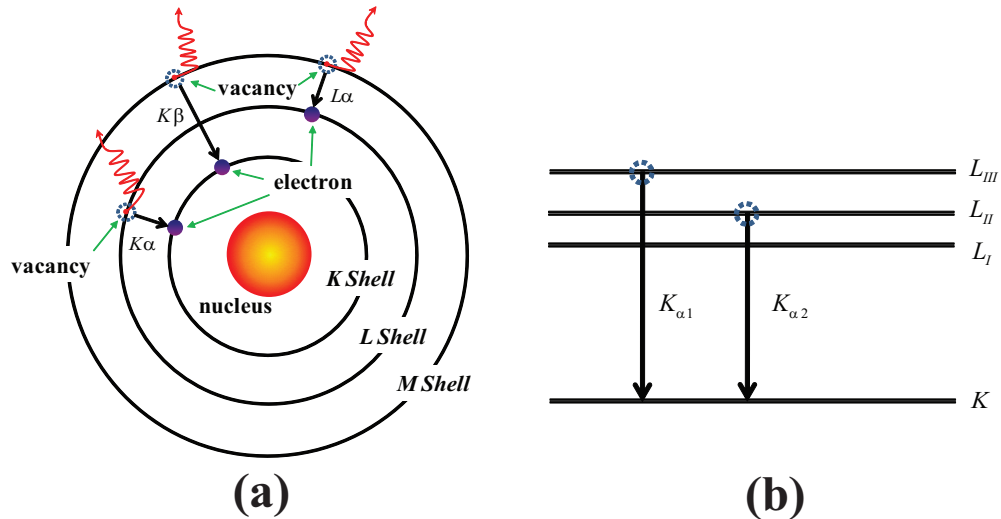


Figure 3.2: (a) The schematic of electronic transitions in an atom (b) Excitation and emission process indicated by arrows

The emissions of these two type of characteristic X-rays appear as two sharp peaks in Fig. 3.1.

This X-ray type have several sets referred as K,L,M for any element. From Fig. 3.2(b), $K_{\alpha 1}$ and $K_{\alpha 2}$ are released by the falling of electron from L_{III} and L_{II} to K shell, respectively. $K_{\alpha 1}$ and $K_{\alpha 2}$ have wavelengths close to another (See Table 3.1 and 3.2) but $K_{\alpha 1}$ wavelength is shorter. The intensity of K_{α} is higher than $K_{\beta 1}$ (See Fig. 3.1). The common targets used in research work are Cu and Mo targets. Table 3.1 and 3.2 show the X-ray wavelength of Mo $K_{\alpha 1}$ and Cu $K_{\alpha 1}$ respectively. In this thesis, we use an X-ray diffractometer with Cu $K_{\alpha 1}$ X-ray wavelength which is equal to 1.540562 Å (See section 3.1.3).

Table 3.1: The characteristic wavelength generated by Mo [11]

Type	Wavelength
$K_{\alpha 1}$	0.70926 Å
$K_{\alpha 2}$	0.71354 Å
$K_{\beta 1}$	0.63225 Å

Table 3.2: The characteristic wavelength generated by Cu [11]

Type	Wavelength
$K_{\alpha 1}$	1.540562 Å
$K_{\alpha 2}$	1.544390 Å
$K_{\beta 1}$	1.392218 Å

3.1.2 Bragg's law

From the previous subsection, we know that X-rays have two wavelength regions: short wavelength region (0.5-2.5 Å) and long wavelength region (2.6-120 Å). Let's consider the sketch of crystal planes consisting of periodic structure from arrangement of atoms or molecules that form a crystal lattice. In any crystal structure, we know that it consists of numerous planes of atoms lying in many different directions. We represent an atomic plane by connecting points by a line as shown in Fig. 3.3. The distance between each atomic plane is called d-spacing. The wavelength of short wavelength X-rays are compatible to the atomic spacing in solid materials. I will derive Bragg's law and use it to determine the lattice constant of the resulting films.

When a bundle of X-ray beam strikes on a crystal plane of material, every atom within a plane acts as a scattering center and emit a secondary wave. The secondary wave performs as a reflected wave. If the path difference between ray 1' and ray 2' from consecutive planes multiple integer number of X-ray wavelength

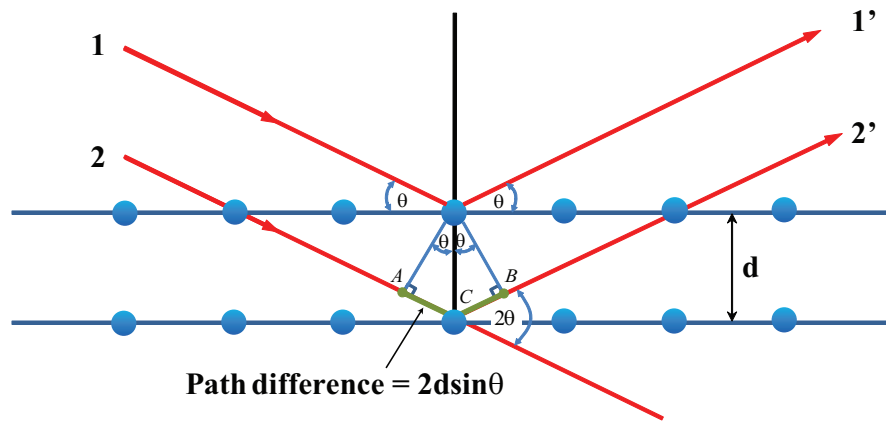


Figure 3.3: Diffraction of X-ray by a crystal

($\Delta\lambda = n\lambda$), constructive interference will occur. In the other hand, if the phase difference is not equal to a multiple of X-ray wavelength ($\Delta\lambda \neq n\lambda$), destructive interference will occur. From Fig. 3.3, we find that

$$|AC| = d \sin \theta \quad (3.6)$$

The path difference between ray 1' and ray 2' is

$$|ACB| = 2d \sin \theta \quad (3.7)$$

The constructive condition is supported when the path difference equals to a whole multiple number n of the wavelength so we obtain:

$$|ACB| = n\lambda \quad (3.8)$$

From equation (3.7) and (3.8), we can write the Bragg's law in the form:

$$2d \sin \theta = n\lambda \quad (3.9)$$

where n is reflection order ($n=1,2,3,\dots$) If we know the wavelength λ , we can calculate the crystalline structure and the plane distance d which used to calculate the lattice constant of our thin films.

3.1.3 The X-ray diffractometer

After the the characteristic X-ray from an X-ray tube is scattered from atoms on any lattice planes, the scattering X-ray is detected by an detector equipped with the X-ray diffractometer machine. The X-ray detector can generate an electrical signal proportion with diffracted X-ray intensity from the sample. The detector is VANTEC-1 detector (Super speed detector) and the model of X-ray diffractometer is Bruker AXS Model D8 discovery. The target of the X-ray tube is Cu with voltage of 40 kV and current of 40 mA. The wavelength of characteristic X-ray from this X-ray tube is 1.5406 Å. The angle of the movement detector between 20-80 degree with 0.02 degree/step of increment. The scan speed is 0.5 sec/step.



Figure 3.4: The X-ray diffractometer

This diffractometer system in our work is controlled by the computer system with XRD commander program which can show the diffraction pattern of our films in real time system collection of the raw data is in the form of 2θ and intensity which can be saved in the .xls file of microsoft excel program.

3.2 Wavelength dispersive X-ray spectroscopy

A wavelength dispersive spectrometry (WDS) is the electron probe spectroscopy technique which uses the characteristic X-rays generated by individual elements of the sample. These X-rays are then selected using analytical crystal with specific lattice spacing. This technique is developed to measure precisely X-ray intensities for determination of the chemical composition accurately. WDS technique is the complementary of energy dispersive spectroscopy (EDS) but WDS spectrometry have higher significant spectral resolution. Many scanning electron microscope (SEM) and Electron probe analyzer (EPMA) have EDS or WDS system mounted with them. The schematic diagram of WDS schematic is shown in

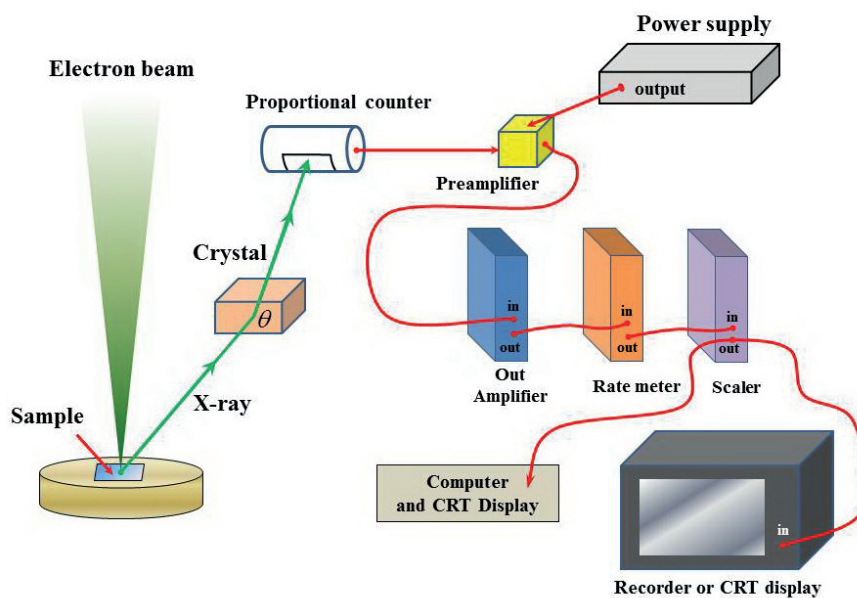


Figure 3.5: Schematic representation of a wavelength dispersive spectrometer and associated electronics

Fig. 3.5 which consists of many part inside WDS system such as crystal, proportional counter, preamplifier, amplifier, rate meter, scaler and computer with CRT monitor. In order to understand WDS characterization technique, we have to focus on WDS focal system, working of analytical crystal and detector on the

focusing circle within the WDS spectrometer.

From Fig. 3.5, a beam of electrons is accelerated in an evacuated electron collum of EPMA or SEM with 15-20 kV potential difference to generate characteristic X-rays from an elements on our sample. A tiny fraction of all X-rays is emitted at the proper take off angle Ψ from sample and encounter the analytic crystal. Since characteristic X-rays from each element has a different wavelength, changing the slope of the crystal in the spectrometer to the specific angle θ in order to adjust to wavelength characteristic of another element. Only some part of X-rays that satisfy Bragg's law, $2d\sin\theta = n\lambda$ as mentioned in equation 3.9 enter the crystal. Different analytical crystals, with $2d$ where d is lattice spacing varying from 2.0 to 2.5 Å, are used to diffract various ranges of wavelength that may correspond to the primary emission lines of various elements.

The sample crystal and detector must lie on the focusing circle and remain on it for all wavelengths. Because the sample and take off angle are fixed, the analytical crystal and detector must move together on focusing circle as shown in Fig. 3.6. A single wavelength X-rays is passed to into a gas-filled proportional counting tube detector, which has a thin wire of tungsten with 1-2 kV potential. The X-rays are absorbed by gas molecules in the detector tube and then a photoelectron is ejected by each atom absorbing an X-ray.

Within our sample, the X-ray intensities of each interesting element enter the detector. The electrical signals from detector are amplified but these signals are fully with noise. Consequently, the noise pulse must be rejected by the special electronic circuit. Only pulses with a certain range of energies are allowed to enter the scaler electronics for counting. The count rates are compared to those of standards value of the interesting element. This comparison process is performed within a computer program that take the raw counting rates of each element to compared with standard and displays the results as a function of the weight percent of the oxide or elements.

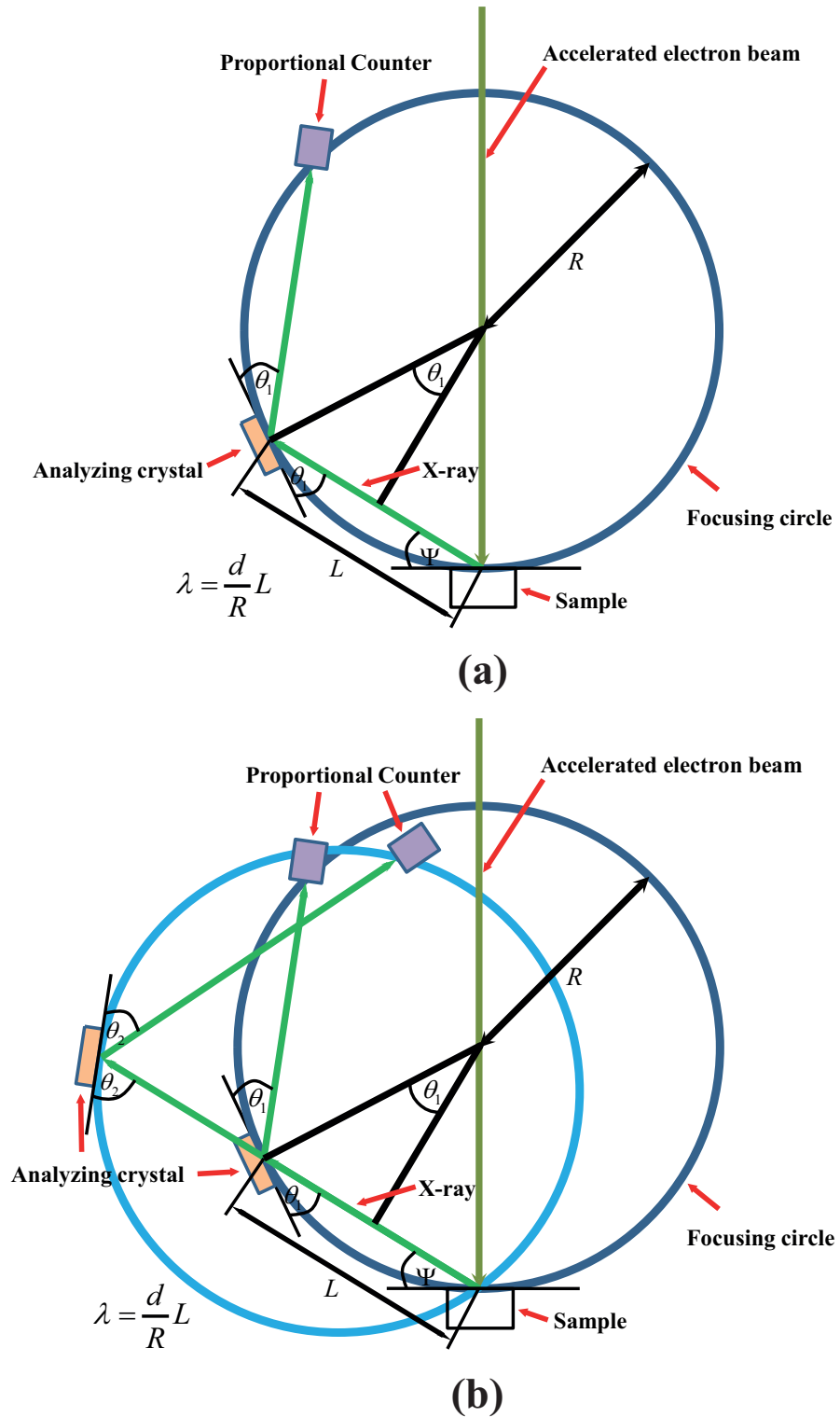


Figure 3.6: (a) Fully focusing wavelength-dispersive spectrometer (b) Movement of the focusing circle to change the diffraction angle of WDS

CHAPTER IV

EXPERIMENTAL METHODS

This chapter describes how to prepare barium titanate and barium strontium titanate films at the different growth conditions by a sol-gel spin technique. Then I will describe how we fabricated the individual coplanar capacitors and the strain gauge by depositing gold electrode using a DC sputtering machine and by dicing the films using dicing saw. The individual coplanar capacitors are brought to measure capacitance via LF impedance analyzer (LCR meter) as a function of frequency. The strain gauge is used as a strain to frequency converter through oscillator circuit.

4.1 Film preparation on cleaned substrates

Barium titanate and barium strontium titanate thin films are studied in this thesis. This sections shows the detail about application of sol-gel spin coating technique for synthesis both types of thin films.

4.1.1 Preparation of barium titanate (BTO) precursor

The main chemicals for of barium titanate precursor are barium acetate ($\text{Ba}(\text{CH}_3\text{COO})_2$), acetic acid (CH_3COOH), titanium butaoxide ($\text{Ti}(\text{CH}_3\text{CH}_2\text{CHO})_4$) and methanol. Barium acetate was first dissolved in acetic acid by magnetic stirring on the hot plate. Titanium butaoxide was mixed in methanol and then barium

acetate solution was quickly added. The whole mixture was stirred at room temperature until the homogeneous solution with yellow color was obtained then the precursor was kept in an electronic dry cabinet until it precipitated for two days. All steps in BTO precursor preparation is shown in Fig. 4.3.

4.1.2 Preparation of barium strontium titanate (BSTO) precursor

In order to prepare barium strontium titanate precursor, an appropriate amount of strontium acetate ($(\text{CH}_3\text{CO}_2)_2\text{Sr}$) was used in addition to barium acetate ($\text{Ba}(\text{CH}_3\text{COO})_2$), acetic acid (CH_3COOH), titanium butoxide ($\text{Ti}(\text{CH}_3\text{CH}_2\text{CHO})_4$) and methanol. First, various portions of barium acetate and strontium acetate were mixed together in acetic acid by magnetic stirring on the hot plate. Titanium butoxide and methanol were mixed together and then barium-strontium acetate solution is quickly added in titanium butoxide mixture. The whole mixture was stirred at room temperature until it changes in to homogeneous solution. The precursor was then kept in an electronic dry cabinet and let it precipitated for two days. Note that this procedure is needed to be done to obtain only clear solution for film deposition. All steps in BSTO precursor preparation are shown in Fig. 4.3.

The stoichiometry of $\text{Ba}_x\text{Sr}_{1-x}\text{TiO}_3$ is done by changing the weight ratio of barium acetate and strontium acetate contents. In film preparation process, the films were prepared with 4 conditions followed by the ratio between barium acetate and strontium acetate. The amount of barium acetate and strontium acetate used to prepare barium-strontium precursor can be seen in Table 4.2. The corresponding atomic ratios in the films are shown in Table 4.1 and 4.2.

In every thin film preparation technique, the substrate must be very cleaned to avoid any contamination that might occurred during the film process. In this thesis work, flexible glass substrate was chosen to be the substrates used in the

Table 4.1: Type of BTO and BSTO thin films with different growth conditions

Type of film	Annealing temperature and time for each layer	Layers Annealed for another 2 hr after all layers finished	Total annealing time	
BTO#1	1 hr, 650°C	6L	√	8 hr
BTO#2	1 hr, 650°C	6L	-	6 hr
BSTO#3	1 hr, 650°C	6L	-	6 hr
BSTO#4	1 hr, 650°C	6L	-	6 hr
*BSTO#5	1.5 hr, 650°C	7L	-	10.5 hr

Table 4.2: Type of BTO and BSTO thin films with different stoichiometry

Type of film	Barium acetate(g)	Strontium acetate(g)	Stoichiometry
BTO#1	2.6	0	BaTiO ₃
BSTO#2	2.167	0.433	Ba _{0.8} Sr _{0.2} TiO ₃
BSTO#3	0.433	2.167	Ba _{0.35} Sr _{0.65} TiO ₃
BSTO#4	1.95	0.65	Ba _{0.69} Sr _{0.31} TiO ₃
*BSTO#5	0.433	2.167	Ba _{0.35} Sr _{0.65} TiO ₃

*The film on deformed substrate (See in Fig. 5.1)

strain gauge application. First, borosilicate glass substrates were put vertically in a teflon holder and cleaned in acetone by the aid of ultrasonic bath for 8 minutes. Second, all substrates in the holder were transferred to containing in methanol followed by DI water, and ultrasonic for 16 mins for each step. After that, each borosilicate glass substrate was dried by nitrogen gas (N₂) and was ready to use for depositing film on it.

4.1.3 Film deposition

The cleaned borosilicate glass substrate was placed on vacuum chuck. The spin coater machine (Spin coater model p6700 series) was used to control for the spinning speed. The BTO or BSTO precursor about $90 \mu\text{l}$ was dropped on a cleaned borosilicate glass using a pipet to obtain the exact amount of solution every time. The substrate was placed on the vacuum chuck. From Fig. 4.1, the spinning speed is increased slowly until the speed was about 800 rpm (revolutions per minute) and holding for 10 seconds then the spinning speed is suddenly up to 3000 rpm and holding for 30 seconds. The spinning chuck is suddenly stopped due to the finishing of the spinning program.

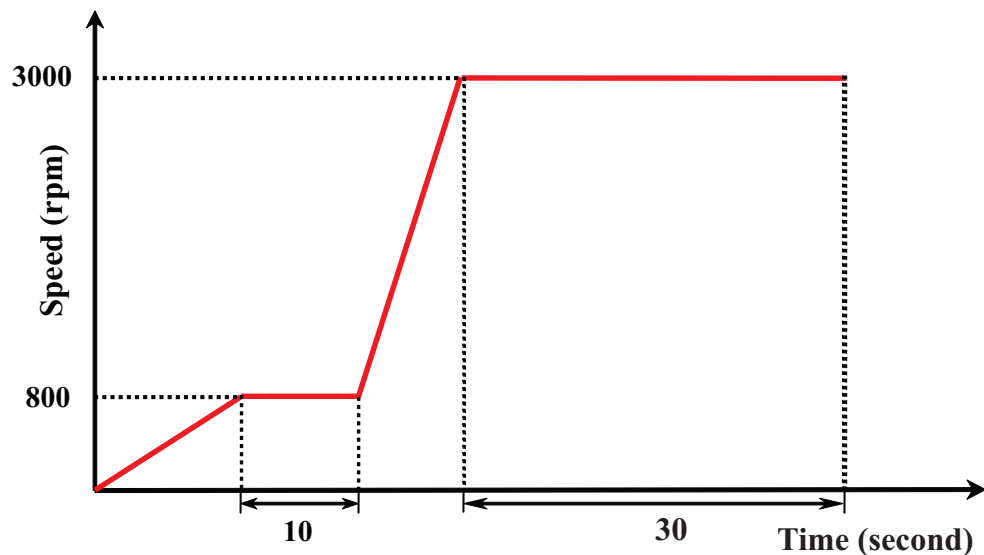


Figure 4.1: The speed diagram of spin coating process

After finishing spinning process, I carried the substrate on the edge using a pair tweezers to preheat at 120°C about 15 min. The preheat treatment is important for removal of organic residues and the generation of water from the condensation reaction. Then, the film is annealed in a programmable furnace (Carbolite elf 1/4) at a high temperature for 1 hr. Since the substrates are thin (0.16 mm), a low heating rate ($10^{\circ}\text{C}/\text{min}$) was used for avoiding of the bending problem the substrates. I also varied the annealing temperature and the annealing time. First, I tried with the annealing temperature of 650°C for 1.5 hr. It turned

out that this growth condition, the substrate was bent (See in section 5.1) For preventing the cracking the films, the temperature of the furnace must be cooled down slowly. The heating diagram of annealing process is shown in Fig. 4.2.

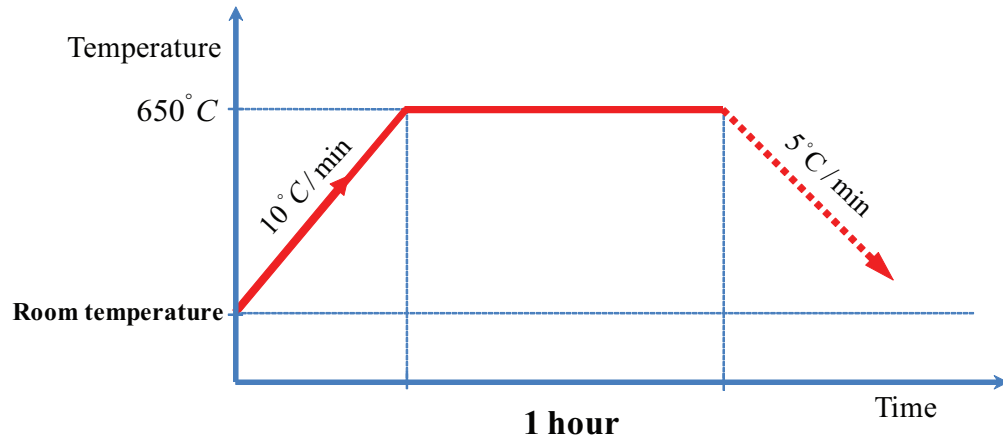


Figure 4.2: The temperature diagram of annealing process

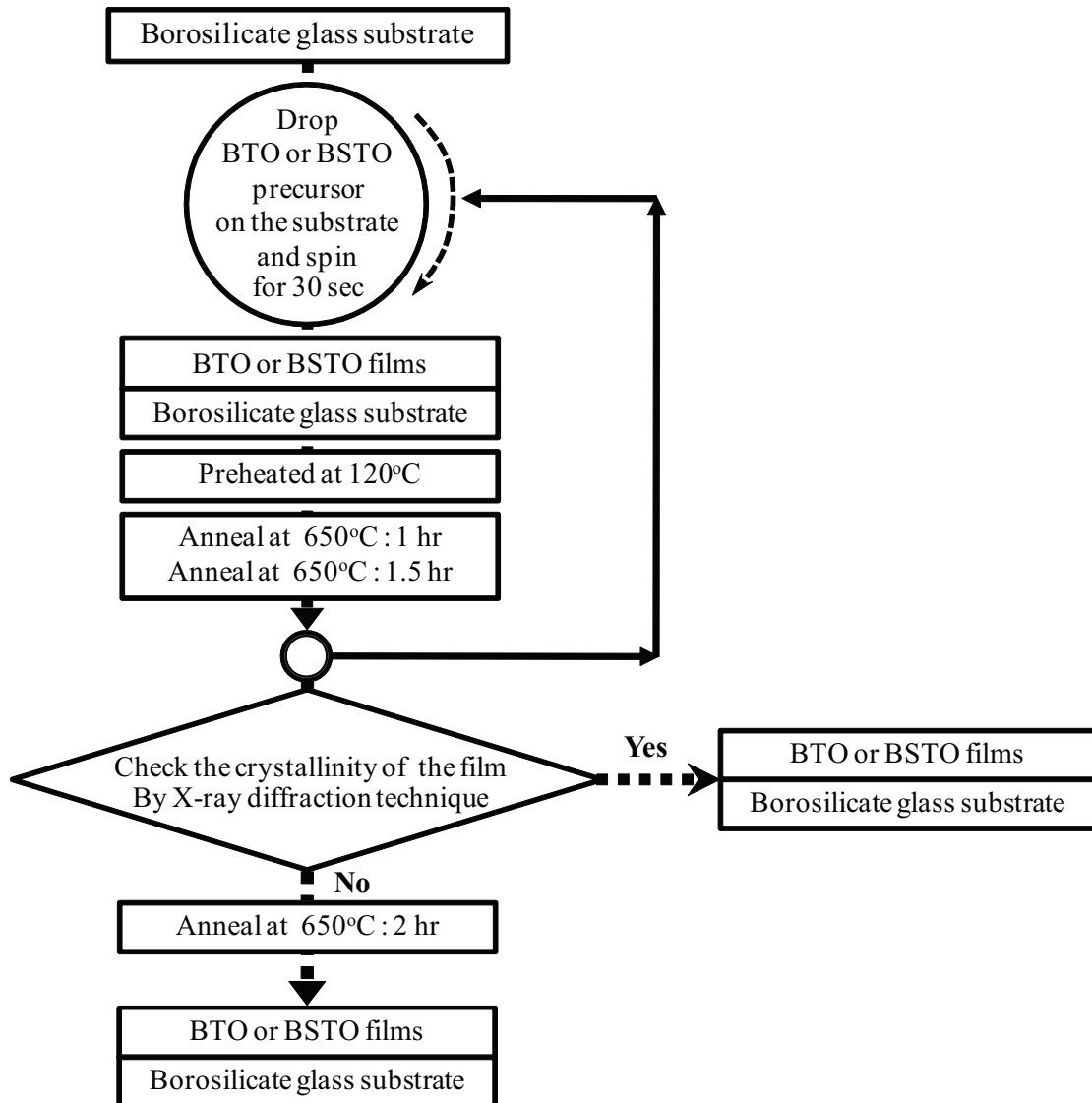


Figure 4.3: The process of BTO and BSTO film preparation

4.2 Device fabrication

In DC sputtering process, the interdigitated nickel mask is put on the top of thin film before sputtering metal targets. Several small magnets were used to attach the nickel mask with our thin film closely (See Fig. 4.4 (b)). Chromium (Cr) target was first sputtered on thin films and followed by gold (Au). Both magnets and the mask with the film sample between put in the sputtering machine (See Fig. 4.4 (a)). The figure of the interdigitated mask is shown in Fig. 4.4 (b).

Since the film with gold electrode came out as an arrays of capacitors, dicing saw was used to dice to individual coplanar capacitors and individual arrays of capacitors. The dicing process was done using a diamond blade equipped with dicing saw machine (Model Vectus) as seen in Fig. 4.6(a) and 4.6(b). The gap width of the coplanar capacitor is $100 \mu m$. The finger length is about 27.8 mm at which the finger length is $1700 \mu m$, and the overall size of $3 \times 4 \text{ mm}$ (Fig. 4.8(b)). For the cantilever, it consists of 4 capacitors if they were laid out perfectly with overall size of $20.1 \times 4 \text{ mm}$. The cantilever will be called a capacitive strain gauge if there is a change in capacitance as a function of strain of the films. In order to connect the strain gauge to the oscillator circuit, wire bonding technique is introduced to attach the copper line to the studied capacitor. The wire bonding machine is shown in Fig. 4.7.



Figure 4.4: (a) The home made DC sputtering machine

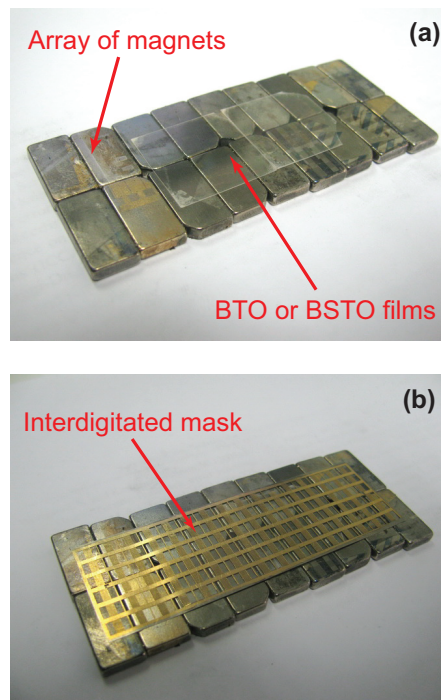


Figure 4.5: (a) Placing BTO or BSTO thin films on array of magnets (b) Attaching the interdigitated chrome mask with the magnet

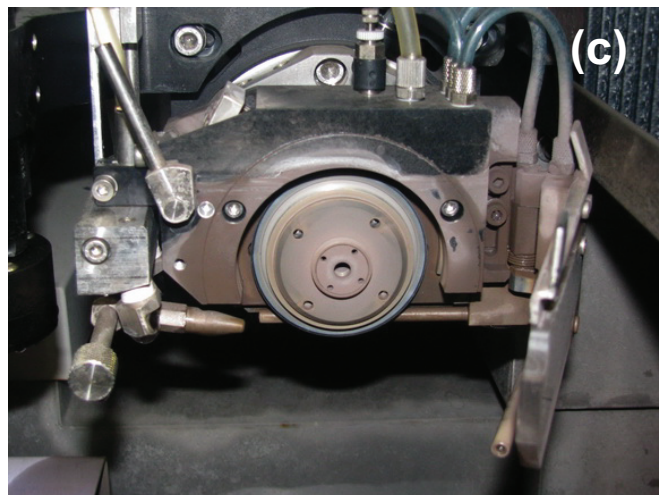


Figure 4.6: (a) The dicing saw machine (b) Inside the dicing saw machine (c) The diamond saw



Figure 4.7: The wire bonding machine (Model 4522)

4.3 Capacitance measurement

After obtaining individual coplanar capacitors, first I had to check whether each one is shorted or not using a multimeter and chose only the one that works. In order to measure the capacitance of a capacitor, it was mounted in the ring resonator as shown in Fig. 4.11. The ring resonator was made by Mark Dalberth [20] and Satreerat Hodak [30]. Silver paint was used to connect between electrodes of interdigitated capacitor and copper line pattern of ring resonator box. LF impedance analyzer or LCR meter (HP 4192) was used to measure capacitance (C) and dissipation factor (D) representing the loss (See Fig. 4.11). This LCR meter can measure electrical parameters as a function of frequency in the range of 5-13 MHz. Labview version 8.5 (See Fig. 4.12) was used as a visual instrument to run program via the front panel to the interfaced apparatus and the measured values were displayed in the front panel. The labview program of capacitance was written by Mr. Surakarn Thitinan [31]. In this program, the initial frequency and the final frequency including the frequency interval can be selected, and the unit

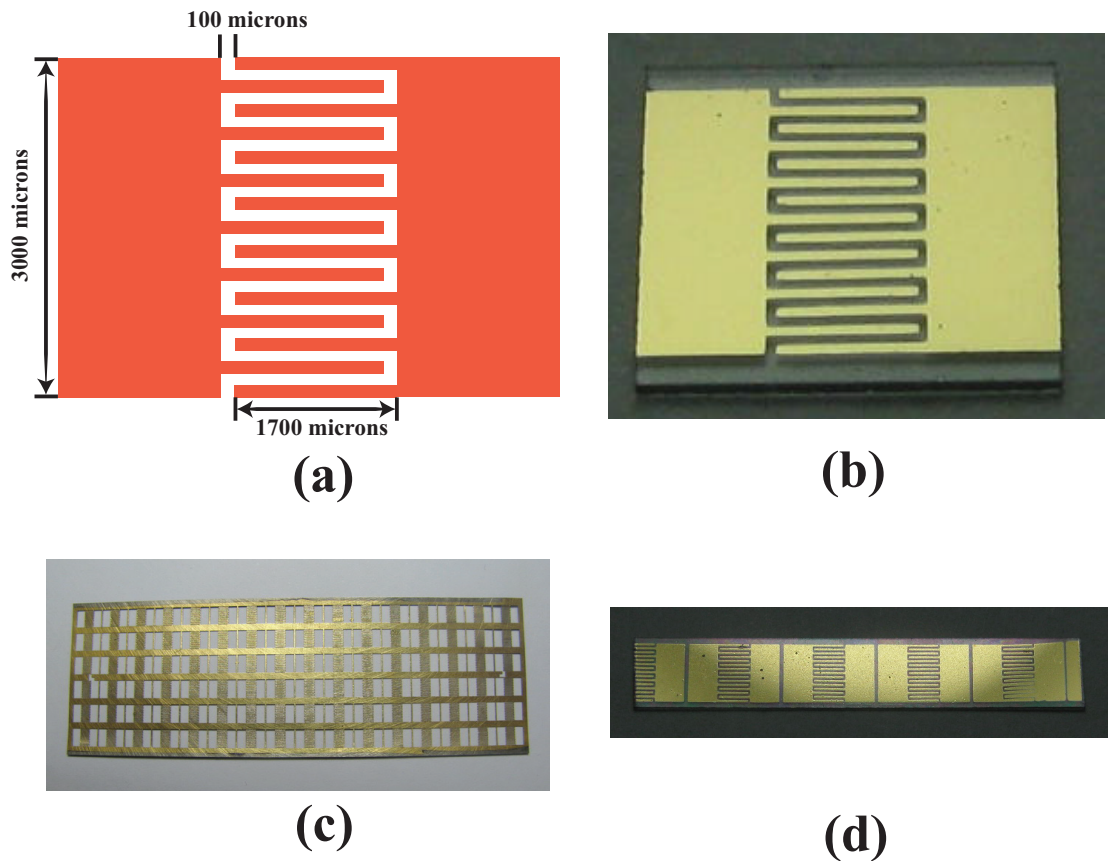


Figure 4.8: (a) The pattern of interdigitated mask (b) Coplanar capacitor (c) Interdigitated mask (d) An array of interdigitated capacitor in cantilever form

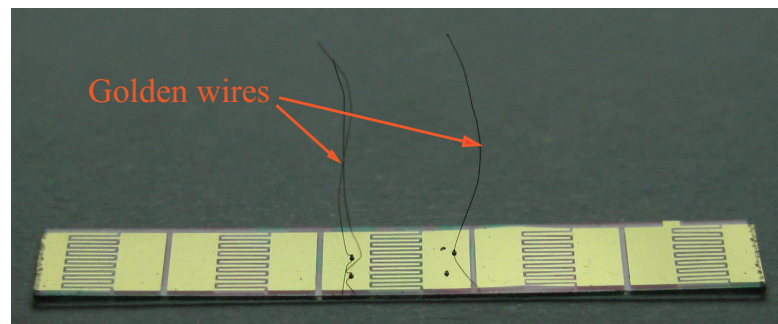


Figure 4.9: The strain gauge

has to be in kilohertz. Before clicking at the run button, the "set" button was needed to be pressed to reset the new input frequency values, From Fig. 4.12, the graph of the capacitance versus frequency is in the left panel and corresponding dissipation factor is in the right panel. The result of the measurement can be

obtained in .txt file.



Figure 4.10: The LCR meter

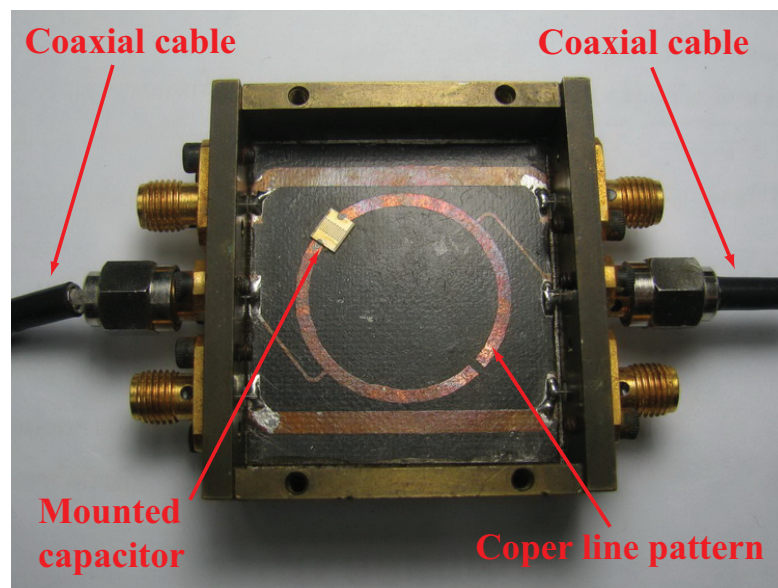


Figure 4.11: The ring resonator box

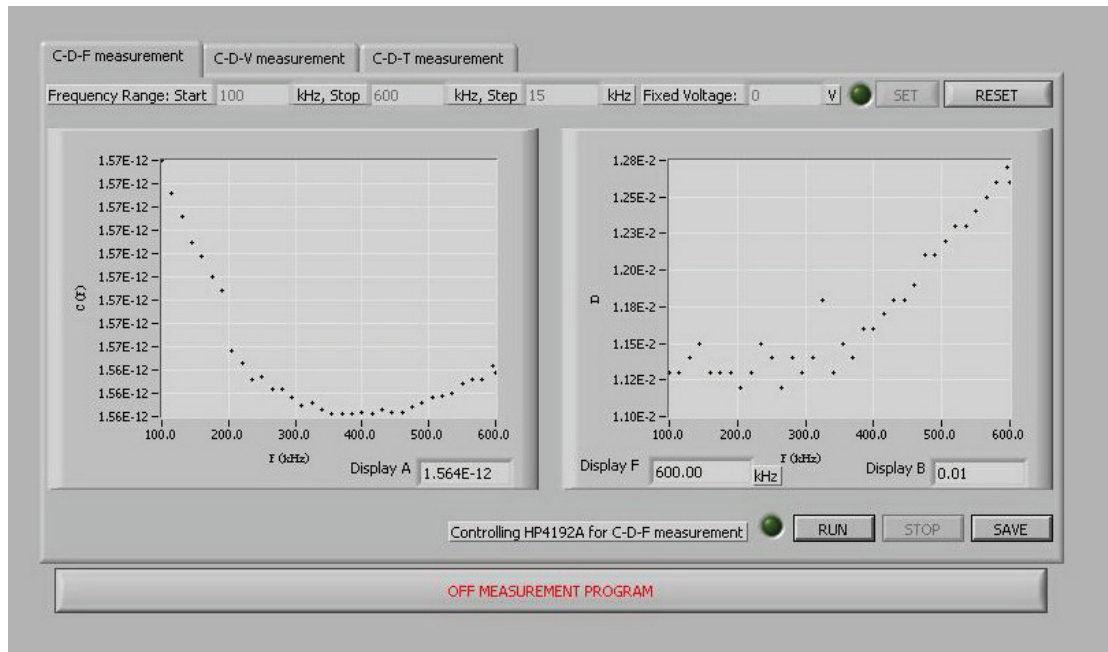


Figure 4.12: Labview program Version 8.5

4.4 Resonant frequency of an oscillator circuit as a function of stress and strain

As shown in Fig. 4.13, a parallelogram clamp of the fixture and a mechanically amplified piezoelectric actuator were used for supporting the cantilever under applying at the free end, and for the application of the stress and the strain in the film, respectively. The fixture is made of aluminum and is lifted up by attaching to four acrylic based with screws at the four corners of the fixture. The acrylic bases were machined using the lathe provided by the Department of Physics, Chulalongkorn University. As shown in Fig. 4.13 and 4.14 (b), the clamping point was used to hold the cantilever by turning at screw knob. The free end of the cantilever beam was near an adjustable contact line that applied a force with the piezoelectric ceramic as an actuator.

The gold electrodes of the capacitor were connected via gold wire bonding before mounting it at the clamping point in the fixture. Then, two ends of golden wires were connected to the oscillator circuit by soldering iron technique at A

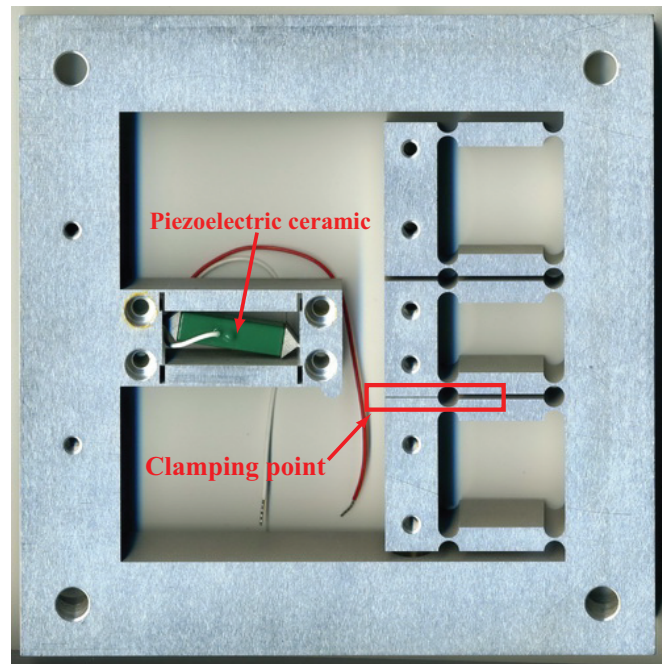
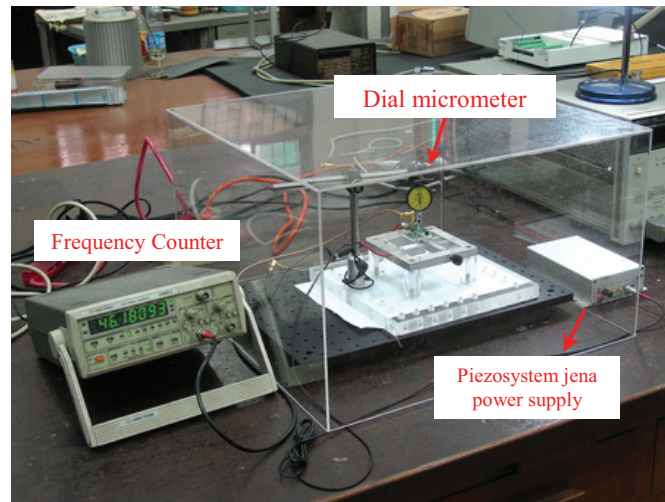


Figure 4.13: The strain gauge fixture

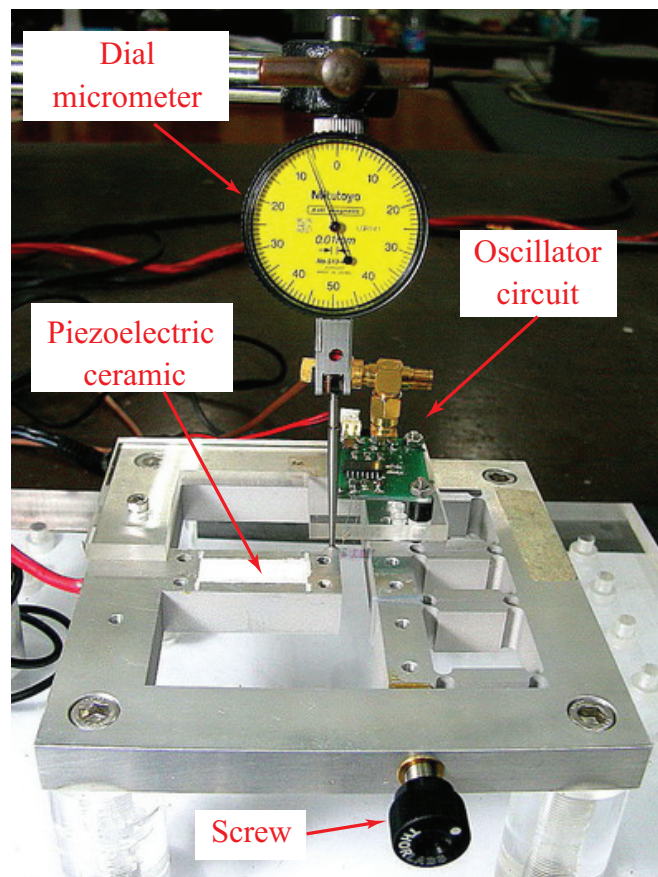
position in the circuit diagram (See detail of oscillator circuit Appendix A). The output signals from oscillator circuit were transferred via SMA connectors with coaxial cables. The corresponding resonant frequency as a function of deflection distance was measured by HUA Chang universal counter (U2000A). The deflection distance at one point of the cantilever was measured by Mitutoyo dial micrometer. We tried to put the micrometer near the free end as much as possible. As I mentioned before, the piezoelectric ceramic acting as an actuator was used to apply the force to the end of the film on glass cantilever. We controlled the deflection distance of the cantilever by adjusting the voltage. The adjusted voltage was in the range 0-12 V but was amplified ten times to DC bias voltage in the 0-120 V range before applying to the piezoelectric ceramic. The expansion of the piezoelectric ceramic in the fixture generated the force on the free end of the clamped strain gauge. The simulation between deflection and force at any positions on the strain gauge is shown in Fig. 2.15 (See section 2.3.7) which are related to the deflection from each force level on the strain gauge measured by a dial micrometer. The simulation of stress on the strain gauge at any positions are

shown in Fig. 2.16 and the deflection at two interesting positions ($x=0.5$ cm and $x=0.7$ cm) of capacitor on the strain gauge.

The simulation of stain on the strain gauge at any positions are Fig. 2.17. The stress and strain can be calculated from the deflection using equation 2.31 and 2.33. The fixture and acrylic base are setup on non-vibration base covered with acrylic box for preventing the air flow during the experiment. The experimental setup are shown in Fig. 4.14(a) and Fig. 4.14(b).



(a)



(b)

Figure 4.14: (a) The overall experimental setup (b) The fixture with piezo actuator and dial micrometer

CHAPTER V

RESULTS AND DISCUSSION

In this chapter, the result and discussion concerning the crystal structure, the chemical compositions, the dielectric responses, the stress and the strain sensing of the films are shown. First, in section 5.1, I will show the results of the effect of the annealing temperature and annealing time and the crystal structure observed in X-ray diffraction (XRD) patterns of the studied films and the deformation of the borosilicate glass substrate. In section 5.2, the stoichiometry of both types of films (BaTiO_3 :BTO and $\text{Ba}_x\text{Sr}_{1-x}\text{TiO}_3$) were obtained from wavelength dispersive X-ray spectrometry technique. In section 5.4, the dielectric constant and the corresponding dielectric loss as a function of frequency of the BTO and BSTO films are presented and compared. Finally, in section 5.5 the stress and strain sensing results of the BTO film capacitor connected to the oscillating circuit are shown.

5.1 The effect of annealing temperature and annealing time on the crystal structure and the deformation of the borosilicate substrate

In many film growth techniques, pulsed laser deposition (PLD), chemical vapor deposition (CVD) and Sol-gel etc., various growth parameter such as annealing temperature and annealing time are concerned. In this thesis work, a sol-gel technique was used to prepare BTO and BSTO films. In this technique,

one of the important film growth parameters affecting on the film crystallinity are the annealing temperature and annealing time. In the work of Thidarat Supasai et al. [32], since they chose the ITO glass substrate for supporting BTO/STO multilayer films, the annealing temperature was limited to 650°C due to the possible melting of the substrate that could happen at higher temperatures. Ornicha Kongwut et al. [33] used quartz as a substrate which has higher melting point (about 1600°C) for BTO film preparation at 800°C . Thidarat Supasai and Ornicha Kongwut are graduate students in our group. Their results showed that the BTO film on quartz substrate had better crystallinity indicated by the sharper peaks in XRD pattern. The peak intensities of BTO films on quartz substrates were also higher than those of BTO/STO multilayer films obtained from Thidarat Supasai et al.

At first, we have to concern the type of substrate used in this thesis before choosing the annealing temperature and annealing time. Because we have to fabricate the capacitive strain gauge from BTO or BSTO films so the thin borosilicate glass substrates are suitable for this thesis work due to the owning of the flexibility and having higher melting temperature than those of thin cover glass slides. Furthermore, for the cost issue borosilicate glass substrates are cheaper than thin quartz substrates.

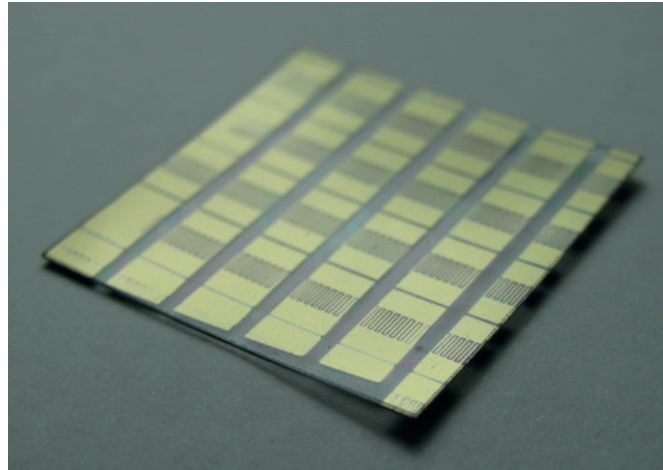


Figure 5.1: The deformed borosilicate glass substrate with gold electrode patterned on the BSTO film (BSTO#5) with 7 layers annealed at 650°C of 1.5 hr for each layer

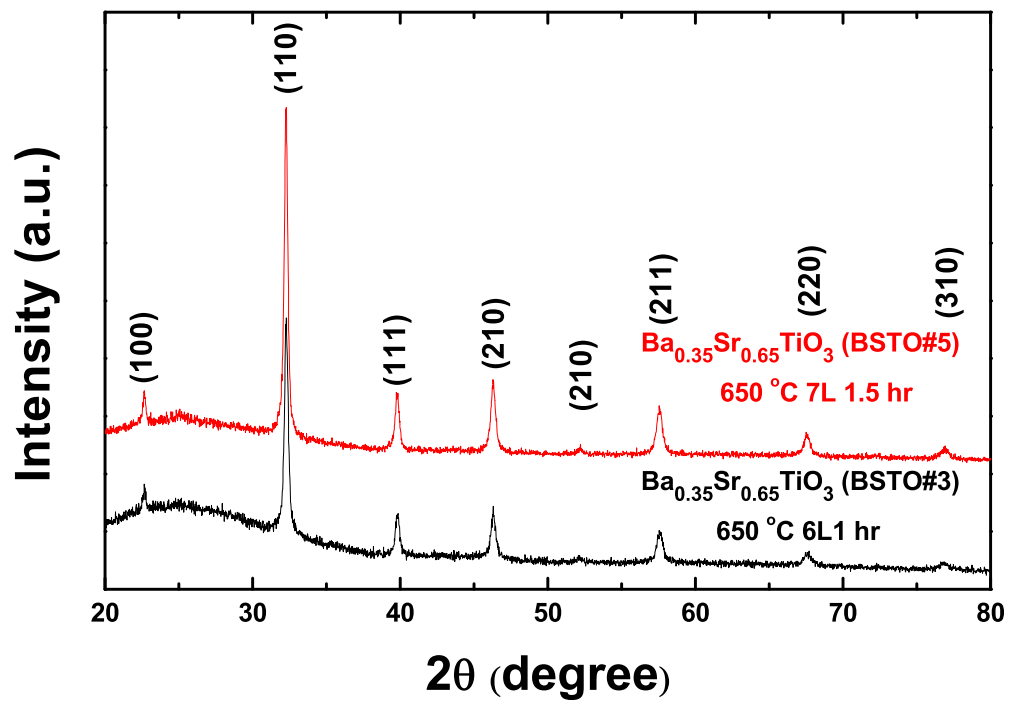


Figure 5.2: XRD patterns of BSTO#3 and BSTO#5 ($\text{Ba}_{0.35}\text{Sr}_{0.65}\text{TiO}_3$)

This bending problem of the substrate affects dicing process in our experiment. But the XRD pattern of this film (BSTO#5) annealed at 650°C with total time annealing of 10.5 hr show that the film has very good crystallinity because diffracted peaks are sharp and the intensities are very high as shown in Fig. 5.2. Thus, we have to reduce the annealing time for each layer from 1.5 hr to 1 hr to avoid the bending problem and melting problem. And the melting problem can be avoid by keeping the annealing temperature no more than 650°C . From our film preparation process only for BTO films, we found that no crystallinity in the film occurs for 1 hr annealing time (See Fig. 5.3). Thus, we had to repeat annealing process for another 2 hr after six layers are completed to ensure the crystallinity of thin films (See Fig. 5.4).

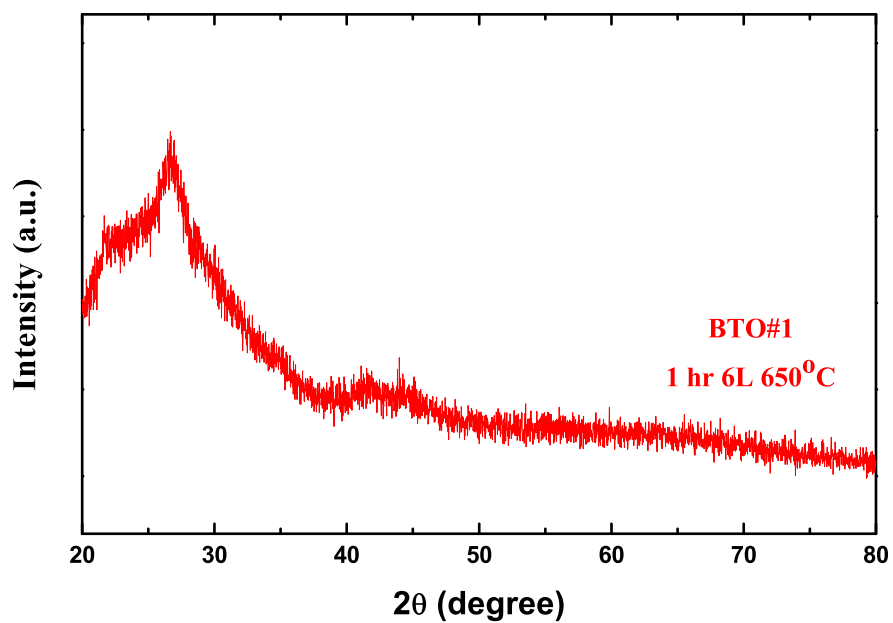


Figure 5.3: XRD pattern of BTO#1 (6 layers) thin film annealed for 1 hr for each layer

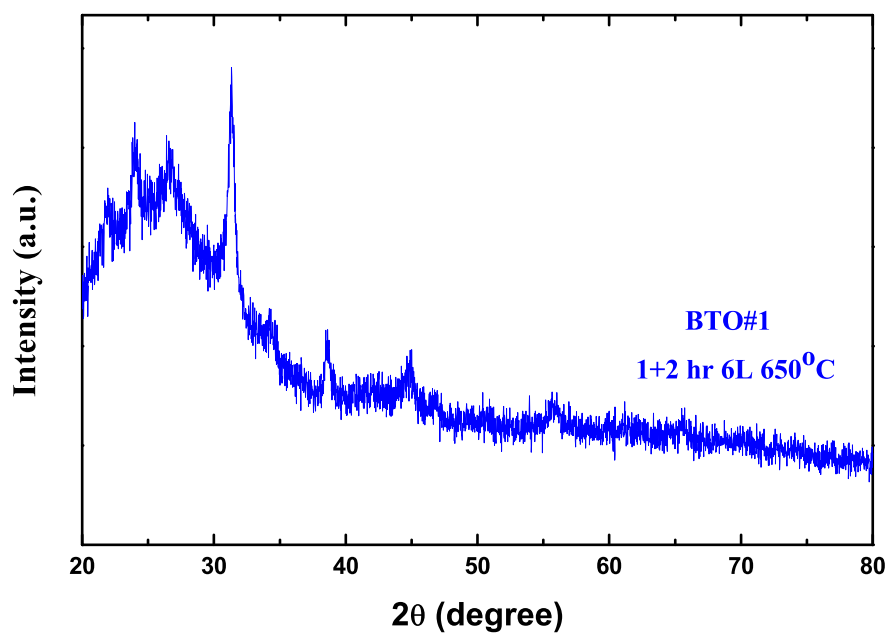


Figure 5.4: XRD pattern of BTO#1 (6 layers) thin film after increasing annealing time for 2 hr

5.2 The WDS result of barium strontium titanate

The compositions of our thin films were obtained using wavelength dispersive X-ray spectrometer (WDS) equipped with electron probe microscope. We probed electron beams on three different spots of the BSTO films and the atomic percentage of each element was averaged as shown in Table 5.1, 5.2 and 5.3. The stoichiometric $\text{Ba}_{0.69}\text{Sr}_{0.31}\text{TiO}_3$, $\text{Ba}_{0.8}\text{Sr}_{0.2}\text{TiO}_3$, and $\text{Ba}_{0.35}\text{Sr}_{0.65}\text{TiO}_3$ films are determined. The growth conditions of film preparation with different Ba and Sr contents were shown in Table 4.1 and 4.2.

Table 5.1: WDX result of $\text{Ba}_{0.69}\text{Sr}_{0.31}\text{TiO}_3$ thin film

Element	Percent of atom
Sr	18.1036
Ba	40.2843
Ti	41.6121
Total	100.00

Table 5.2: WDX result of $\text{Ba}_{0.8}\text{Sr}_{0.2}\text{TiO}_3$ thin film

Element	Percent of atom
Sr	16.816
Ba	59.101
Ti	24.083
Total	100.00

Table 5.3: WDX result of $\text{Ba}_{0.35}\text{Sr}_{0.65}\text{TiO}_3$ thin film

Element	Percent of atom
Sr	19.829
Ba	69.463
Ti	10.709
Total	100.00

5.3 X-ray diffraction pattern

5.3.1 X-ray diffraction pattern of BaTiO_3 , $\text{Ba}_{0.35}\text{Sr}_{0.65}\text{TiO}_3$ and $\text{Ba}_{0.8}\text{Sr}_{0.2}\text{TiO}_3$ thin films

The X-rays diffraction (XRD) patterns of the BTO and BSTO films on borosilicated glass substrates annealed at 650°C are shown in Fig. 5.5. At this temperature, the films were formed polycrystalline. The lattice constant are calculated from (101) and (200) peak positions showing that the lattice constant of the $\text{Ba}_x\text{Sr}_{1-x}\text{TiO}_3$ films are smaller than that of pure BaTiO_3 as can be seen from the shift to higher diffraction angles. At room temperature, STO is cubic ($a = b = c$) with the lattice constant of 3.905\AA (See appendix B) and BTO is tetragonal ($a = b \neq c$) with $a = b = 3.994\text{\AA}$ and $c = 4.038\text{\AA}$ (See appendix B). From XRD diffraction pattern and XRD database (See Appendix B), BaTiO_3 and $\text{Ba}_{0.8}\text{Sr}_{0.2}\text{TiO}_3$ are found to be in tetragonal phase. $\text{Ba}_{0.35}\text{Sr}_{0.65}\text{TiO}_3$ has cubic phase as SrTiO_3 because of more strontium content than barium content.

The lattice constant values of BaTiO_3 and $\text{Ba}_{0.8}\text{Sr}_{0.2}\text{TiO}_3$ are calculated from (101) and (200) peaks positions showing that the lattice constant (a and b) are 4.05\AA and 4.00\AA , respectively. For $\text{Ba}_{0.35}\text{Sr}_{0.65}\text{TiO}_3$, the lattice constant is calculated from (100) and (200) peak positions showing that the lattice constant (a,b and c) is 3.92\AA . These lattice constants of BTO and BSTO decrease while adding more strontium content. Because the atomic radius of strontium atom is smaller than that of barium atom, by the substitution of Sr (radius size 2.15\AA) to Ba (radius size 2.22\AA) sites causes the reduction in the lattice constant.

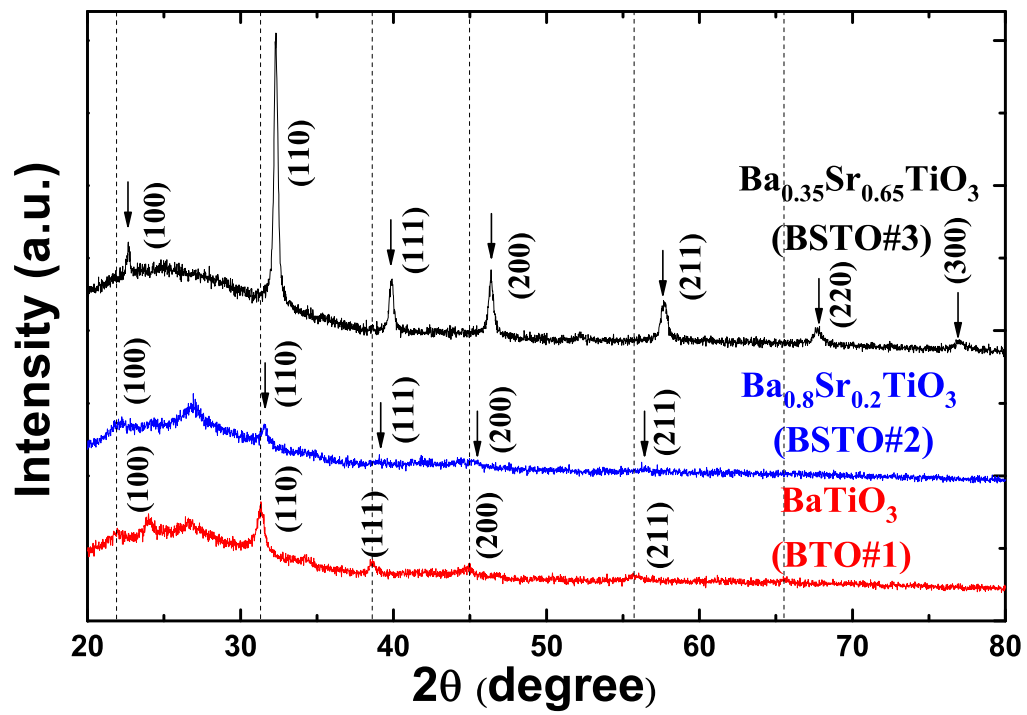


Figure 5.5: XRD pattern of BaTiO_3 , $\text{Ba}_{0.8}\text{Sr}_{0.2}\text{TiO}_3$ and $\text{Ba}_{0.35}\text{Sr}_{0.65}\text{TiO}_3$

5.4 Dielectric response of the film

5.4.1 Dielectric constant and dielectric loss versus frequency of BaTiO₃ thin film

The resulting dielectric constant, capacitance and dielectric loss as a function of frequency of the BTO films is shown in Fig. 5.6. This figure shows that the capacitance of the BTO film decrease as a function of frequency in the range 100-1100 kHz. The maximum capacitance of BTO film is found to be 1.0 pF (See Fig. 5.6(a)). The maximum dielectric constants versus frequency in Fig. 5.6(b) calculated capacitance conversion (See subsection 2.4.3) is 309 at 100 kHz of frequency. In comparison with Xu, R. [14], the dielectric constant of BTO films increases with increasing in the crystallinity of the film. Xu, R. [14] annealed the BTO film at 750°C on Pt/Ti/SiO₂ substrate and found that the dielectric constant is in the range of 250-348 in the 100-1000 kHz frequency wavelength range.

5.4.2 Dielectric constant and dielectric loss versus frequency of Ba_{0.8}Sr_{0.2}TiO₃ thin film

For Ba_{0.8}Sr_{0.2}TiO₃ film, the result of dielectric constant, capacitance and dielectric loss are obtain from LCR meter in the function of frequency (See Fig. 5.7). Figure 5.7(a) shows that capacitance of the film decrease in the frequency range 40 - 440 kHz. The maximum capacitance of Ba_{0.8}Sr_{0.2}TiO₃ film is found to be 1.1 pF. From Fig. 5.7(c), the maximum dielectric constant from capacitance conversion (See subsection 2.4.3) is 418 at 40 kHz.

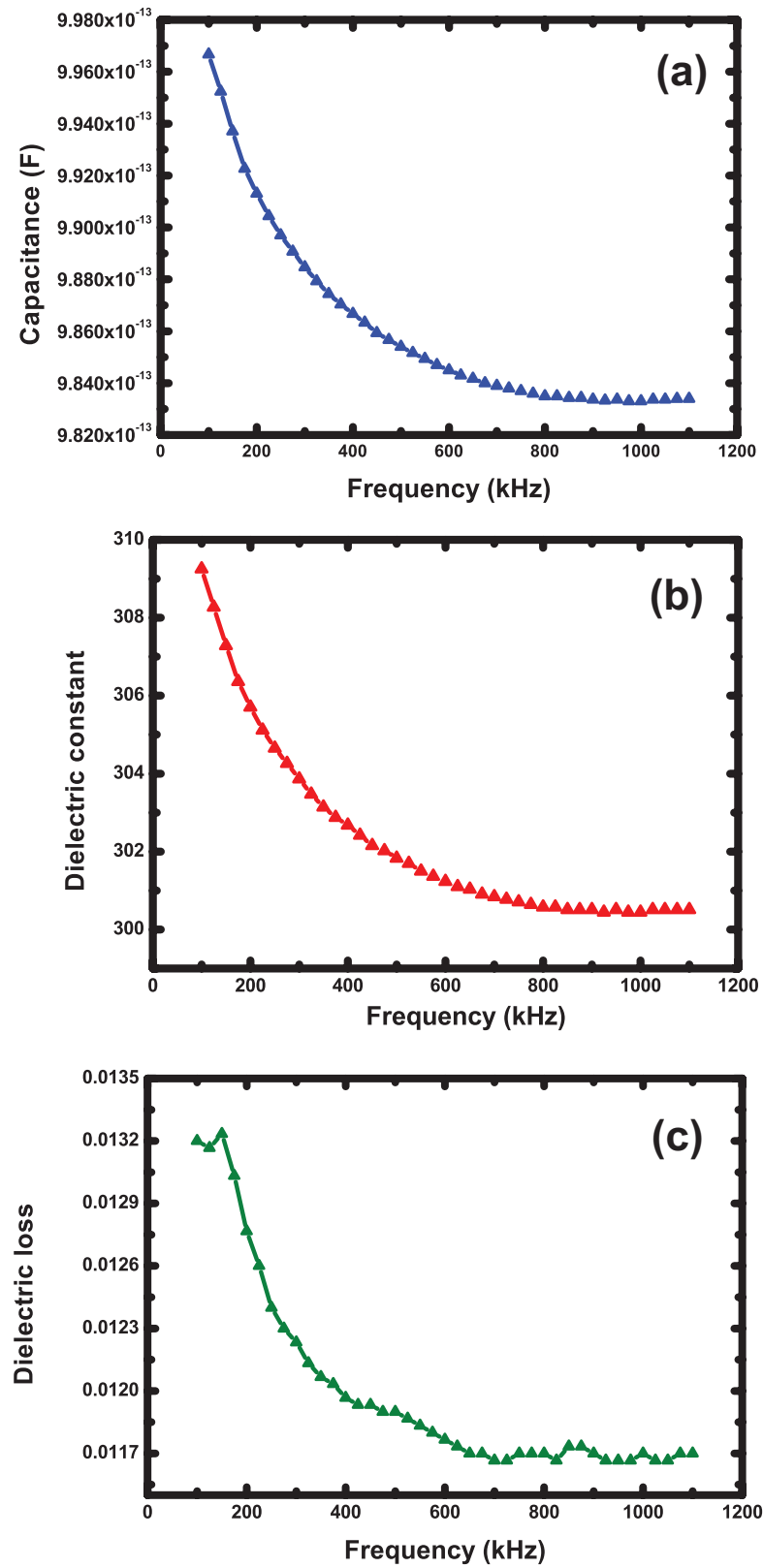


Figure 5.6: (a) Capacitance of BaTiO₃ thin film (b) Dielectric constant of BaTiO₃ thin film (c) Dielectric loss of BaTiO₃ thin film

5.4.3 Dielectric constant and dielectric loss versus frequency of $\text{Ba}_{0.65}\text{Sr}_{0.35}\text{TiO}_3$ thin film

For $\text{Ba}_{0.65}\text{Sr}_{0.35}\text{TiO}_3$ film, the result of dielectric constant, capacitance and dielectric loss are obtained from LCR meter in the function of frequency (See Fig. 5.8). Figure 5.8(a) shows that capacitance of the film decreases in the frequency range 100 - 600 kHz. The maximum capacitance of $\text{Ba}_{0.65}\text{Sr}_{0.35}\text{TiO}_3$ film is found to be 1.16 pF. From Fig. 5.8(a), the maximum dielectric constant from capacitance conversion (See subsection 2.4.3) is 482 at 100 kHz. Normally, the associated dielectric loss decreases with the dielectric constant in which we observed in our films as well. We found that by adding more strontium contents to the BTO film can increase the capacitance e.g. the dielectric constant. The dielectric constant and corresponding dielectric loss increase due to the strain effect in the film. Similar results have been observed by others [14, 23].

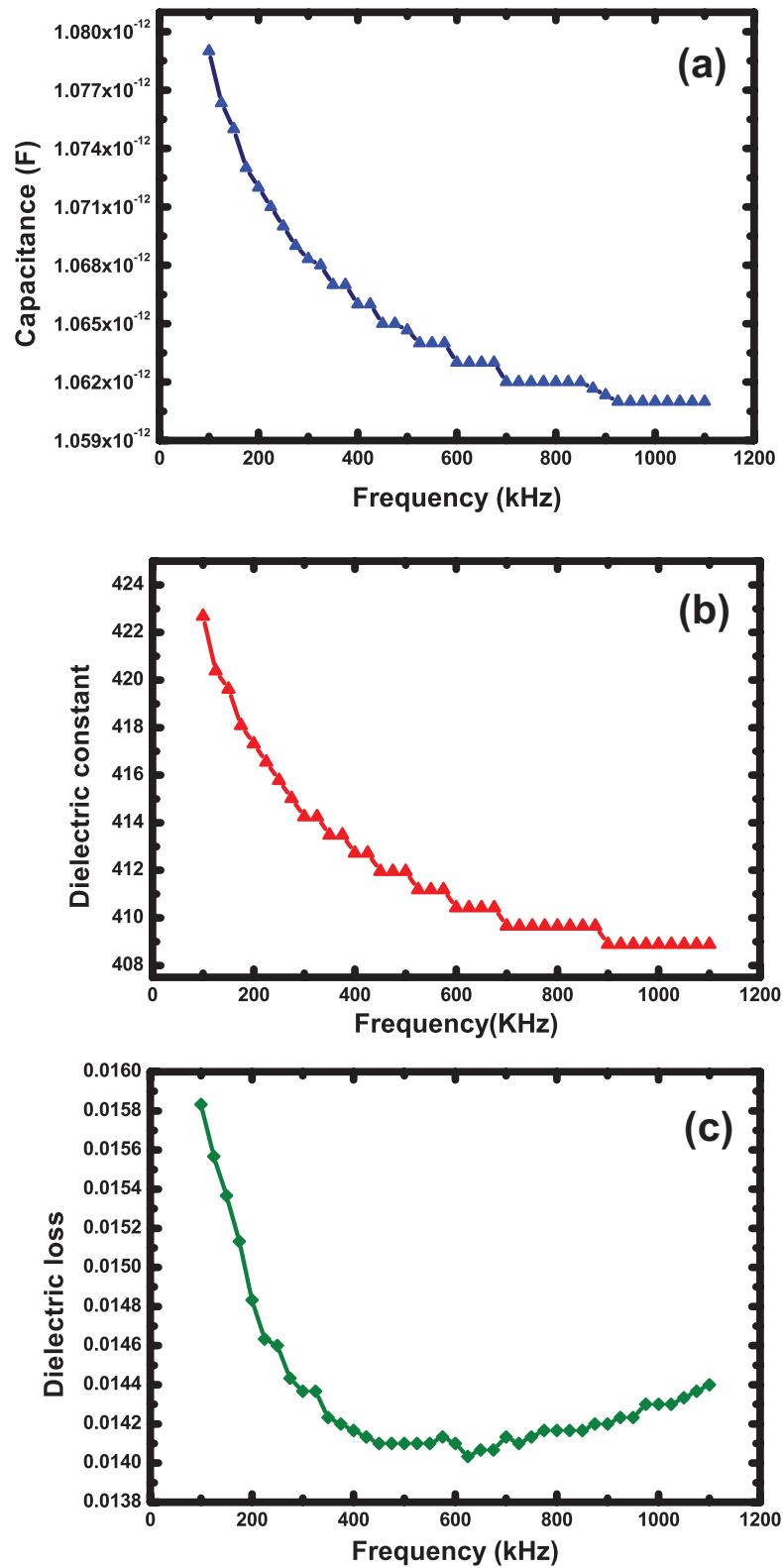


Figure 5.7: (a) Capacitance of $\text{Ba}_{0.8}\text{Sr}_{0.2}\text{TiO}_3$ thin film (b) Dielectric constant of $\text{Ba}_{0.8}\text{Sr}_{0.2}\text{TiO}_3$ thin film (c) Dielectric loss of $\text{Ba}_{0.8}\text{Sr}_{0.2}\text{TiO}_3$ thin film

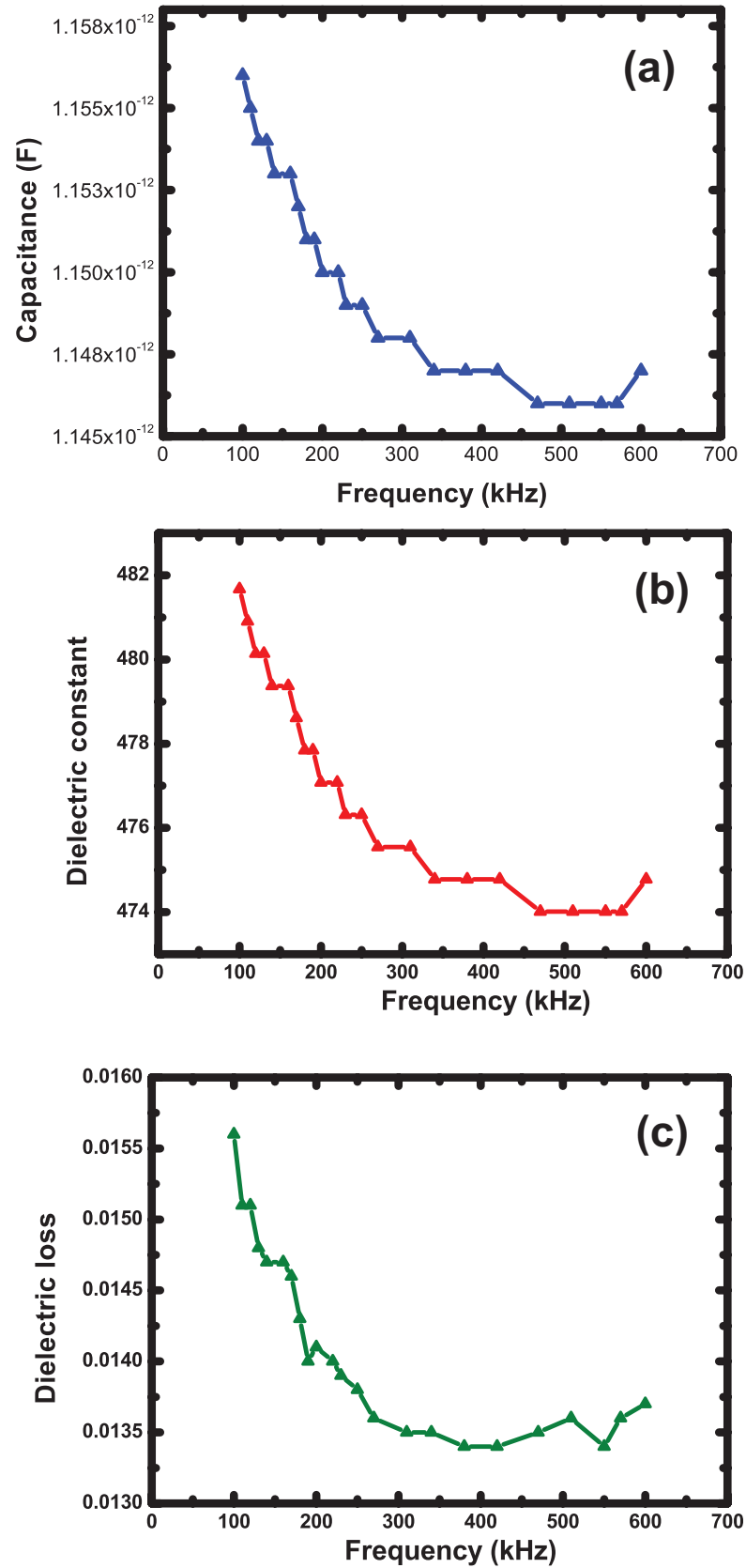


Figure 5.8: (a) Capacitance of $\text{Ba}_{0.35}\text{Sr}_{0.65}\text{TiO}_3$ thin film (b) Dielectric constant of $\text{Ba}_{0.35}\text{Sr}_{0.65}\text{TiO}_3$ thin film (c) Dielectric loss of $\text{Ba}_{0.35}\text{Sr}_{0.65}\text{TiO}_3$ thin film

5.5 Stress and strain sensing of barium titanate thin film

5.5.1 Stress and strain sensing of the cantilever made of barium titanate thin film at $x = 0.7$ cm.

After BTO strain gauge is clamp with the fixture (See section 4.4), we used the vernier to measure some parameter which showed in Table 2.1 such as the range from the clamping point to applying force position (a), the position of interesting capacitor (b) then we start to apply the force using piezoelectric actuator attached with dial micrometer touching with the one end of strain gauge (See Fig. 4.14). We observe and collect some a frequency value form each step of applying force to the device which is equal to 0.01 mm of the strain gauge deflection range. From our experiment, the piezoelectric ceramic can be round in voltage by 11 step. Before collecting each frequency value from an oscillator circuit, we have to wait until the number on frequency counter is stable for 30 seconds. In order to ensure the correction of our data we have to repeat the 11 measuring step process again for 5 times but during each time of measurement we have to wait unit the film is relax from stress and strain, this waiting time is called the relaxation time of BTO film which is equal to 30 minutes. The data from our BTO stress and strain sensing is show in the 4 graph stress versus frequency and strain versus frequency (See Fig. 5.9, 5.10, 5.11 and 5.12) where two graphs of stress and strain is plotted together with the deflection at 0.7 cm and the deflection at the end point.

From Fig. 5.9, the resonant frequency from interesting capacitor on the strain gauge and stress at 0.7 cm decrease together while deflection distance at capacitance position is increased as a function of applying force from piezoelectric actuator. The deflection 0.7 cm of interdigitated capacitor on the BTO strain gauge can be calculated from simulation program (See subsection 2.3.4). From Fig. 2.15, simulation result of deflection and stress of borosilicate cantilever (See. 5.9), the deflection distance at capacitor position increase from 3.0×10^{-5} m to

1.1×10^{-4} m. The resonant frequency from an oscillator circuit decrease in the range between 46.06 MHz and 45.96 MHz. The stress of the strain gauge at the capacitor position increase from 2.36×10^6 to 8.65×10^6 Pascal. From Fig. 5.10, the resonant frequency decrease while the deflection at the end point increase. From the simulation result (See Fig. 2.15), the minimum and maximum deflection perform at clamping point and the end point, respectively. The deflection range at end point is in the range between 5.18×10^{-5} m and 1.90×10^{-4} m. The relation between strain and resonant frequency from Fig 5.11 and 5.12 show that at 0.7 cm clamping point, strain increase as a function of frequency indicated by eleven levels of deflection range from 3.74×10^{-5} to 1.37×10^{-4} (See Fig. 5.11). From 5.11 and 5.12, the resonant frequency from interesting capacitance is increasing. The deflection range at 0.7 cm and the free end position is the same with Fig. 5.9 and 5.10.

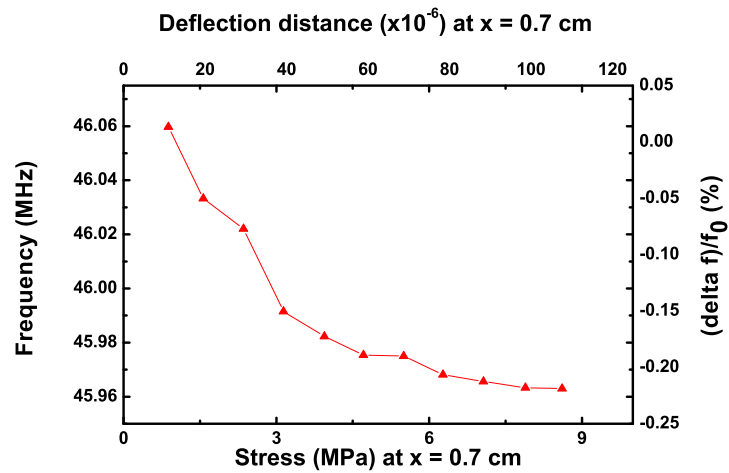


Figure 5.9: Variation of the resonant frequency and the change in resonant frequency of the oscillator with applied deflection at the free end whereas the bottom axis shows the corresponding stress at the location of the capacitor (at $x = 0.7$ cm) and the top axis show the deflection at $x = 0.7$ cm

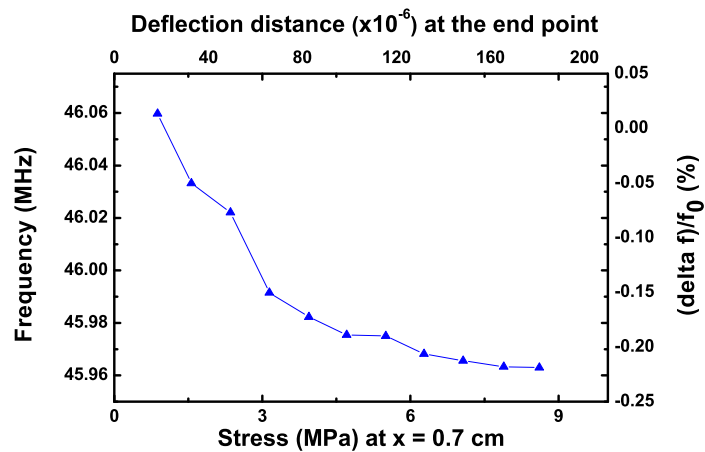


Figure 5.10: Variation of the resonant frequency and the change in resonant frequency of the oscillator with applied deflection at the free end whereas the bottom axis shows the corresponding stress at the location of the capacitor (at $x = 0.7$ cm) and the top axis show the deflection at the end point

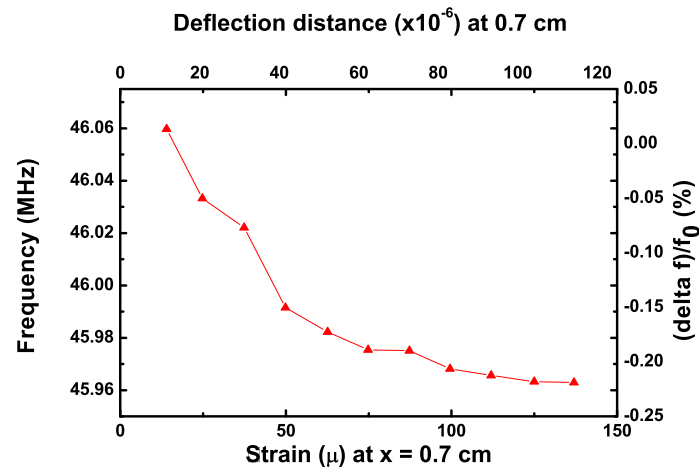


Figure 5.11: Variation of the resonant frequency and the change in resonant frequency of the oscillator with applied deflection at the free end whereas the bottom axis shows the corresponding strain at the location of the capacitor (at $x = 0.7$ cm) and the top axis show the deflection at 0.7 cm

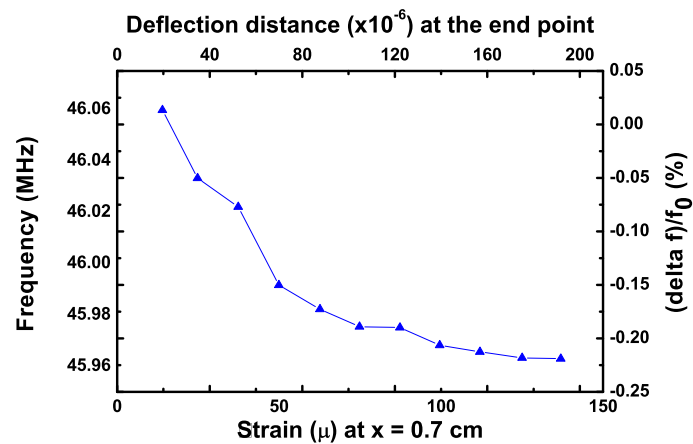


Figure 5.12: Variation of the resonant frequency and the change in resonant frequency of the oscillator with applied deflection at the free end whereas the bottom axis shows the corresponding strain at the location of the capacitor (at $x = 0.7$ cm) and the top axis show the deflection at the end point

5.5.2 Stress and strain sensing sensing of the cantilever made of barium titanate thin film at $x = 0.5$ cm.

In order to change the interesting capacitance position, we unscrew the knob (See Fig. 4.14) and move the interesting capacitance to 0.5 cm position carefully because the gold wire fragile. After that, we repeat all the process as subsection 5.5.1. We increase the time between each point of the resonant frequency measurement up to 1 minute for ensure the stability of the frequency value.

From stress and strain simulation result at 0.5 cm, (See Fig. 2.16 and 2.17) 0.5 cm of capacitance position increase while the resonant frequency and deflection at 0.5 cm and the end point position decrease. The resonant frequency perform between 45.532 MHz and 45.462 MHz (See Fig. 5.13, 5.14, 5.15 and 5.16). The stress and strain value increase from 7.62×10^6 to 7.59×10^7 Pascal and 2.23×10^{-5} to 2.28×10^{-4} , respectively. The deflection distance at 0.5 cm of capacitor position increase from 3.33×10^{-5} to 3.31×10^{-4} m while the deflection at the free end is remain in the same range.

If we were to measure the stress and strain sensing result of the BSTO films, we expected to see the measured resonant frequency decreased due to the higher capacitance values of the BSTO films (See Fig. 5.7 and 5.8) according to $f_{resonant} = \frac{1}{R_7 C_4}$. (See detail in Appendix A) The increase in capacitance values of BSTO films are due to the internal strain in the film [23].

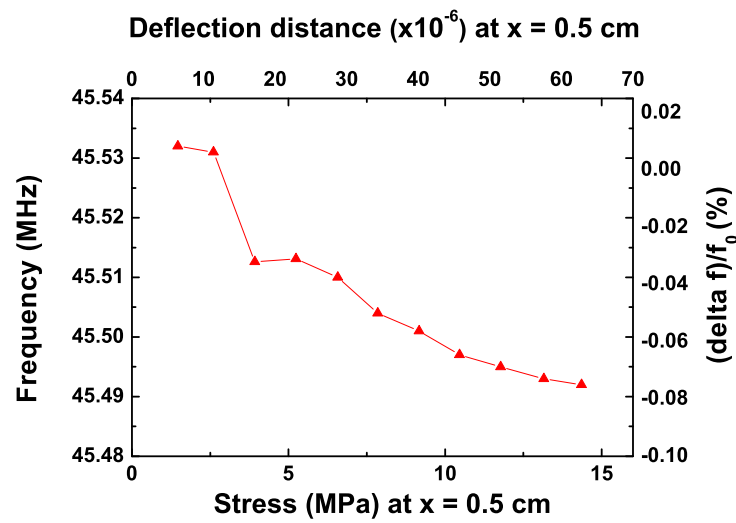


Figure 5.13: Variation of the resonant frequency and the change in resonant frequency of the oscillator with applied deflection at the free end whereas the bottom axis shows the corresponding stress at the location of the capacitor (at $x = 0.5$ cm) and the top axis show the deflection at $x = 0.5$ cm

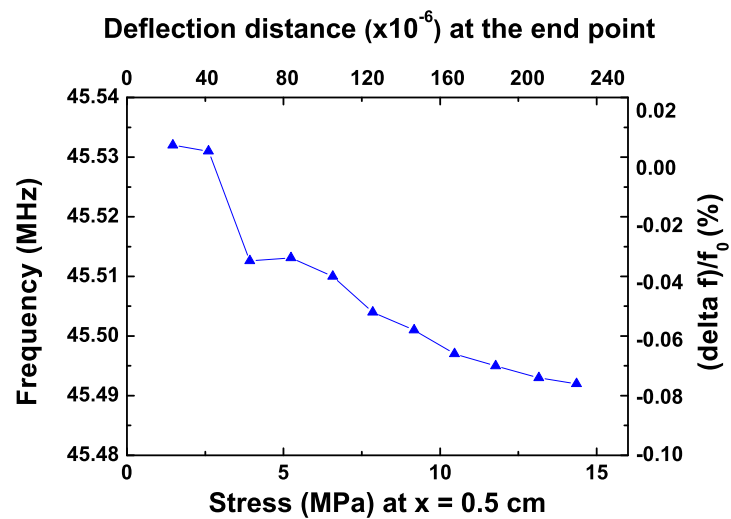


Figure 5.14: Variation of the resonant frequency and the change in resonant frequency of the oscillator with applied deflection at the free end whereas the bottom axis shows the corresponding stress at the location of the capacitor (at $x = 0.5$ cm) and the top axis show the deflection at the end point

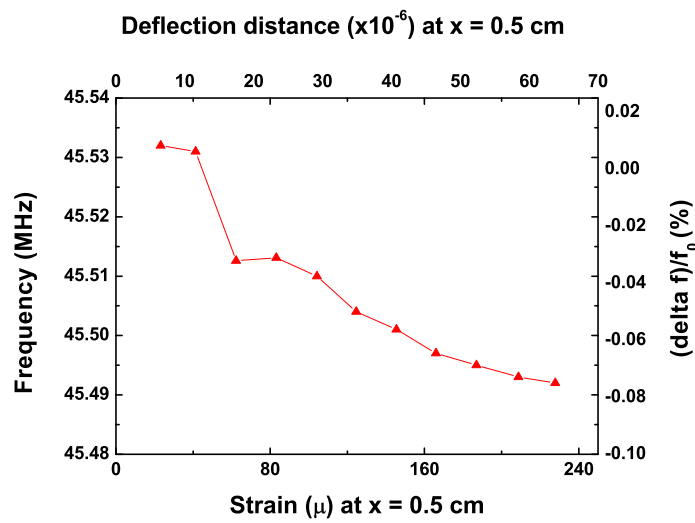


Figure 5.15: Variation of the resonant frequency and the change in resonant frequency of the oscillator with applied deflection at the free end whereas the bottom axis shows the corresponding strain at the location of the capacitor (at $x = 0.5$ cm) and the top axis show the deflection at 0.5 cm

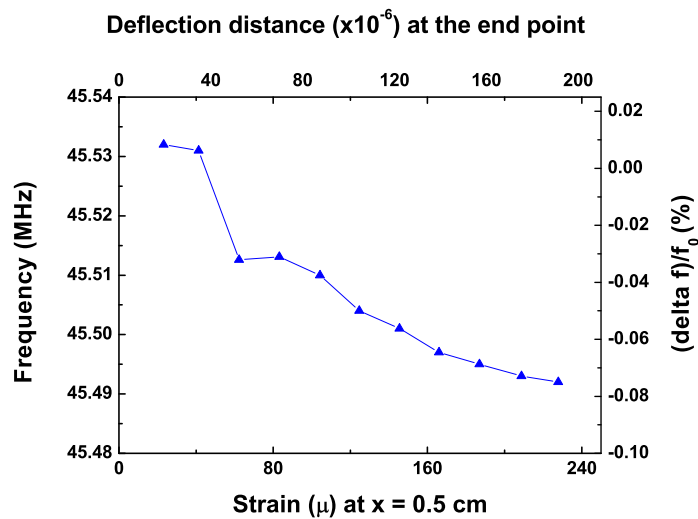


Figure 5.16: Variation of the resonant frequency and the change in resonant frequency of the oscillator with applied deflection at the free end whereas the bottom axis shows the corresponding strain at the location of the capacitor (at $x = 0.5$ cm) and the top axis show the deflection at the end point

CHAPTER VI

CONCLUSIONS

In this thesis, we prepared barium titanate (BaTiO_3) and barium strontium titanate ($\text{Ba}_x\text{Sr}_{1-x}\text{TiO}_3$) thin film with various conditions of Ba/Sr contents by a sol-gel spin technique. Some characteristic properties of these films such as lattice constant, stoichiometry, dielectric constant were obtained. After that, we constructed the strain gauges with capacitor using barium strontium titanate thin film dielectrics.

In the annealing process, two variables to be considered in the preparation of thin films are annealing time and annealing temperature. Our films exhibited more crystallinity if the annealing temperature and time are increased because all atoms received more energy from annealing process. Although the crystallinity is better but the bending effect of the substrate make it difficult to dice to strain gauges or individual capacitors. Thus, we conclude that the best condition for preparing BTO and BSTO films for construction of strain gauges is 650°C with 1 hour of annealing time for each layer. The stoichiometric results show 3 types of $\text{Ba}_x\text{Sr}_{1-x}\text{TiO}_3$ ($x = 0.8$, $x = 0.69$ and $x = 0.35$) which have the different Ba/Sr contents.

The XRD patterns of 3 types of the films shows us that adding Sr content make $\text{Ba}_x\text{Sr}_{1-x}\text{TiO}_3$ decrease lattice constants. XRD peak positions shifted to the higher diffracted angle also make our films have better crystallinity (See Fig. 5.5).

The capacitance and dielectric loss of BaTiO_3 , $\text{Ba}_{0.8}\text{Sr}_{0.2}\text{TiO}_3$, $\text{Ba}_{0.69}\text{Sr}_{0.31}\text{TiO}_3$ and $\text{Ba}_{0.35}\text{Sr}_{0.65}\text{TiO}_3$ decrease as a function of frequency. The dielectric constants of BSTO films are larger than BTO film. This could be due to strain induced

in the BSTO films. The maximum dielectric constant of $\text{Ba}_x\text{Sr}_{1-x}\text{TiO}_3$ increase with Sr content (See Fig. 5.6 and 5.7) and our results agree with those of Bunting Shelton and Creamer's group [34]. They found that $\text{Ba}_x\text{Sr}_{1-x}\text{TiO}_3$ perform a maximum dielectric constant around $x = 0.75 - 0.85$.

The stress and strain sensing experiment results show that the resonant frequency from an oscillator circuit using interdigitated capacitor on BTO strain gauge decrease while deflection of strain gauge is increased with applying force from piezoelectric actuator (See Fig. 2.15 and 2.16). The change in the resonant frequency in our experiment is due to change in capacitance of BTO coplanar capacitor located at $x = 0.5$ cm and $x = 0.7$ cm on the strain gauge. The resonant frequency decreases while the stress and strain at capacitor position is increasing as we move x-position closer to the clamping point. The change in capacitance or dielectric constant of BTO as a function of stress and strain is from being piezoelectricity of this dielectric material. Due to the commercial capacitive sensor is quite expensive so our thesis showed that our BTO strain gauge can be used as a low cost capacitive strain gauge device.

References

- [1] Cullity, B.D. *Element of X-ray diffraction*. Addison-westley publishing Company,inc. 1959.
- [2] Tudor, M.J. and Beeby, S.P. Stress and modelling of microstructures. *Sensors and Materials* 1 (1997): 9.
- [3] Jaffe, B., Cook, W.R. and Jaffe, H. *Piezoelectric Ceramics*. Academic Press London,inc. 1971.
- [4] Dong, W., Lu, X., Cui, Y., Wang, J. and Liu, M. Fabrication and characterization of microcantilever integrated with PZT thin film sensor and actuator. *Thin Solid Films* 515 (2007): 8544–8548.
- [5] Lines, M.E. and Glass, A.M. *Principles and applications of Ferroelectrics and related material*. Clarendon Press Oxford,inc. 1977.
- [6] Desai, R., Lakshminarayan, D., Patel, P. and Panchal, C. Indium sesquiteroxide (In_2Te_3) thin film strain gauge. *Sensors and Actuators* 121 (2005): 405–409.
- [7] Chung, G. S. Characteristics of tantalum nitride thin film strain gauges for harsh environments. *Sensors and Actuators A* 135 (2007): 355–359.
- [8] Arshak, A., Arshak, K., Morris, D., Korostynska, O. and Jafer. Investigation of TiO_2 thick film capacitors for use as strain gauge sensors *Sensors and Actuators A* 122 (2005): 242–249.
- [9] Peiner, E., Tibrewala, A., Bandorf, R., Biehl, S. and Doering, L., Micro force sensor with piezoresistive amorphous carbon strain gauge. *Sensors and Actuators A* 130131 (2006): 75–82.

- [10] Li, J., Longtin, J. P., Tankiewicz, S., Gouldstone, A. and Sampath, S. Interdigital capacitive strain gauges fabricated by direct-write thermal spray and ultrafast laser micromachining. *Sensors and Actuators A* 133 (2007): 1–8.
- [11] Cullity, B.D. *Element of X-ray diffraction*. Addison-westley publishing Company,inc. 1959.
- [12] Feynman, P., Leighton, B. and Sands, M. *Feynman lecture on physics*. Addison-westley publishing Company,inc. 1964.
- [13] Safari, A., Panda, R. K. and F.Janas, V. *Ferroelectrics Ceramics : Processing Properties and Applications*. Rutgers university, Piscataway NJ 08855 USA,inc. 2009.
- [14] Xu, R., Shen, M., Ge, S., Gan, Z. and Cao, W. Dielectric enhancement of sol-gel derived BaTiO₃ /SrTiO₃ multilayered thin films. *Thin Solid Films* 406 (2002): 113–117.
- [15] Saravanan, K.V., Sudheendran, K., and Krishna, G. Optical and Structural microwave characteristics of sol-gel derived Barium Strontium Titanate thin films. *Materials Chemistry and Physics* 105 (2007): 426–432.
- [16] Aulika, I. et al. Structural and optical characterization of Ba_{0.8}Sr_{0.2}TiO₃ PLD deposited films. *Optical Material* 30 (2008): 1017–1022.
- [17] Panda, B., Dhar, A., Nigamb, G., Bhattacharyab, D. and Rayb, S. Optical properties of RF sputtered strontium substituted barium titanate thin films. *Thin Solid Films* 332 (1998): 46–49.
- [18] Supasai, T. et al. Influence of temperature annealing on optical properties of SrTiO₃/BaTiO₃ multilayered films on indium tin oxide. *Applied Surface Science* 256 (2010): 4462–4467.

- [19] Hodak, S. K. and Rogers, C. T. Microstructure and dielectric response of SrTiO₃/NdGaO₃ interdigitated capacitors. *Microelectronic Engineering* 85 (2008): 441–451.
- [20] Dalberth, M., Stauber, R., Price, J., Rogers, C.T. and Galt, D. Improved low frequency and microwave dielectric response in strontium titanate thin films grown by pulsed laser ablation. *Applied Physics Letters* 72 (1998): 507–509.
- [21] Guo, Y., Suzuki, K., Nishizawa, K., Miki, T. and Kato, K. Dielectric and piezoelectric properties of highly (1 0 0)-oriented BaTiO₃ thin film grown on a Pt/TiO_xSiO₂/Si substrate using LaNiO₃ as a buffer layer. *Journal of Crystal Growth* 284 (2005): 190–196.
- [22] Madeswarana, S., Varatharajanb, N. G. R., Ravi, G. and Jayavel, R. Effect of rhodium doping on the growth and characteristics of BaTiO₃ single crystals grown by step-cooling method. *Journal of Crystal Growth* 266 (2004): 481–486.
- [23] Lahiry, S. and Mansingh, A. Dielectric properties of solgel derived barium strontium titanate thin films. *Thin Solid Films* 516 (2008): 1656–1662.
- [24] Cowley, R. The Phase Transition of Strontium Titanate Philosophical Transactions: Mathematical. *Physical and Engineering Sciences* 354 (1996): 2799.
- [25] Gim, Y. et al. Microstructure and dielectric properties of Ba_{1-x}Sr_xTiO₃ films grown on LaAlO₃ substrates. *Applied Physics Lette* 77 (2000): 1200.
- [26] Yimpa, P. and Hodak, S.K. Simulation of bending beam consisting of thin film capacitors. Senior project, Department of Physics Faculty of Science Chulalongkorn university, 2009.

- [27] Hong, L., Zhaohui, P., Xiaohong, Z., Dingquan, X. and Jianguo, Z. The effect of different electrode structures on the dielectric properties of lanthanum-doped lead titanate ferroelectric thin films. *Frontiers of Materials Science in China* 1 (2007): 322–325.
- [28] Available from: <http://www.camglassblowing.co.uk/gproperties.htm>
- [29] Farnell, G. W., CERMAK, I., SILVESTER, P. and WONG, S. Capacitance and Field Distributions for Interdigital Surface-Wave Transducers. *IEEE T. Son. Ultrason* 3 (1970): 188–195.
- [30] Hodak, S. K. Effect of crystal structure on strontium titanate thin films and their dielectric properties. Doctoral dissertation, Department of Physics Faculty of Science University of Colorado at Boulder, 2000.
- [31] Thitinan, S. Automated plasma parameter measuring system using electrical probe. Master's Thesis, Department of Metrology Faculty of Science Chulalongkorn university, 2008.
- [32] Supasai, T. et al. Structural and optical studies on BaTiO₃ and BaTiO₃/SrTiO₃ multilayer films prepared by a sol-gel technique. Doctoral dissertation, Department of Physics Faculty of Science Chulalongkorn university, 2007.
- [33] Kongwut, O. et al. Effects of gamma ray irradiation on fundamental properties of perovskite thin films prepared by a sol-gel technique. Master's Thesis, Department of Physics Faculty of Science Chulalongkorn university, 2010.
- [34] Bunting, E. N., Shelton, G. and Creamer, A. S. Properties of Barium strontium titanate dielectrics. *Journal of the American Ceramic Society* 30 (1947): 114–125.

APPENDICES

Appendix A

Oscillator circuit theory

Studying the electrical response of the film is one purpose of this research. The BTO films was used to construct the strain gauge and was attached with the oscillator circuit. In our work, the oscillator circuit is designed by Assistant Prof Dr. Jose Hodak and the schematic of circuit is shown in Fig. A.1. In design oscillator circuit, we use IC 74AC14 hex schmitt inverter as a main device. From Fig. A.1, the capacitive strain gauge is put in *A* position. 5 Volt with 3 milliamps power supply are used to supply this circuit at *B* position. The output signal come out from *P1* at *C* position. The real picture of the oscillator circuit is shown in Fig. A.2.

Fig. A.1, the oscillator circuit used to evaluate the strain. Capacitor C4 is the device under test. The oscillator is comprised by UA1 Resistor R6 and capacitor C4. The resonant frequency of this circuit is given by

$$f_{resonant} = \frac{1}{R_7 C_4} \quad (\text{A.1})$$

For a capacitor in the few pico Farad range, this frequency can easily reach some tens of megahertz using a 15 KOhm resistor for R7. The higher frequency, the lower the strains that can be detected.

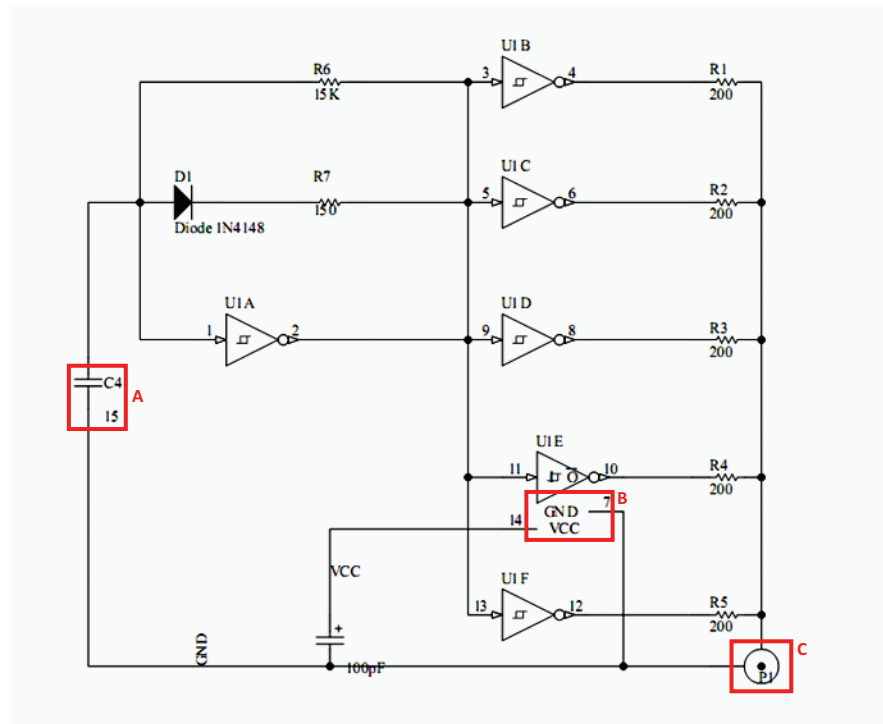


Figure A.1: The schematic of oscillator circuit

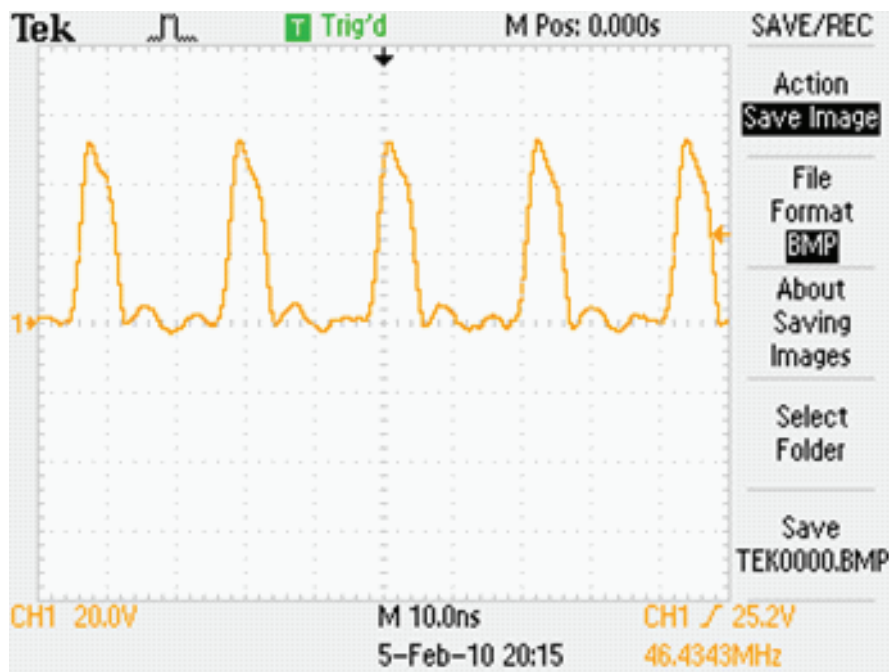


Figure A.2: Output signal from oscillator circuit

Appendix B

Simulation program

The simulation program is one of important instrument in this thesis. This simulation program was done by Mr. Pakorn Yimpa [26] using Microsoft excel with equations of deflection, stress, strain versus x position on the borosilicated cantilever of BTO strain gauge (See section 2.3). Using this program was done by varying the force value until we see that the deflection at the free end from experiment equal to the deflection distance from the simulation program. This program also showed the variation of deflection, stress, strain as a function of the x position on the clamping strain gauge.

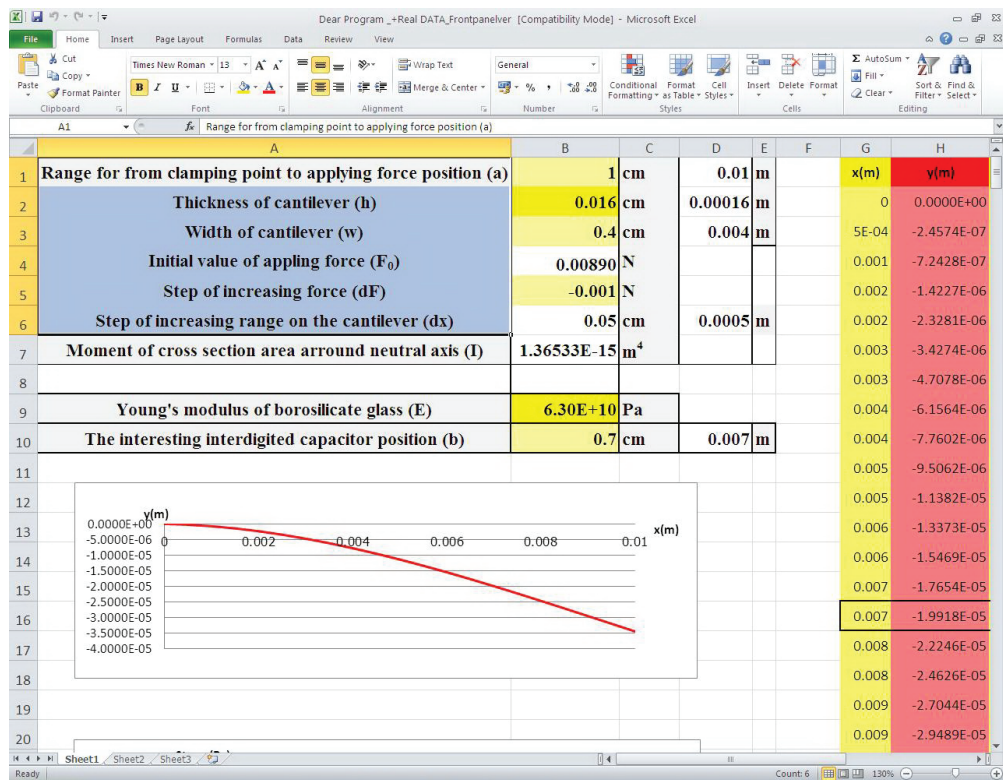


Figure B.1: Front panel of the simulation program by Mr. Pakorn Yimpa

Appendix C

XRD database

The structure of the BTO and BSTO films obtained from XRD spectra were compared with the XRD database from The International Centre for Diffraction Data(ICDD) which represented as follow

Pattern : 00-005-0626		Radiation = 1.540598		Quality : High		
BaTiO ₃		2th	i	h	k	l
Barium Titanium Oxide		22.039	12	0	0	1
		22.263	25	1	0	0
		31.498	100	1	0	1
		31.647	100	1	1	0
		38.888	46	1	1	1
		44.856	12	0	0	2
		45.378	37	2	0	0
		50.614	6	1	0	2
		50.978	8	2	0	1
		51.100	7	2	1	0
		55.955	15	1	1	2
		56.253	35	2	1	1
		65.755	12	2	0	2
		66.123	10	2	2	0
		70.359	5	2	1	2
		70.662	2	3	0	0
		74.336	5	1	0	3
		75.094	7	3	0	1
		75.164	9	3	1	0
		78.768	3	1	1	3
		79.472	5	3	1	1
		83.492	7	2	2	2
		86.965	1	2	0	3
		87.287	1	3	0	2
		88.069	1	3	2	0
		91.586	7	2	1	3
		92.060	12	3	1	2
		92.327	12	3	2	1
		99.494	1	0	0	4
		100.984	2	4	0	0
		103.869	1	1	0	4
		104.502	1	2	2	3
		104.991	1	3	2	2
		105.362	1	4	1	0
		108.256	3	1	1	4
		108.946	1	3	0	3
		109.733	5	4	1	1
		113.556	2	3	1	3
		114.362	2	3	3	1
		117.506	3	2	0	4
Lattice : Tetragonal		Mol. weight = 233.23				
S.G. : P4mm (99)		Volume [CD] = 64.41				
a = 3.99400	Z = 1	Dx = 6.012				
c = 4.03800		l/cor = 8.34				
<p>Color: Colorless Additional diffraction line(s): Plus 10 additional reflections. Sample source or locality: Sample from National Lead Company. Sample preparation: Annealed at 1480 C in MgO. Analysis: Spectroscopic analysis: <0.1% Bi, Sr; <0.01% Al, Ca, Fe, Mg, Pb, Si; <0.001% Mn, Sn. General comments: Inverts to cubic form at 120 C. Temperature of data collection: X-ray pattern at 26 C. General comments: Merck Index, 8th Ed., p. 122. Data collection flag: Ambient.</p>						
Swanson, Fuyat., Natl. Bur. Stand. (U.S.), Circ. 539, volume 3, page 45 (1954)						
CAS Number: 12047-27-7						
Radiation : CuKα1		Filter : Beta				
Lambda : 1.54050		d-sp : Not given				
SS/FOM : F30= 19(0.0490,32)						

Pattern : 00-035-0734		Radiation = 1.540598		Quality : High		
<p>SrTiO₃</p> <p>Strontium Titanium Oxide Tausonite, syn</p>		<p>2th</p> <p>22.783 32.424 39.985 46.485 52.358 57.796 67.805 72.545 77.177 81.724 86.206 95.131 104.154 113.613 118.589 123.832 135.422 150.146</p>	<p>i</p> <p>12 100 30 50 3 40 25 1 15 5 8 16 3 10 3 10 6 9</p>	<p>h</p> <p>1 1 1 2 2 2 2 3 3 2 3 4 4 3 3 4 3 4</p>	<p>k</p> <p>0 1 1 0 1 1 2 0 1 1 2 2 1 1 3 2 3 3 2</p>	<p>l</p> <p>0 0 1 0 0 1 0 0 0 1 2 1 0 1 1 0 2 2 2</p>
<p>Lattice : Cubic</p> <p>S.G. : Pm-3m (221)</p> <p>a = 3.90500</p>		<p>Mol. weight = 183.52</p> <p>Volume [CD] = 59.55</p> <p>Dx = 5.118</p>		<p>Z = 1</p> <p>l/cor = 6.22</p>		
<p>Sample source or locality: Sample from Nat. Lead Co. Analysis: Spectrographic analysis: <0.01% Al, Ba, Ca, Si; <0.001% Cu, Mg. Temperature of data collection: Pattern taken at 25 C. Additional pattern: To replace 00-005-0634 and 00-040-1500. Data collection flag: Ambient.</p>						
<p>Swanson, H., Fuyat, Natl. Bur. Stand. (U.S.), Circ. 539, volume 3, page 44 (1954)</p>						
<p>Radiation : CuKα1</p> <p>Lambda : 1.54050</p> <p>SS/FOM : F18= 47(0.0182,21)</p>		<p>Filter : Beta</p> <p>d-sp : Diffractometer</p>				

Pattern : 00-044-0093		Radiation = 1.540598		Quality : High		
Ba _{0.77} Sr _{0.23} TiO ₃		2th	i	h	k	l
Barium Strontium Titanium Oxide		22.336	18	1	0	0
		31.748	100	1	0	1
		39.165	32	1	1	1
		45.426	3	0	0	2
		45.583	43	2	0	0
		51.300	10	2	0	1
		56.608	47	2	1	1
		66.330	27	2	0	2
		70.944	6	2	1	2
		75.304	7	1	0	3
		75.536	14	3	1	0
		79.734	4	1	1	3
		79.918	6	3	1	1
		84.188	8	2	2	2
		88.491	2	3	0	2
Lattice : Tetragonal		Mol. weight = 221.79				
S.G. : P4mm (99)		Volume [CD] = 63.08				
a = 3.97710	Z = 1	Dx = 5.838				
c = 3.98830						
Sample preparation : Prepared by using stoichiometric mixture of Ba C O ₃ , Sr C O ₃ and Ti O ₂ , heat treated at 1200 C.						
Data collection flag : Ambient.						
Wang, P., Huang, Z., Werner, P., Wuji Cailiao Xuebao, volume 3, page 15 (1988)						
Radiation : CuKα1		Filter : Not specified				
Lambda : 1.54060		d-sp : Guinier				
SS/FOM : F15=116(0.0048,27)		Internal standard : Si				

Pattern : 01-089-8211		Radiation = 1.540598		Quality : Calculated		
(Ba _{0.256} Sr _{0.744})TiO ₃		2th	i	h	k	l
Barium Strontium Titanium Oxide		22.638	73	1	0	0
		32.230	999	1	1	0
		39.747	206	1	1	1
		46.225	349	2	0	0
		52.064	38	2	1	0
		57.470	317	2	1	1
		67.440	171	2	2	0
		72.145	20	3	0	0
		76.728	116	3	1	0
		81.227	46	3	1	1
		85.672	49	2	2	2
Lattice : Cubic		Mol. weight = 196.24				
S.G. : Pm-3m (221)		Volume [CD] = 60.45				
a = 3.92470		Dx = 5.390				
	Z = 1	l/cor = 8.96				
ICSD collection code : 088532						
Cancel :						
Data collection flag: Ambient.						
Joseph, J., Vimala, T.M., Raju, J., Murthy, V.R.K., J. Phys. D: Appl. Phys., volume 32, page 1049 (1999) Calculated from ICSD using POWD-12++						
Radiation : CuK α 1		Filter : Not specified				
Lambda : 1.54060		d-sp : Calculated spacings				
SS/FOM : F11=1000(0.0000,11)						

Appendix D

Conference presentation

International presentations:

2010, P. Promsena, J.H.Hodak, A. Wisitsoraat, and S. K. Hodak. Strain Sensing Properties Of Barium Strontium Titanate Thin Films Deposited On Flexible Substrates. Poster presentation at The Sixth Mathematics and Physical Sciences Graduate Congress, Faculty of Science, University of Malaya, Kuala Lumpur (December 13-15 2010) Code: PM 516

2009, P. Promsena, J.H.Hodak, A. Wisitsoraat, and S. K. Hodak. Design of low cost capacitive strain gauge. Poster presentation at Asiasense 2009 The 4th International Conference on Sensors at The Imperial Queen's Park Hotel, Bangkok, Thailand (July 29-31 2009) Code: AS-P-R018

2009, P. Promsena, J.H.Hodak, A. Wisitsoraat, and S. K. Hodak. Design of low cost capacitive strain gauge. Poster presentation at The Fifth Mathematics and Physical Sciences Graduate Congress, Faculty of Science, Chulalongkorn University, Bangkok (December 7-9 2009) Code: PM 513

Local presentations:

2010, P. Promsena, J.H.Hodak, A. Wisitsoraat, and S. K. Hodak. Capacitance Responses of Barium Titanate and Barium Strontium Titanate Thin Films Prepared by Sol-Gel Technique. Oral presentation at Siam Physics Congress 2010, Kanjanaburi (March 25-27 2010) Code: TF-O9

2010, P. Promsena, J.H.Hodak, A. Wisitsoraat, and S. K. Hodak. Capacitance Responses of Barium titanate and Barium Strontium Titanate Thin Films Prepared by Sol-Gel Technique. Poster presentation at The 16th National Graduated Research Conference, Faculty of Science, Meajo University, Chiangmai (March 11 2010) Code: P-PS 11

2009, P. Promsena, J.H.Hodak, A. Wisitsoraat, and S. K. Hodak. Design of low cost capacitive strain gauge. Poster presentation at Siam Physics Congress 2009, Methavalai Hotel, Cha-am, Phetchburi (March 19-21 2009) Code: MP-P25

2009, P. Promsena, J.H.Hodak, A. Wisitsoraat, and S. K. Hodak. Design of low cost capacitive strain gauge. Oral presentation at The Science Forum 2009, Faculty of Science, Chulalongkorn University, Bangkok (March 12-13 2009) Code: P 8

Appendix E

Publication

P. Promsena, J.H.Hodak, A. Wisitsoraat, and S. K. Hodak. Capacitance Responses of Barium titanate and Barium Strontium Titanate Thin Films Prepared by Sol-Gel Technique. (Proceeding from The 16th national graduate research conference)

การตอบสนองของค่าความจุไฟฟ้าของฟิล์มบางแบเรียมไททาเนต
และสตรอนเทียมไททาเนตเตรียมโดยเทคนิคโซลเจล

CAPACITANCE RESPONSES OF BARIUM TITANATE AND BARIUM STRONTIUM
TITANATE THIN FILMS PREPARED BY SOL-GEL TECHNIQUE

ปาริต พรหมเสนา^{1/} โยเซ่ โฮดัก^{2/} อนูรัตน์ วิสิทธิโสระอัท^{3/} และ สตรีรัตน์ โฮดัก^{4/}
Pavarit Promsena^{1/} Jose Hodak^{2/} Anurat Wisitsoraat^{3/} and Satreerat Hodak^{4/}

บทคัดย่อ

ตัวเก็บประจุราคาประหยัดทำมาจากวัสดุไดอิเล็กตริก แบเรียมไททาเนตและแบเรียมสตรอนเทียมไททาเนต ปลูกบนแก้วโบโรซิลิเกตที่มีความยืดหยุ่นโดยเทคนิคโซลเจล ความกว้างของช่องแคบตัวเก็บประจุที่มีอิเล็กโทรด เคลือบบนฟิล์มบางมีค่า 100 ไมครอน มีความยาวของช่องแคบ 27.8 มิลลิเมตร และมีขนาดโดยรวม 3x4 มิลลิเมตร ค่าคงที่ของแลตทิซของ $Ba_xSr_{(1-x)}TiO_3$ น้อยกว่า $BaTiO_3$ เนื่องจากการแทนที่ของอะตอมสตรอนเทียมในตำแหน่งของ อะตอมแบเรียม มีการวัดการตอบสนองเชิงความจุไฟฟ้าที่เป็นฟังก์ชันของความถี่และพบว่าค่าความจุไฟฟ้ามี ค่าสูงสุดประมาณ 1 พิโคฟารัดสำหรับฟิล์มบาง $Ba_{0.8}Sr_{0.2}TiO_3$
คำสำคัญ: แบเรียมสตรอนเทียมไททาเนต, การตอบสนองของค่าความจุไฟฟ้า, วิธีการโซลเจล

Abstract

Low cost capacitors were made of dielectric materials, barium titanate ($BaTiO_3$) and barium strontium titanate ($BaSrTiO_3$), depositing on flexible borosilicate glass using sol-gel technique. The gap width of the coplanar capacitor is 100 μm , with finger length of 27.8 mm., and the overall size of 3x4 mm. The lattice constant of the $Ba_xSr_{1-x}TiO_3$ films are smaller than that of pure $BaTiO_3$ due to the substitution of Sr to Ba sites. The capacitance responses as a function of frequency were measured and the maximum capacitance around 1 pF was found in $Ba_{0.8}Sr_{0.2}TiO_3$ film.

Keywords: $Ba(Sr)TiO_3$, capacitance responses, sol-gel method

Introduction

Ferroelectric materials strongly exhibit piezoelectric properties when the temperature is below Curie point depending on each type of materials (Sharma and Sharma, 1998). Early work has extensively focused on the piezoelectric properties of lead zirconate titanate ($PbZr_xTi_{1-x}$ or PZT) due to its high value of charge coefficient (Shen *et al.*, 2002). Recently, it is desirable that lead-free materials will be replaced lead materials for many applications such as high dielectric constant capacitors such as DRAM, sensors and transducers (Shen *et al.*, 2002; and Kumar and Manavalan, 2005). Barium strontium titanate ($Ba_xSr_{1-x}TiO_3$ or BSTO) which is non-lead material has been extensively studied due to Curie point near room temperature and therefore the dielectric tenability has been observed near room temperature range. It has been reported that the Curie temperature of $BaTiO_3$ is about 400K (Chen *et al.*, 2008). Furthermore,

¹นิสิตบัณฑิตศึกษา ภาควิชาฟิสิกส์ คณะวิทยาศาสตร์ จุฬาลงกรณ์มหาวิทยาลัย

²ภาควิชาฟิสิกส์ คณะวิทยาศาสตร์ มหาวิทยาลัยมหิดล

³หน่วยปฏิบัติการวิจัยนาโนอิเล็กทรอนิกส์และเครื่องกลจุลภาค ศูนย์เทคโนโลยีอิเล็กทรอนิกส์และคอมพิวเตอร์แห่งชาติ

⁴ภาควิชาฟิสิกส์ คณะวิทยาศาสตร์, ศูนย์นวัตกรรมนาโนเทคโนโลยี จุฬาลงกรณ์มหาวิทยาลัย

Curie temperature can be tuned by varying Ba and Sr ratios in the stoichiometric $Ba_xSr_{1-x}TiO_3$ films (Lahiry and Mansingh, 2008). Lahiry *et al.* have found that the Curie temperature of BSTO film decreases with increasing strontium contents in the film (Lahiry and Mansingh, 2008). The aim of this work is to synthesis barium titanate and barium strontium titanate and to compare the capacitance responses of both types of materials. The characteristic film properties such as the lattice constant and composition were also determined.

1. Experimental Details

1.1 Sample preparation

Barium titanate or barium strontium titanate films were prepared from starting materials consisting of barium acetate [$Ba(CH_3COO)_2$], strontium acetate [$Sr(CH_3COO)_2$], titanium (IV) isopropoxide [$Ti(CH_3CH_2CHO)_4$]. In the first step, barium acetate was dissolved in acetic acid [CH_3COOH] by magnetic stirring on the hot plate. $Ti(CH_3CH_2CHO)_4$ was mixed in methanol then barium acetate solution was quickly added in $Ti(CH_3CH_2CHO)_4$ solution. Appropriate amount of strontium acetate was added in the first step to provide BSTO precursor. The desired solution was deposited on borosilicate glass using spin coating method and then each layer of the films was annealed at $650^\circ C$ in the air atmosphere for one hour. After completing six layers, the films were annealed at $650^\circ C$ for 2 hours to ensure the crystallinity of the films. The diagram of film preparation was shown in Fig. 1.

The stoichiometry of $Ba_xSr_{1-x}TiO_3$ was determined from the energy-dispersive spectroscopy and the XRD database. We constructed Au/Cr electrode on top of BTO and BSTO films by sputtering chromium (Cr) and gold (Au) targets through the shadow mask using DC sputtering technique. The gap width of the coplanar capacitor is $100\ \mu m$, with finger length of 27.8 mm., and the overall size of 3x4 mm. The electrode pattern is shown in Fig. 2(a) and the photograph of an individual capacitor is shown in Fig. 2(b).

1.2 Experimental Setup

Film crystallinity was analyzed by X-ray diffraction technique. The capacitance and the dielectric loss ($\tan\delta$) as a function of frequency in the range of 100-1100 kHz for each capacitor were measured with HP4192 LF impedance analyzer.

2. Results and discussion

The X-rays diffraction (XRD) patterns of the BTO and BSTO films on borosilicated glass substrates annealed at $650^\circ C$ were shown in Fig. 3. At this temperature, the films were formed polycrystalline. The lattice constant was calculated from (101) and (200) peak positions showing that the lattice constant of the $Ba_xSr_{1-x}TiO_3$ films are smaller than that of pure $BaTiO_3$ as can be seen from the shift to higher diffraction angles. The values of lattice constants (a and b) BTO and BSTO films are 4.05 and

4.00 \AA . Because the atomic radius of strontium atom is smaller than that of barium atom, by the substitution of Sr to Ba sites causes the reduction in the lattice constant. The compositions of the film was obtained using wavelength dispersive X-ray spectrometer (WDX) equipped with electron probe microscope. We probed electron beams on three different spots of the BSTO films and the atomic percentage of each element was averaged as shown in Table 1. The stoichiometric $\text{Ba}_{0.8}\text{Sr}_{0.2}\text{TiO}_3$ film was determined.

The resulting capacitance and dielectric loss as a function of frequency of the BTO and BSTO films are shown in Fig. 4. Fig. 4(a) and 4(b) shows that the capacitance and loss tangent of the BTO film with frequency in the range 100-1100 kHz. Fig. 4(c) and 4(d) shows that the capacitance and loss tangent of the BSTO film measured in the same range of frequency. We found that by adding strontium contents to the BTO film can increase the capacitance e.g. the dielectric constant. Normally, the associated dielectric loss increase with the dielectric constant in which we observed in our films as well. The maximum capacitance around 1.1 pF was found in $\text{Ba}_{0.8}\text{Sr}_{0.2}\text{TiO}_3$ film as compared with 1.0 pF for BTO film. We noted that these two films have the same thicknesses. Similar results have been observed by others (Xu *et al.*, 2002; and Vitanov *et al.*, 2003).

3. Conclusions

The films were formed polycrystalline at 650 °C on borosilicate substrates. By substitution strontium (Sr) atom to the site of barium (Ba) atom, the lattice constant was reduced due to replacing Ba with Sr having smaller atomic radius. The dielectric constant and corresponding dielectric loss increased due to the strain effect in the film.

Acknowledgement

The authors would like to thank the Department of Physics, Faculty of Science, Chulalongkorn University, the Asahi Foundation, the graduate thesis grant, the Thailand Toray Foundation, the Thailand Research Fund (TRF) and NECTEC for financial and equipment support.

References

- Sharma, H.B. and Sharma, H.H.K., 1998. Electrical properties of sol-gel processed barium titanate films. *Thin Solid Films* 330: 178-182.
- Xu, R., Shen, M., Ge, S. and Gan, Z., 2002. Dielectric enhancement of sol-gel derived $\text{BaTiO}_3/\text{SrTiO}_3$ multilayered thin films. *Thin Solid Films* 406: 113-117 (2002).
- Kumar, A. and Manavalan, S.G., 2005. Characterization of barium strontium titanate thin films for tunable microwave and DRAM applications. *Surface and Coating Technology* 406-413.
- Chen, W.P., Shen, Z.J., Guo, S.S., Zhu, K., Qi, J.Q., Wang, Y. and Chan, H.L.W., 2008. A strong correlation of crystal structure and Curie point of barium titanate ceramics with Ba/Ti ratio of precursor composition. *Physica B* 403: 660-663.

Lahiry, S. and Mansingh, A., 2008. Dielectric properties of sol-gel derived barium strontium titanate thin films. *Thin Solid Films* 516: 1656-1662.

Vitanov, P., Harizanova, A., Ivanova, T., Velkov, D. and Raytcheva, Zd., 2003. Deposition, structure evolution and dielectric properties of BaTiO_3 and $\text{Ba}_x\text{Ti}_{1-x}\text{O}_3$ thin films prepared by the sol-gel method. *Vacuum* 69: 371-377.

Element	Mass %	Norm %	Atom %	Error %
Sr	3.159	13.719	16.816	7.45
Ba	17.557	75.544	59.101	0.98
Ti	2.490	10.736	24.083	3.41
Total	23.206	100.000	100.000	

Table 1. The composition of $\text{Ba}_{0.8}\text{Sr}_{0.2}\text{TiO}_3$ film

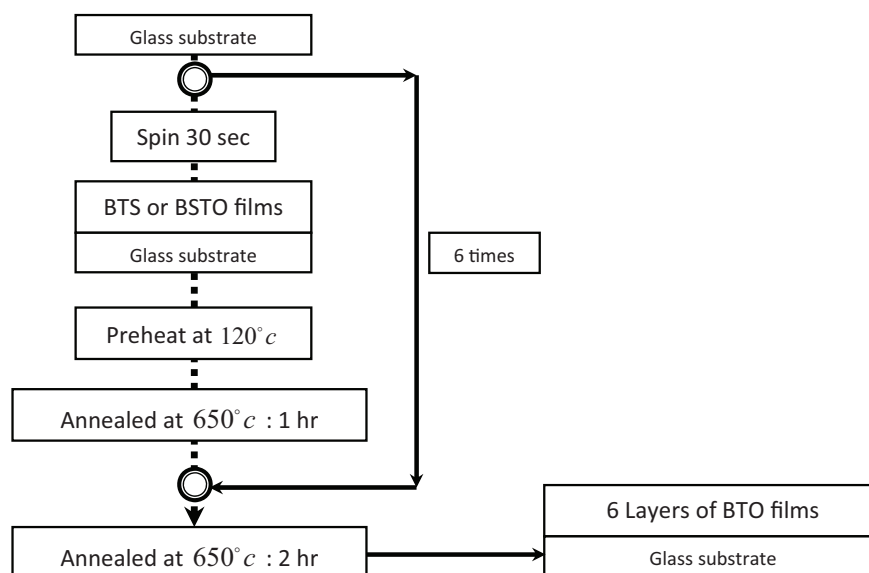


Fig. 1. The process of film preparation

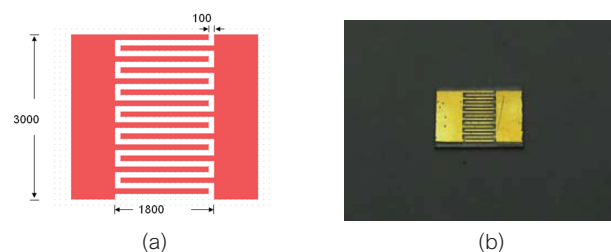


Fig. 2. (a) The size of coplanar capacitor (b) The photograph of an individual capacitor

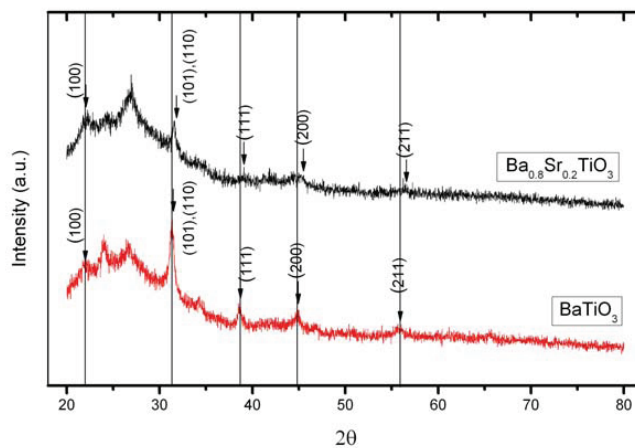


Fig. 3. X-ray diffraction pattern of BaTiO_3 and $\text{Ba}_{0.8}\text{Sr}_{0.2}\text{TiO}_3$

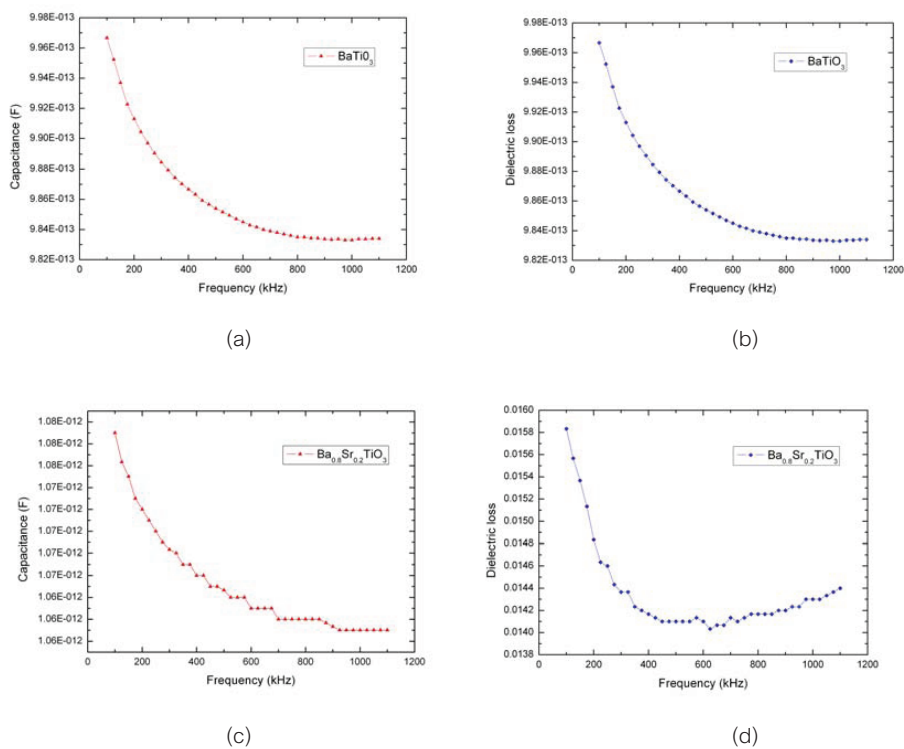


Fig. 4. Electrical properties of BaTiO_3 and $\text{Ba}_{0.8}\text{Sr}_{0.2}\text{TiO}_3$ film (a) Capacitance of BTO, (b) Dielectric loss of BTO, (c) Capacitance of BSTO and (d) Dielectric loss of BSTO

Appendix F

Research award



Figure F.1: Best poster presenter award from 6th Mathematics and Physical Science Congress 2010 at University of Malaya Kuala Lumpur Malaysia

Vitae

Mr Pavarit Promsena was born on the 9th November 1983 in Phrae, Thailand. He finished high school from Phiriyalai school, Phrae, then received his Bachelor of Science degree in Physics major from Chulalongkorn University, Bangkok in 2007, and continued his master's study at Chulalongkorn University.